Locomotion and Drift in Viscous Flows: Numerical and Asymptotic Predictions

Submitted in partial fulfillment of the requirements for the degree of

Doctor of Philosophy

in

Chemical Engineering

Nicholas G. Chisholm

B.S., Chemical Engineering, University of Rochester

Carnegie Mellon University
Pittsburgh, PA

May 2017

Acknowledgments

I have found my time at Carnegie Mellon University to be greatly enriching both professionally and personally. The Department of Chemical Engineering has provided an ideal setting for developing myself into a highly capable researcher, which is due in no small part to the unparalleled quality of the faculty, staff, and students here. I am particularly grateful for having the opportunity to work with my adviser and thesis committee chair, Dr. Aditya Khair, who has been nothing short of an excellent instructor, mentor, and coach. I am truly thankful for the help and guidance he has provided for the past five years and for his unparalleled dedication to his Ph.D. students. I would also like to thank all remaining members of my thesis committee, Dr. Shelley Anna, Dr. Erik Ydstie, Dr. Fred Higgs, and Dr. Kaushik Dayal for their insight and interest in my work. Last but not least, I would like to thank my wife, Lisa Kasiewicz, who I was so very fortunate to have met during my time at Carnegie Mellon. Lisa's love and support during the ups and downs of my Ph.D. career are something I find very difficult to imagine having gone without.

Funding: This work was partially supported by the John and Claire Bertucci Fellowship in engineering, and I gratefully acknowledge this financial support.

Abstract

We theoretically investigate the fluid mechanics of self-propelled (or swimming) bodies. An important factor concerning the hydrodynamics of locomotion concerns the relative strength of inertial to viscous forces experienced by the swimmer, the ratio of which is quantified by the Reynolds number, Re. Particular attention is given to the regime where Re is intermediate, where viscous and inertial forces are both relevant to fluid motion. We study two broad classes of swimmers: 'pushers' and 'pullers'. Pushers produce thrust from the rear of their body, while pullers generate thrust from the front. We first investigate the near-field flow due to pushers and pullers by numerically solving the Navier-Stokes equations for Re of 0.01–1000. We show that, although the locomotion of pushers and pullers is similar at small Re, drastic differences due to fluid inertia arise as Re is increased. Most remarkably, flow instabilities develop at much smaller Re for a puller than a pusher.

Further, we investigate the large scale fluid transport induced by a swimmer as a function of Re in the context of the induced 'drift volume'. The drift volume quantifies the volume of fluid swept out by a 'dyed' fluid plane that is initially perpendicular to the body's path. However, we first address the previously unsolved problem of the drift volume due to a body that is towed by an external force at finite Re. While the drift volume is comparable to the body volume in inviscid flow ($Re \to \infty$), it is much larger when Re is finite due to viscous effects. The drift volume due to a swimmer is smaller than that due to a towed body because swimmers generate a weaker far-field flow. However, it is still potentially large compared to the volume of the swimmer's body in the viscously dominated small-Re regime. However, the drift volume of a swimmer quickly diminishes as Re is increased.

Table of Contents

List of Tables

List of Figures and Illustrations

Chapter 1

Introduction

In this thesis, we theoretically investigate the locomotion of swimmers across a range of Reynolds numbers and the fluid transport that they induce. The hydrodynamics of swimming organisms has long captured the interest of biologists, physicists, and engineers alike. A striking observation is that these organisms span seven orders of magnitude from the smallest motile bacteria to the largest marine mammals [1]. If a Newtonian fluid is assumed, the underlying physics of the flow are primarily dictated by the Reynolds number,

$$Re = \frac{\varrho U_c l_c}{\mu}, \tag{1.1}$$

where l_c is the characteristic length of the swimmer, U_c is the characteristic speed, ϱ is the fluid density, and μ is the viscosity. Thus, Re quantifies the ratio of inertial to viscous forces in the fluid.

Microscopic swimmers have $Re \ll 1$, and their locomotion is dominated by viscous forces. On the other hand, macroscopic organisms swim at $Re \gg 1$, and the forces governing the fluid motion are largely inertial. The physics of locomotion in these inertial and viscous regimes are entirely different. In fact, microscopic swimmers must utilize completely different mechanisms of locomotion than their macroscopic counterparts in order to swim effectively [2].

Owing to the linear nature of the Stokes equations, which govern small-Re flow, analysis of swimming microorganisms in this regime has been quite extensive, and excellent reviews of small-Re self-propulsion are given by Brennen and Winnet [3], Lauga and Powers [4], and Pak and Lauga [5]. Similarly, the analysis of large-Re macroscopic swimmers such as fish and marine mammals is simplified by the use of potential flow theory, and investigation of locomotion in this regime has also been considerable [6, 7, 8, 9].

The analysis of locomotion when Re is intermediate has not been nearly as broad and is considerably less well understood [3, 10]. This is due in no small part to the fact that the physics of self-propulsion at intermediate Re are inherently more complex than at small or large Re. Viscous and inertial forces are comparable in strength, and the resulting equations of flow are nonlinear, making analysis more difficult. This represents a substantial knowledge gap considering that the biomass of zooplankton communities in the oceans is often dominated by millimeter-sized intermediate-Re swimmers such as copepods [11] and krill [12]. One approach taken by previous investigators is to focus on a particular organism or mechanism of swimming [e.g., 13, 14, 15]. However, there is some risk of masking the basic features common to all swimmers by considering only specific cases. Thus, we take the alternative approach of considering reduced-order models that capture the essential fluid mechanics of self-propulsion in the simplest manner possible.

In chapter 2, the self-propulsion of a spherical squirmer — a model swimming organism that achieves locomotion via steady tangential movement of its surface — is quantified across the transition from viscously to inertially dominated flow. Specifically, the flow around a squirmer is computed for Reynolds numbers (Re) between 0.01 and 1000 by numerical solution of the Navier-Stokes equations. A squirmer with a fixed swimming stroke and fixed swimming direction is considered. We find that fluid inertia leads to profound

differences in the locomotion of pusher (propelled from the rear) versus puller (propelled from the front) squirmers. Specifically, pushers have a swimming speed that increases monotonically with Re, and efficient convection of vorticity past their surface leads to steady, axisymmetric flow that remains stable up to at least $Re = 1000$. In contrast, pullers have a swimming speed that is non-monotonic with Re. Moreover, they trap vorticity within within their wake, which leads to flow instabilities that cause a decrease in the time-averaged swimming speed at large Re. The power expenditure and swimming efficiency are also computed. We show that pushers are more efficient at large Re, mainly because the flow around them can remain stable to Re much greater than that of a puller. Interestingly, if unstable axisymmetric flows at large Re are considered, pullers are more efficient due to the development of a Hill's vortex-like wake structure.

In chapters 3 and 4, we shift our attention from the dynamics of a model swimmer to quantifying fluid transport by both towed and self-propelled bodies as a function of Re. By 'towed', we mean that the body moves under the influence of an external force (e.g., gravity) rather than under its own power. Motivation for investigating this problem is provided by the recent suggestion that small- and intermediate-Re swimmers may be relevant to large scale biomixing of the oceans, which has been a topic of considerable debate [e.g., 16, 17, 18, 19, 20, 21]. In particular, we adopt the concept of the *drift volume*, introduced by Darwin [22], in order to build a simple framework for quantifying the net fluid motion induced a translating body. The drift volume D refers to the volume of fluid enclosed between the initial and final profiles of an initially flat marked sheet of fluid that deforms due to the passage of the body. Although the drift volume has been used to quantify fluid transport in inviscid flows ($Re \to \infty$) [23, 24, 25, 26] and Stokes flows ($Re \to 0$) [27, 19, 28], the nature of the drift volume at finite Re has not been previously

quantified.

Indeed, this is the topic of chapter 3, where we first address the case of a towed body. Classic investigations of the drift volume in an inviscid fluid show that D is comparable in magnitude to the volume of the translating body [22]. The situation is fundamentally different for a viscous fluid. For instance, if the Reynolds number Re is zero, then D diverges with the distance traveled by the body and may be orders of magnitude larger than the body volume [27]. In chapter 3, we interpret the drift volume as the flux through a stationary plane bounded by a stream tube, thus allowing D to be computed without explicit reference to the trajectories of the marked fluid elements, which greatly simplifies our analysis. We focus our analysis on a rigid sphere of radius a that is steadily towed through a viscous fluid by an external force. The initial profile of the marked fluid is taken to be a disc of finite height h, which is assumed to be much larger than a. A two-term asymptotic expansion of D for $a/h \to 0$ is computed for $Re = 0$ and compared to the analogous result for inviscid flow in order to illustrate the fundamental differences between these two cases. Next, a leading order approximation to D for a sphere translating at small Re is computed using Oseen's approximation to the flow. These results are extended to $Re \geq O(1)$ by taking advantage of the fact that, at distances greatly exceeding its radius, the flow around a sphere is described by the point force solution to Oseen's equations [29]. Therefore, it is found universally for finite Re that D diverges as the distance traveled by the sphere becomes large. However, the exact nature of this divergence depends upon the ratio of the distance traveled by the sphere to the radius of the initially marked disc of fluid (h).

Having developed a methodology for computing the drift volume of towed bodies as a function of Re, we apply a similar analysis to swimming bodies at both zero and finite Re in chapter 4. In particular, we discuss the ability of a

steadily translating low Reynolds number (Re) swimmer to displace a volume of fluid that is large compared to the volume of the swimmer itself, which is necessary for the swimmer to induce large scale mixing. The swimmer is modeled simply as a force dipole aligned with the swimming direction. It is found the drift volume induced by a swimmer is large if $Re \ll 1$. In fact, it diverges as the extent of the marked fluid is made large for a swimmer at $Re = 0$. However, we show that D does not diverge if Re is finite. Inertia screens the far-field flow, and hence the volume transported by the swimmer decreases as $1/Re$. For swimmers at $Re \geq O(1)$, we demonstrate the D quickly reduces to an amount that is of the same order of magnitude as the volume of fluid physically displaced by the body. Hence, D depends largely upon the nature of the near field-flow that is not associated with large-scale fluid motion in this case. That an intermediate-Re swimmer does not induce large-scale fluid transport via its drift volume suggests that the amount of fluid mixing achievable by such a swimmer individually is limited.

Chapters 2 to 4 are intended to be self-contained and may be read as such. More detailed introductions to their respective subject matters are given within. In chapter 5, we conclude by summarizing the key results and findings of the work presented in this thesis, and we consider possible directions for future research.

Chapter 2

Inertial locomotion of a squirmer

2.1 Introduction

Swimming organisms span seven orders of magnitude in length [1]: a motile bacterium may be only a few microns across whereas a large marine animal may be several meters in length. Completely different fluid flow regimes are observed at either end of this scale [7]. The underlying flow physics are dictated by the relative strength of inertial to viscous forces within the fluid. The Reynolds number, $Re = \varrho V L/\mu$, represents the ratio of these forces, where ϱ is the fluid density, μ is the viscosity, V is a characteristic speed, and L is a characteristic length.

Locomotion at macroscopic length scales is associated with large Re flows dominated by inertial forces. Roughly all swimmers between the size of a small fish ($Re \sim 10^3$) and a blue whale ($Re \sim 10^8$) fall into this *Eulerian* realm. Self-propulsion is primarily generated by reactionary forces arising from the acceleration of fluid opposite the swimming direction [7]. This is accomplished, for instance, by the motion of a fish's tail fin. The effects of viscosity are

The content in this chapter is from an article published in the Journal of Fluid Mechanics that is co-authored by Dominique Legendre and Eric Lauga [30]. Explicit permission from the co-authors has been obtained to include the content in this thesis.

confined to thin boundary layers so long as the swimmer is streamlined in shape [31]. Thus, fluid-mechanical analysis may be carried out using inviscid flow theory [32].

In contrast, microscopic organisms fall into the *Stokesian* realm, where viscous forces dominate and Re is small, ranging from 10^{-4} for bacteria to 10^{-2} for mammalian spermatozoa [3]. Here, inertial mechanisms of thrust generation are unavailable; the swimming mechanics of these organisms are governed by resistive forces, where viscous thrust is balanced by viscous drag [4].

Lighthill [33] and Blake [34] introduced the *spherical squirmer* as simple model for self-propulsion at small Re, intended to mimic the locomotion of organisms possessing dense arrays of motile cilia. A squirmer of radius a achieves locomotion through small, axisymmetric deformations of its surface, such that the radial and tangential velocity components on its surface in a co-moving frame are

$$v_r|_{r=a} = \sum_{n=0}^{\infty} A_n(t) P_n(\cos\theta), \quad \text{and} \quad v_\theta|_{r=a} = \sum_{n=1}^{\infty} \frac{-2}{n(n+1)} B_n(t) P_n^1(\cos\theta), \tag{2.1}$$

respectively. Here, r is the distance from the origin, located at the center of the squirmer's body, θ is the polar coordinate measured from the direction of locomotion, A_n and B_n are time dependent amplitudes (with units of velocity), and P_n (P_n^1) are (associated) Legendre polynomials of order n. The direction of locomotion remains constant (at small Re) due to the axisymmetry of the swimming "stroke" represented by (2.1), and thus the swimming velocity is $\boldsymbol{U} = U\boldsymbol{e}_z$, where $\boldsymbol{e_z}$ is the unit vector along the swimming direction. From the requirement that the net hydrodynamic force must vanish on a steadily translating, neutrally buoyant body, the swimming speed of a squirmer in Stokes flow is $U = (2B_1 - A_1)/3$ [33]. This depends only upon the first mode

of each surface velocity component in (2.1) and is independent of viscosity, since thrust and drag scale linearly with viscosity at $Re = 0$.

A reduced-order squirmer may be conceived by assuming that the surface deforms steadily and only in the tangential direction ($A_n = 0$, and $B_n =$ constant). Furthermore, one may retain only the first two B_n coefficients, so that

$$v_\theta|_{r=a} = v_s(\theta) = B_1 \sin\theta + B_2 \sin\theta\cos\theta. \tag{2.2}$$

(2.2) is a slip flow along the squirmer surface that vanishes at the poles ($\theta = 0$ and $\theta = \pi$). The first term in (2.2) is solely responsible for propulsion, $U|_{Re=0} = 2B_1/3$, and generates an irrotational velocity field decaying as $1/r^3$, characteristic of a potential dipole. The second term is associated with the stresslet exerted by the squirmer, $\boldsymbol{S}|_{Re=0} = 4\pi\mu a^2 B_2(3\boldsymbol{e_z}\boldsymbol{e_z} - \boldsymbol{I})/3$, where $\boldsymbol{I}$ is the identity tensor [35, 36]. The flow field due to this term decays as $1/r^2$ in Stokes flow. There is no Stokeslet contribution to the velocity field because the squirmer is force-free: there is no net hydrodynamic force; drag balances thrust. Defining $\beta = B_2/B_1$ and with $B_1 > 0$, squirmers are divided into *pullers* having $\beta > 0$ and *pushers* having $\beta < 0$ [37] (figure 2.1). If $|\beta| > 1$, there exists an intermediate point within $0 < \theta < \pi$ at which $v_s(\theta)$ vanishes, leading to recirculating flow behind (in front of) a puller (pusher) [38]. The magnitude of β determines the amount of vorticity generation. If $\beta = 0$, the squirmer is "neutral" and generates a potential flow, which, in fact, is a solution to the Navier-Stokes equations (NSE) at any Re. In this sense, β quantifies the amount of fluid mixing by a squirmer. Importantly, the swimming speed is independent of β at $Re = 0$; there is no coupling between vorticity generation and propulsion in Stokes flow.

Clearly, this reduced-order squirmer is a simplistic model for the locomotion of actual organisms. Nevertheless, it has been employed to examine

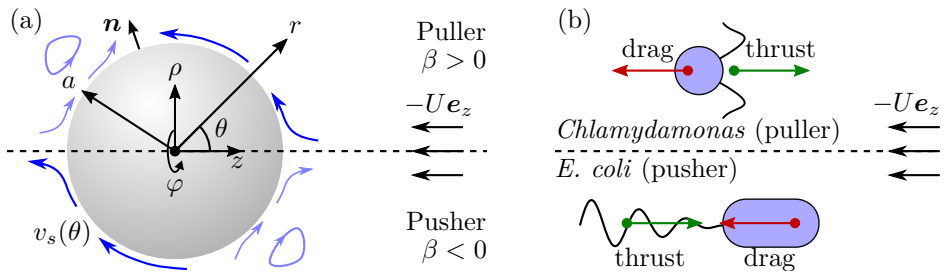

Figure 2.1: (a) Illustration of the flow pattern around a pusher and puller squirmer in a co-moving frame. (b) Typical examples of pusher and puller squirmers. Arrows represent the force exerted by the fluid on the swimmer body. Pullers generate thrust from the front, e.g., the breast-stroke-like motion performed by *Chlamydamonas* (a green algae). Pushers generate thrust from the rear, e.g., *E. coli* which propel themselves by rearward facing flagella.

various facets of self-propulsion in Stokes flow, including swimming in non-Newtonian fluids [39, 40], mixing by swimmers [41, 20, 28], feeding and nutrient transport [38, 42, 43], and hydrodynamic interactions of swimmers [36, 44, 45]. A detailed summary is provided by Pak and Lauga [5].

Recently, the locomotion of a squirmer with stroke (2.2) was studied at non-zero Re. In particular, matched asymptotic expansions were used to compute U to $O(Re)$ by Wang and Ardekani [46] and to $O(Re^2)$ by Khair and Chisholm [47]. It was found that U depends on β at non-zero Re: pushers ($\beta < 0$) swim faster than pullers ($\beta > 0$). Here, the Reynolds number is $Re \equiv 2\varrho B_1 a/(3\mu)$. This is a result of vorticity generation, or mixing, being coupled to propulsion at finite Re. Note that the vorticity distribution around a Stokesian squirmer evolves purely via diffusion and is thus fore-aft anti-symmetric. This anti-symmetry precludes the generation of a net force and hence propulsion. The anti-symmetry is broken at finite Re as vorticity is advected past the squirmer into a far-field inertial wake. Khair and Chisholm [47] demonstrate that the wake structure around a squirmer is consistent with previous work on steady, self-propelled bodies at non-zero Re [29, 18], underscoring the squirmer as a suitable reduced-order model for inertial locomotion.

Additionally, Li and Ardekani [48] and Khair and Chisholm [47] report numerical results for the swimming speed of a squirmer for $Re \leq 1$, which show that the asymptotic results are of practical value in the rather limited range of $Re \lesssim 0.2$.

The goal of the present chapter is to quantify the locomotion of a spherical squirmer in the transition from viscously to inertially dominated flow. Self-propulsion in this regime has not been fully explored, especially in comparison to the Stokesian and Eulerian limits. Here, viscous and inertial forces may be simultaneously responsible for thrust and drag on a swimmer making analysis more difficult. Specifically, we focus on intermediate values of Re that lie between 0.1 and 1000, thus bridging the gap between viscous and inertial swimming. A multitude of aquatic organisms, such as zooplankton that are on the millimeter to centimeter length scale, fall into this range and utilize a wide variety of swimming motions. The majority of past work has focused on the swimming of particular species of organisms [13, 10, 14, 49, 15]. Such work undoubtedly provides valuable information on the specific locomotive strategies of these organisms. However, in contrast to past work, our objective is to quantify finite Re locomotion from a broad perspective using the simple (reduced-order) squirmer model. Specifically, through the numerical solution of the NSE, we will determine the flow fields around pusher and puller squirmers for $0.01 < Re < 1000$ and $-5 \leq \beta \leq 5$, along with their swimming speeds, power expenditure, and hydrodynamic efficiency. Furthermore, we will determine the stability of the steady axisymmetric flow about a squirmer and compute the critical values of Re at which transitions to three-dimensional (3D) and transient flow occur. A prime outcome of our work is to demonstrate that the fluid mechanics of pusher and puller squirmers are dramatically distinct at intermediate Re, in contrast to their similar locomotions at small Re.

It must be noted that the squirmer model is indeed simple in that it only considers propulsion via generation of a surface velocity, and it may not well capture the detailed flows arising from the complex geometries and locomotions of many biological swimmers. Nonetheless, its simple geometry allows examination of the essential fluid mechanics of a self-propelling body. Moreover, our results are easily compared to the classic problems of flow past a no-slip sphere and flow past an inviscid spherical bubble, which are well studied at all Re. Nonetheless, there also exist certain biological swimmers that provide reasonably close realizations of a finite Re squirmer. *Paramecium*, a ciliate 0.2 mm in size, can reach speeds of 10 mm/s while evading threats, corresponding to $Re \approx 2$ [50]. Ctenophores, the largest organisms known to use ciliary propulsion, are a few millimeters to a few centimeters in size and swim about one body-length per second when foraging (and faster when evading threats). Thus, the Reynolds number of the flow ranges from roughly 100 to 6000 [51]. Moreover, some species of Ctenophores, such as *Pleurobrachia bachei* have bodies that exhibit strong axial symmetry and are approximately spherical in shape [52]. Such examples provide additional biological motivation for studying the squirmer model outside the small Re limit.

The remainder of this chapter is organized as follows. In section 2.2, we present the governing equations for a self-propelled squirmer. In section 2.3 we detail two numerical methods used for performing steady, axisymmetric and transient, three-dimensional (3D) simulation of flows about a squirmer, respectively. The subsequent results are presented and discussed in section 2.4. Finally, we conclude and suggest directions for future work in section 2.5.

2.2 Governing equations

Consider a single squirmer with a steady swimming stroke (2.2) in an unbounded incompressible Newtonian fluid (figure 2.1a). We normalize length by the squirmer radius a, velocity by the speed of a neutral squirmer in potential flow ($2B_1/3$), time by $3a/(2B_1)$, and pressure and viscous stresses by $2B_1\mu/(3a)$. Thus, the Reynolds number is defined as $Re \equiv 2\varrho B_1 a/(3\mu)$. Henceforth, all quantities are dimensionless unless indicated otherwise. The fluid motion is governed by the NSE,

$$\nabla \cdot \boldsymbol{v} = 0, \quad \text{and} \quad Re\,\frac{D\boldsymbol{v}}{Dt} = \nabla^2 \boldsymbol{v} - \nabla p, \tag{2.3}$$

where $\boldsymbol{v}$ is the velocity vector, p is the pressure, t is time, and D/Dt represents the material derivative.

We assume that the squirmer body has a constant mass density ϱ_b, equal to ϱ, and is thus neutrally buoyant. If the flow about the squirmer is axisymmetric, the net hydrodynamic force perpendicular to the squirmer's axis (taken as the z-axis of an attached Cartesian frame) and the net hydrodynamic torque vanish. Thus, the squirmer does not rotate and maintains a straight-line path. The remaining z-component of the hydrodynamic force F_z is equal to the mass times acceleration of the squirmer body in the z-direction,

$$Sk\,\frac{dU}{dt} = F_z = \int_S (\boldsymbol{n} \cdot \boldsymbol{\sigma} \cdot \boldsymbol{e_z})\,\mathrm{d}S, \tag{2.4}$$

where U is the swimming speed, S represents the spherical squirmer surface with outer unit normal $\boldsymbol{n}$, and $\boldsymbol{\sigma} = -p\boldsymbol{I} + \nabla\boldsymbol{v} + (\nabla\boldsymbol{v})^\top$ is the stress tensor. The Stokes number, $Sk = Re\,\varrho_b/\varrho$, is equal to Re because $\varrho = \varrho_b$. This force will vanish when the flow is at steady state and the squirmer translates with a steady velocity. Therefore, a steady squirmer in steady, axisymmetric flow is force-free and torque-free.

However, the spherical squirmer is a bluff object; the steady, axisymmetric flow around it may become unstable beyond a critical value of Re, yielding to 3D and/or unsteady flow. This leads to the production of instantaneous lift forces perpendicular to the squirmer's axis and instantaneous hydrodynamic torques that result in lateral motion and rotation of the squirmer's body, respectively. Here, for simplicity, forces and torques are externally applied to the squirmer to keep its direction and orientation constant and along the z-axis during our computations, although the speed is allowed to vary according to (2.4). Thus, the squirmer is not fully free-swimming but rather constrained to follow a straight-line path. This is a logical first step before considering the more complicated paths of motion that would arise if the squirmer trajectory were to be unconstrained. For instance, the transitions in flow that occur for a freely rising or sinking body, and the values of Re at which they occur, are closely related to the those that take place in the flow past an analogous fixed body [53, 54]. Thus, we expect that our study of a squirmer constrained to a single direction of swimming will be relevant to a fully free-swimming squirmer. Indeed, the two problems are identical in the regime of axisymmetric flow and only differ when such flow destabilizes. Although it is not considered here, note that the path of motion of a fully free squirmer could be computed via a force balance (in all directions) and an angular momentum balance on the squirmer body, similar to the computation of the paths of freely rising or falling bodies [54].

2.3 Numerical methods

Two numerical schemes were employed to compute the flow field around a squirmer for $-5 \leq \beta \leq 5$ and $0.01 \leq Re \leq 1000$. One assumes steady, axisymmetric flow where the steady-state swimming speed U is that at which

F_z in (2.4) vanishes. The other considers fully 3D, transient flow, in which case $U = U(t)$ is given by integrating (2.4) via a time stepping procedure.

2.3.1 Computation of steady, axisymmetric flow

We convert the NSE into a stream function–vorticity form. From (2.3), the steady vorticity transport equation is

$$Re[(\boldsymbol{v}\cdot\nabla)\boldsymbol{\omega} - (\boldsymbol{\omega}\cdot\nabla)\boldsymbol{v}] = \nabla^2\boldsymbol{\omega}, \tag{2.5}$$

where $\boldsymbol{\omega} = \nabla\times\boldsymbol{v}$ is the vorticity vector. A stream function ψ is defined in cylindrical coordinates, such that

$$v_\rho = -\frac{1}{\rho}\frac{\partial\psi}{\partial z}, \quad \text{and} \quad v_z = \frac{1}{\rho}\frac{\partial\psi}{\partial\rho}, \tag{2.6}$$

where ρ is the distance from the z-axis, and v_ρ and v_z represent the fluid velocity components.

Combining (2.6) with (2.5) gives

$$Re\left(\left|\frac{\partial(\psi,\omega)}{\partial(r,z)}\right| + \frac{\omega}{r^2}\frac{\partial\psi}{\partial z}\right) = \nabla^2\omega - \frac{\omega}{r^2}, \tag{2.7}$$

where ω is the component of $\boldsymbol{\omega}$ in the azimuthal direction φ about the z-axis; the other (ρ and z) components of $\boldsymbol{\omega}$ vanish by symmetry. Expressing ω in terms of ψ gives

$$\omega\rho = -E^2\psi, \quad \text{where} \quad E^2 \equiv \rho\frac{\partial}{\partial\rho}\left(\frac{1}{\rho}\frac{\partial}{\partial\rho}\right) + \frac{\partial^2}{\partial z^2}. \tag{2.8}$$

Equations (2.7) and (2.8) are coupled partial differential equations, with the former being nonlinear. These may be simultaneously solved for the scalar quantities ψ and ω to give the flow field given appropriate boundary conditions.

In a co-moving frame, the squirmer surface ($r = 1$) is a streamline with tangential velocity given by (2.2). Thus, $\psi|_{r=1} = 0$, and $[\nabla\psi\cdot\boldsymbol{n}]_{r=1} = v_s = 3\sin\theta(1+\beta\cos\theta)/2$. The values of β and Re are specified constants, so the

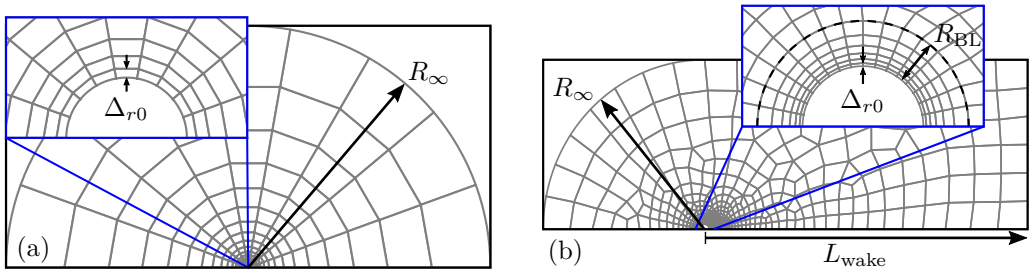

Figure 2.2: Structured polar grids (a) were used for both axisymmetric and 3D (by revolving them azimuthally) computations of the flow. For axisymmetric computations with $Re > 10$, a different mesh (b) was used with greater resolution in the wake of the squirmer to more accurately resolve the details of the flow in this region.

swimming stroke is represented as a fixed boundary condition. By axisymmetry, $\psi|_{\rho=0} = 0$, and $\omega|_{\rho=0} = 0$ on the z-axis. Finally, the flow is uniform in the far-field, so $\psi|_{r\to\infty} = -U\rho^2/2$, and $\omega|_{r\to\infty} = 0$.

A spectral element method [55] was used to spatially discretize (2.7), (2.8), and the boundary conditions. The shape functions were defined as a tensor product of Nth order Lagrange polynomials supported at the $N+1$ Gauss-Lobatto integration points over the square $[-1,1]^2$ parametric space of each quadrilateral element. Integration over each element was carried out using the corresponding Gauss-Lobatto quadrature rule to produce a system of non-linear algebraic equations. This system was solved iteratively using Newton-Raphson iteration. Iteration was terminated when the L2-norm of the relative errors in ψ and ω over all discretization points was reduced below 10^{-6}.

The spatial domain was discretized into high-order computational grids using the software package "Gmsh" [56]. Three different grids were used depending on the value of Re. For $Re \leq 0.1$, a polar grid extending to $R_\infty = 1000$ and consisting of 9-by-9 node quadrilateral elements was used. The elements were distributed evenly in the θ-direction ($N_\theta = 10$) and progressed geometrically outward in the r-direction ($N_r = 20$). A similar grid was used for

$0.1 \leq Re \leq 10$, with $R_\infty = 100$ (figure 2.2a). For $Re > 10$, a different mesh was used to provide better resolution in the squirmer wake. Here, a boundary layer grid was used along the squirmer surface, with $N_r = 10$ and $N_\theta = 51$, extending $R_{\mathrm{BL}} = 0.25$ radii from the squirmer surface. The radial grid size grows geometrically with r, and is initially $\Delta_{r0} = 0.01$ at the squirmer surface. The remainder of the grid was unstructured, with upstream boundaries extending to $R_\infty = 32$, and a rectangular wake region extending a distance of 100 radii behind the squirmer (figure 2.2b). The far-field boundary conditions were enforced at the exterior boundary of the mesh. We refer the reader to appendix A for details on grid convergence.

The far-field boundary condition of uniform, oncoming flow cannot be directly applied because the steady-state swimming speed U is unknown *a priori*. Since the flow is assumed to be steady and axisymmetric, we instead enforce that F_z is equal to zero. Expressing (2.4) in terms of ω for an axisymmetric flow field gives [47]

$$F_z = Re\,\frac{\pi}{2}\int_0^\pi v_s^2 \sin(2\theta)\,\mathrm{d}\theta + \pi\int_0^\pi \left(\frac{\partial(r\omega)}{\partial r} - 2\omega\right)\sin^2\theta\,\mathrm{d}\theta. \tag{2.9}$$

A secant method was used to iteratively compute the value of U at which (2.9) vanishes. At each iteration, the flow is solved with $U = U^{\langle n\rangle}$, where n is the iteration number, and (2.9) is evaluated to give $F_z^{\langle n\rangle}$. An improved estimate for U is given by linear interpolation: $U^{\langle n+1\rangle} = (U^{\langle n\rangle}F_z^{\langle n-1\rangle} - U^{\langle n-1\rangle}F_z^{\langle n\rangle})/(F_z^{\langle n-1\rangle} - F_z^{\langle n\rangle})$. Iteration was terminated when $|U^{\langle n\rangle} - U^{\langle n-1\rangle}|$ was reduced below 10^{-5}.

Computations for each value of β were started initially with $Re = 0.01$. Two initial guesses of the swimming speed are required, which were made as $U^{\langle 0\rangle} = 0.99$ and $U^{\langle 1\rangle} = 1.01$, since U is close to unity at small Re. An initial guess for the stream function and vorticity fields of uniformly zero was sufficient for convergence of the computed flow in this case. A simple continuation strategy was employed by incrementally increasing Re. Initial guesses for U

and the flow field at a given Re were supplied by using the values computed at the last largest values of Re for which a converged solution was successfully reached.

2.3.2 Computation of unsteady, three-dimensional flows

Unsteady, 3D flows were explored using the JADIM code described in detail in Legendre and Magnaudet [57] and Magnaudet, Rivero, and Fabre [58]. The JADIM code has been extensively used and validated in previous studies concerning the 3D flow dynamics of spheroidal and disk-shaped bodies with no-slip (solid) or slip (bubble) surfaces in uniform, shear or turbulent flows [see, e.g., 57, 59, 60, 61]. In particular, the wake transition from axisymmetric to 3D flow for a fixed body has been considered in Mougin and Magnaudet [62] and Magnaudet and Mougin [63]; and Fabre, Auguste, and Magnaudet [64]. In the case of a sphere, a first bifurcation resulting in loss of axial symmetry in the flow is detected at a critical Reynolds number (based on the sphere radius and speed of translation U) of $Re_U^{(c1)} = 105$, in agreement with linear stability analysis [65] and previous numerical studies [66, 67]. A second (Hopf) bifurcation is observed at $Re_U^{(c2)} = 135$, leading to time-dependent flow, which is also in good agreement with previous numerical findings [66, 67], according to which the Hopf bifurcation lies in within the range $135 < Re_U^{(c2)} < 137$. In Magnaudet and Mougin [63], the vortex shedding process for a sphere at $Re_U = 150$ corresponds to a Strouhal number of $Sr_U = fa/U = 0.0665$, where f is the dimensional frequency of vortex shedding. This falls within 2 to 3% of that reported by Johnson and Patel [66] and Tomboulides and Orszag [67] for the same Re.

Briefly, the JADIM code solves the incompressible NSE (2.3) in terms

of velocity and pressure variables. The spatial discretization employs a staggered grid on which the equations are integrated using a second-order accurate finite-volume method. Fluid incompressibility is satisfied after each time step by solving a Poisson equation for an auxiliary potential. Time advancement is achieved through a second-order accurate Runge-Kutta/Crank-Nicholson algorithm. At each time step, the swimming speed U is updated by integrating (2.4). For each simulation, the squirmer was started from rest with swimming stroke (2.2) and allowed to accelerate. Simulations were terminated after a steady time-averaged value of the swimming speed was reached.

A polar grid extending to $R_\infty = 150$ and rotated around the z-axis was used for computation (figure 2.2a). Nodes were distributed uniformly in the θ-direction and in a geometric progression in the r-direction. The effect of the number of nodes ($N_r = 150$ along the radial direction, $N_\theta = 250$ along the polar direction, and $N_\varphi = 64$ along the azimuthal direction), as well as R_∞ and the radial grid size $\Delta_{r0} = 0.001$ at the body surface, were checked in order to ensure grid independence of the results (see appendix A).

The transition from steady, axisymmetric to unsteady, 3D flow was investigated by running the simulation for a given period of time while allowing numerical error to perturb the initially axisymmetric flow profile. If the flow is unstable for a given β and Re, such perturbations are expected to grow over time, resulting in a flow field that is potentially 3D and/or unsteady. Such is the case for a no-slip sphere in uniform flow, where distinct axisymmetric; steady, 3D; and unsteady, 3D flow regimes are respectively encountered as Re is increased [65, 67]. Specifically, simulations were performed with Re increased in coarse increments until a transition, if one occurred, was identified. Then, Re was increased in finer increments within the interval in which the transition occurred. This process was repeated until a satisfactory estimate of the critical transition Reynolds number was procured. The simulation time

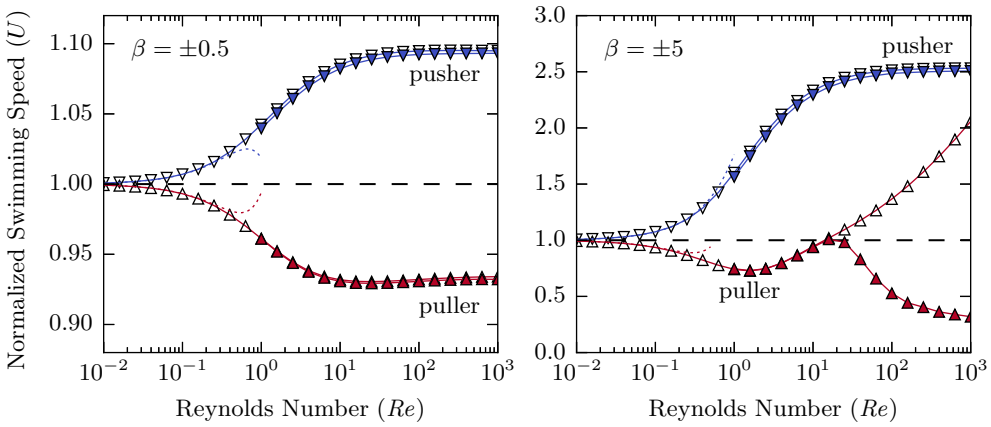

Figure 2.3: Swimming speed, normalized by $2B_1/3$, for $\beta = \pm 0.5$ and ± 5. The "$\bigtriangledown$" markers represent pushers and the "$\bigtriangleup$" markers represent pullers. Hollow markers represent steady, axisymmetric solutions, and filled markers represent unsteady, 3D solutions. We follow these conventions for the remainder of the chapter. The dashed line represents the speed of a neutral ($\beta = 0$) squirmer. For a $\beta = +5$ puller, the steady, axisymmetric flow destabilizes at $Re \approx 20$, and hence the steady, axisymmetric and unsteady, 3D solutions diverge. Time averages of U are taken in the case of unsteady flow. Dotted lines show the asymptotic result of Khair and Chisholm [47] for U to $O(Re^2)$.

was increased as the critical Reynolds number of transition was approached, as it generally required longer times for perturbations to grow and hence for the flow to reach a final transitioned state.

2.4 Results and discussion

2.4.1 Swimming speed of a squirmer

The calculated swimming speed U versus Re of a squirmer with $\beta = \pm 0.5$ and ± 5 is shown in figure 2.3. There, U is normalized by $2B_1/3$, which is the swimming speed at $Re = 0$ for all β, or the swimming speed of a neutral squirmer at arbitrary Re. At $Re = 0$, U is independent of β because the equations governing the flow are linear. Thus, the two terms in the swimming stroke (2.2) contribute to the flow field independently; only the first (treading) term generates propulsion, while the second only produces vorticity. This is

not the case as Re is increased from zero: pushers (pullers) monotonically increase (decrease) in speed if $Re \lesssim O(1)$, in agreement with results from asymptotic analyses [46, 47]. The increase or decrease in swimming speed is amplified as $|\beta|$ increases. However, as Re is increased beyond an $O(1)$ value, significantly different behavior of pushers versus pullers is observed. For all pushers and pullers with $\beta < 1$, U continues to vary monotonically with increasing Re, eventually reaching a terminal value. The computed swimming speed is nearly identical for axisymmetric and 3D computations, suggesting that there is no departure from steady, axisymmetric flow. In contrast, a non-monotonic trend is observed for pullers with $\beta > 1$, and no limiting value for U is apparent through $Re = 1000$. Moreover, the axisymmetric and 3D computations give drastically different results, suggesting the destabilization of the axisymmetric, steady flow (see section 2.4.3 for more detail). We remind the reader that Re for a squirmer is defined as $2\varrho B_1 a/(3\mu)$, in contrast to the Reynolds number based on the translational speed U, which we denote $Re_U = \varrho U a/\mu$. Note that Re and Re_U are the same order of magnitude since $U \sim O(1)$.

Distinct contributions to the thrust and drag on a squirmer are provided by the two terms on the right-hand-side of (2.9). The first term, which equals $8\pi\, Re\, \beta/15$ after integration, depends solely on the swimming stroke and vanishes when $Re = 0$. The second term also vanishes if $Re = 0$ due to the antisymmetric, purely diffusive, distribution of the vorticity, and it is hence associated with forces arising from the flow asymmetry produced by inertia at finite Re. Thus, (2.9) is satisfied identically in Stokes flow, and a squirmer propels itself at the same speed regardless of β. However, pushers increase in speed with Re while pullers decrease at finite $Re \lesssim O(1)$. In the former case, the first term represents a drag force because it is negative when $\beta < 0$. Thus, the redistribution of vorticity caused by inertia is responsible for the

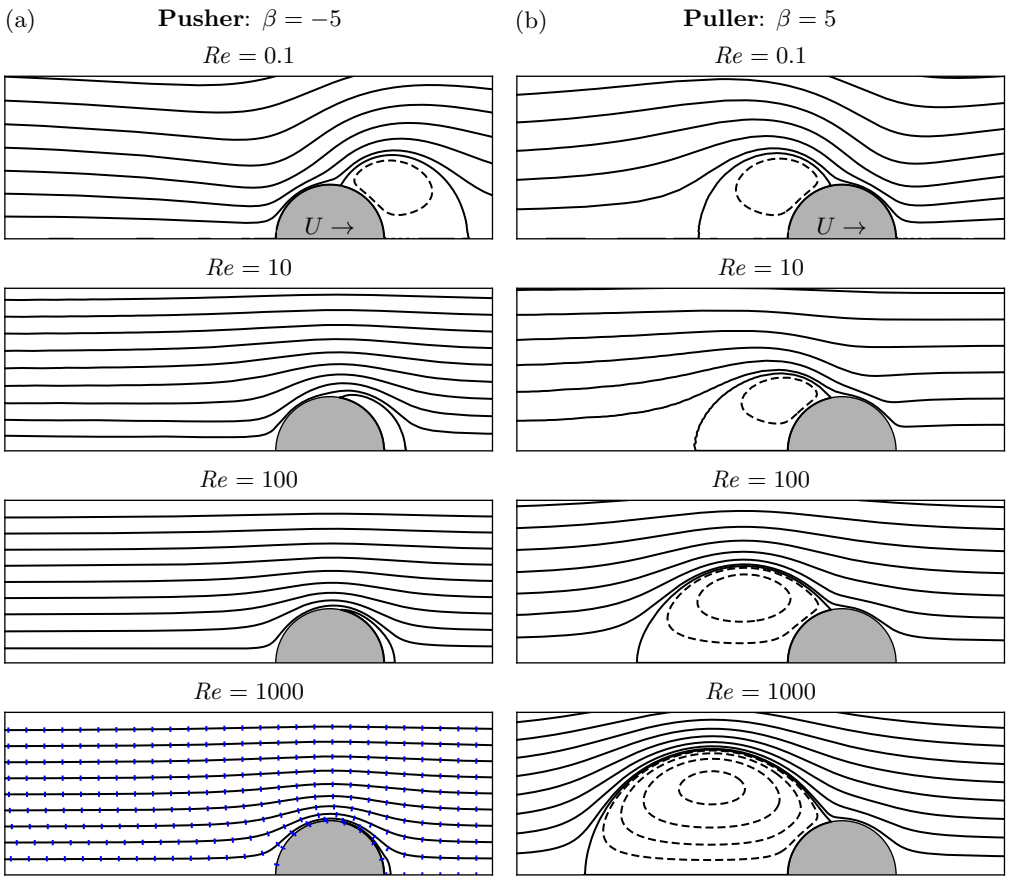

Figure 2.4: Streamlines of axisymmetric flow past a squirmer with $\beta = \pm 5$. Dashed streamlines represent negative values of the stream function. The tick marks in (a) at $Re = 1000$ follow along streamlines of irrotational flow past a sphere.

extra thrust that increases the swimming speed with Re. The opposite occurs for a puller, where $\beta > 0$: the contribution of the first term is a thrust, but it is outweighed by drag produced by the inertial redistribution of vorticity. As Re is increased beyond an $O(1)$ value, the monotonic trend continues for a pusher until a limiting speed is reached. In contrast, the swimming speed of a puller becomes non-monotonic. A fuller explanation of these trends, especially when Re is large, requires a closer examination of the flow fields generated by squirmers and how they differ for pushers versus pullers.

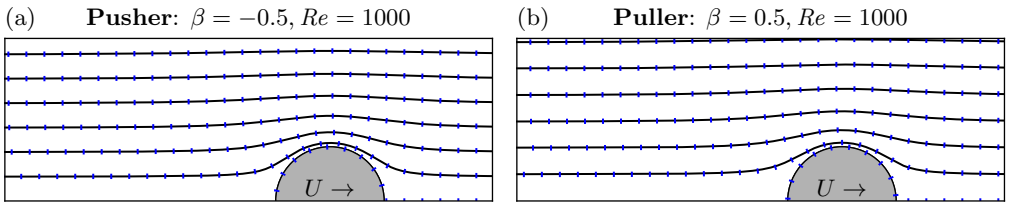

Figure 2.5: Similar to figure 2.4 except with $\beta = \pm 0.5$.

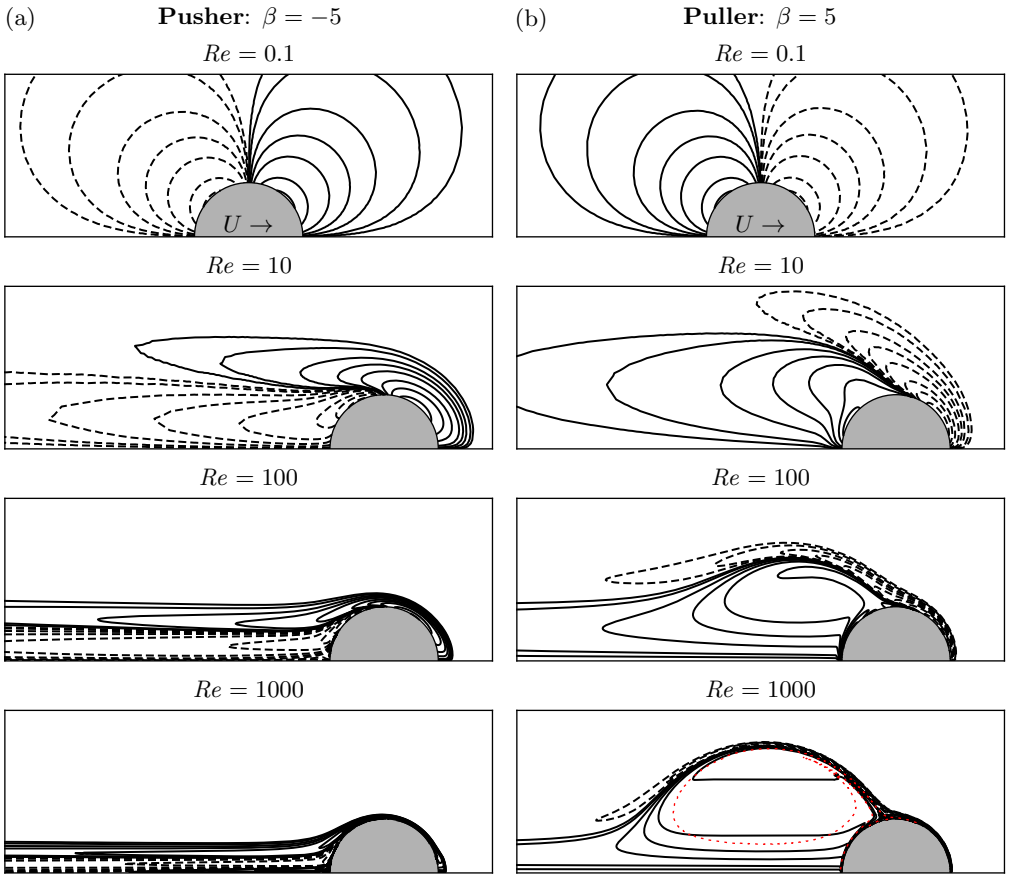

Figure 2.6: Vorticity contours for axisymmetric flow with $\omega = \pm \{0.1, 0.2, 0.5, 1, 2, 5, \ldots, 200\}$. Dashed lines represent negative values. The dotted line in (b) at $Re = 1000$ encircles the region where there is an approximately constant value of $\omega/\rho = 2.9 \pm 0.05$, indicating that the wake bubble behind a $\beta = 5$ puller has a structure resembling a Hill's vortex.

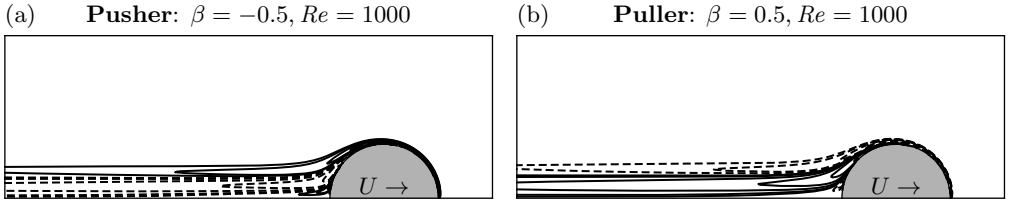

Figure 2.7: Similar to figure 2.6 except with $\beta = \pm 0.5$.

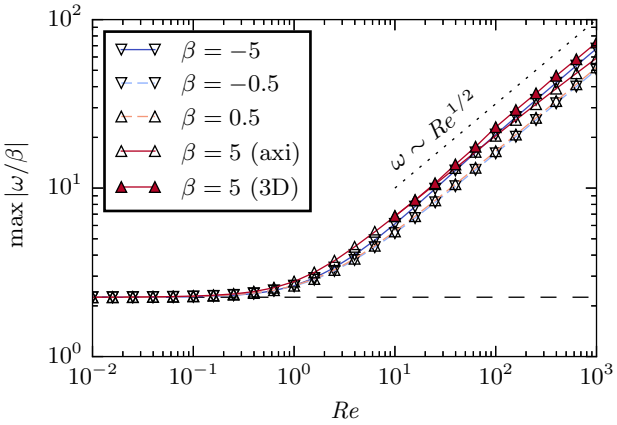

Figure 2.8: The maximum value of $|\omega|$, normalized by $|\beta|$, from axisymmetric computations at $\beta = \pm 0.5$ and ± 5 and from 3D computations for $\beta = +5$. In Stokes flow, $\max|\omega/\beta| = 9|\beta|/4$, as indicated by the dashed line to which the data collapses as $Re \to 0$. The dotted line indicates a slope of one-half, revealing that $\omega \sim \sqrt{Re}$ at large Re.

2.4.2 Flows generated by pushers and pullers

Streamlines illustrating the steady, axisymmetric flow around a pusher and puller are shown in figures 2.4 and 2.5, and contours of constant vorticity are shown in figures 2.6 and 2.7. At $Re = 0.1$, symmetries in the near-field flow are apparent due to the dominance of viscous forces over inertial forces: reversing the sign of β causes the streamlines to be mirrored along the ρ-axis. Also, the vorticity is fore-aft anti-symmetric. Pushers generate positive vorticity ahead of their direction of travel and negative vorticity behind, while pullers do the opposite. Closed-streamline recirculatory regions appear in front of pushers and behind pullers if $|\beta| > 1$. Streamlines separate from the squirmer surface at the point where the stroke $v_s(\theta)$ changes sign [38].

The flow patterns and swimming speed observed as Re is increased depend critically on β. For pushers at $Re \gg 1$, the majority of the vorticity, along with the upstream closed-streamline region that is present if $\beta < -1$, is concentrated into a laminar boundary layer of thickness $O(1/\sqrt{Re})$. This vorticity is then transported into a narrow downstream wake due to the mo-

tion of the swimming stroke (figures 2.6a and 2.7a). The streamlines outside the boundary layer and wake tend toward a potential flow profile, and no standing wake eddy is present (figures 2.4a and 2.5a). Thus, the flow around a pusher apparently resembles that past an inviscid spherical bubble at large Re_U, which exhibits the same characteristics [68, 69]. The key similarity is that the mobile surfaces of a bubble and a pusher squirmer cause advection of vorticity downstream, thus preventing it from accumulating into a recirculating wake. However, for a bubble, the shear-free surface produces $\omega \sim O(1)$, whereas for a squirmer, $\omega \sim O(\sqrt{Re})$ in the boundary layer (figure 2.8) due to the fixed nature of the surface velocity profile (swimming stroke). This is akin to a towed, rigid sphere with a no-slip surface, where the greater amount of boundary layer vorticity results in flow separation and the appearance of a wake eddy if $Re_U \gtrsim 10$, which grows with Re_U [70, 71]. These phenomena are avoided by a streamlined no-slip body, but for a pusher, the strong vorticity advection due to the propulsive surface motion interestingly achieves a similar effect. Despite the bluff body shape and $O(\sqrt{Re})$ surface vorticity of a pusher, no wake eddy is produced.

The flow around pullers with $0 < \beta < 1$ may be described likewise. As Re is increased, the boundary layer and wake become smaller in extent, and the majority of the flow domain becomes irrotational (figures 2.5b and 2.7b). Again, vorticity is efficiently swept downstream by the mobile surface with a (monotonic) swimming stroke $v_s(\theta)$ that is directed along the path of the flow. Consequently, pushers and pullers with $\beta < 1$ reach a terminal (dimensionless) swimming speed (i.e., a dimensional swimming speed that is proportional to B_1).

The axisymmetric flow that is observed around pullers with $\beta > 1$ as Re increases is very different. A trailing vortical wake bubble is indeed present and grows with Re (figure 2.4b). Thus, for pullers with $\beta > 1$, the flow

does *not* become irrotational within the majority of the flow domain as Re becomes large. As a result, the swimming speed of a $\beta > 1$ squirmer does not attain a terminal value. The wake eddy is caused by the reversal of v_s along the rear half of the squirmer surface, which hinders the advection of vorticity downstream, and causes its accumulation behind the squirmer. This resembles flow past a rigid bluff body towed by an external force, where fluid deceleration along the no-slip surface has the same effect. Indeed, if the flow is restricted to be axisymmetric, the wake bubble resembles a Hill's spherical vortex at $Re = 1000$, where ω/ρ is constant in the region of closed streamlines and $\omega = 0$ elsewhere (figure 2.6b). Batchelor [72] proposed that such flow structures exist in the wake of bluff bodies in steady, axisymmetric flow at large Reynolds numbers. The computations of Fornberg [71] show the presence of a Hill's vortex-like wake structure behind a sphere held fixed in a uniform flow, within which ω/ρ is nearly constant once Re_U is sufficiently large. Moreover, it is shown that such large Reynolds number axisymmetric flows result in very low drag forces relative to that observed in 3D flows beyond the onset of flow instabilities. The observation that U increases with Re for an axisymmetric $\beta = 5$ pusher when $Re \gtrsim O(1)$ (figure 2.3) indicates that the trailing vortex behind a $\beta > 1$ puller is analogous to that behind a towed sphere; the wake eddy acts to decrease the overall drag. Note that the point of flow separation along the surface of a squirmer always occurs where $v_s(\theta)$ changes sign regardless of Re (figure 2.4), whereas it depends on Re_U for a no-slip sphere.

2.4.3 Transition to 3D and unsteady flow

Figure 2.9 and table 2.1 detail the transition of the flow around a squirmer from steady and axisymmetric to unsteady and 3D and are derived from unsteady,

3D flow simulations. The critical values of Re at which the axisymmetry breaks ($Re^{(c1)}$) and at which the flow becomes unsteady ($Re^{(c2)}$) are shown. For $\beta > 1$ pullers, $Re^{(c1)} < Re^{(c2)}$, and a monotonic decrease of $Re^{(c1)}$ and $Re^{(c2)}$ with β is observed. Moreover, $Re^{(c1)}$ and $Re^{(c2)}$ both increase rapidly as β is decreased toward unity such that $\beta = 1$ appears to be an asymptote; pushers and pullers with $\beta < 1$ produce steady, axisymmetric flows that remain stable up to at least $Re = 1000$.

This highlights another apparent similarity between the flow past a $\beta < 1$ squirmer and an inviscid spherical bubble. For the latter, the asymptotic analysis of Moore [68] suggested that a potential flow is recovered as $Re_U \to \infty$. Specific studies have also been carried out to determine how the wake structure and flow stability vary with aspect ratio for oblate spheroidal bubbles [73, 74, 63]. It was revealed that only bubbles with an aspect ratio larger than 1.65 and 2.21 exhibit a standing wake eddy and an unstable wake, respectively. The reason is that a sufficient amount of vorticity (produced at the bubble surface in an amount proportional to the surface curvature) must accumulate in its wake for these transitions to occur. For a squirmer, a comparatively large $O(\sqrt{Re})$ amount of boundary layer vorticity is generated, whereas it is $O(1)$ for a spherical bubble, so the stability of the flow past pushers and $\beta < 1$ pullers despite this fact is an intriguing result. Again, vorticity is strongly advected downstream by the propulsive surface velocity, preventing its accumulation in the wake, and the stability of the steady, axisymmetric flow is preserved.

However, this does not imply stability at all Re. For no-slip objects where the vorticity is similarly $O(\sqrt{Re})$, turbulent boundary layers develop when Re is very large, even for streamlined objects such as airfoils or flat plates where there is no instability caused by a wake eddy. For example, the boundary layer of a no-slip sphere becomes turbulent at $Re_U \approx 10^5$ [75, p. 512]. For this reason, it is very possible that the laminar boundary layer of a squirmer will

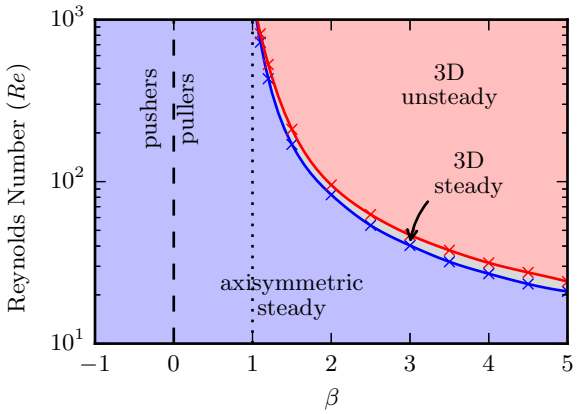

Figure 2.9: Flow state as a function of β and Re. The points of transition, marked with an "×" and interpolated by the solid lines, were obtained numerically (see also table 2.1).

β	1.1	1.2	1.5	2.0	3.0	5.0
$Re^{(c1)}$	725	432	170	83.0	40.3	21.0
$Re^{(c2)}$	818	528	210	95.3	47.8	24.2
$Re^{(c2)} - Re^{(c1)}$	93	96	40	12.3	7.5	3.2

Table 2.1: Numerically obtained critical values of Re where the flow becomes 3D ($Re^{(c1)}$) and unsteady ($Re^{(c2)}$) (see also figure 2.9).

also become turbulent at sufficiently large Re, except, perhaps, in the singular $\beta = 0$ case where potential flow results identically. Such a phenomenon likely occurs well above the maximum $Re = 1000$ considered in this work, and hence is not further discussed here.

Given the previously noted similarities of the steady, axisymmetric flows around a $\beta > 1$ puller to that past a no-slip sphere, one might also expect that the transitions to 3D and unsteady flows that occur will also be analogous. This indeed appears to be the case. For a no-slip sphere, the flow first bifurcates at $Re_U^{(c1)} \approx 105$ [65, 67], resulting in a steady, 3D flow that exhibits planar symmetry and two counter-rotating vorticies in the wake. The symmetry plane passes through the axis of translation, but its orientation is arbitrary due to the initial axisymmetry of the flow. The scenario is the same for $\beta > 1$ pullers, and planar flow symmetry is apparent in figure 2.10a. The only differ-

ence is that $Re^{(c1)}$ depends on β in the latter case. A second transition from steady to unsteady flow takes place at $Re_U\,Crit2 \approx 140$ in the case of a no-slip sphere [65, 67], and the same happens for a $\beta > 1$ puller at $Re^{(c2)} = Re^{(c2)}(\beta)$. In both cases, the planar flow symmetry persists, and as Re (or Re_U) is further increased, shedding of the wake vorticies begins to occur (figure 2.10b). Table 2.1 reveals that the quantity $Re^{(c2)} - Re^{(c1)}$ decreases significantly as β is increased; the difference is about 40 at $\beta = 1.5$ and decreases to only 3.2 at $\beta = 5$. The flow is more quickly destabilized when the value of β is larger, and hence there is only a narrow range of Re where it exhibits a steady, 3D state.

Once the flow enters a unsteady and/or 3D state, the squirmer will no longer be force-free or torque-free in general. Examining the hydrodynamic forces and torques which arise in the vicinity of $Re^{(c1)}$ and $Re^{(c2)}$ yields some interesting observations. Figure 2.11 shows the lift, defined as the force perpendicular to the direction of translation, for a $\beta = 5$ puller started from rest, in which case $Re^{(c1)} = 21.0$ and $Re^{(c2)} = 24.2$. If $Re^{(c1)} < Re < Re^{(c2)}$, as in parts (a) and (b), a constant lift force is generated once the flow reaches a steady-state. Some small oscillations that eventually die out are observed at $Re = 24.0$ but not at $Re = 21.7$. If $Re > Re^{(c2)}$, the flow is unsteady, and hence the lift does not reach a constant value in parts (c) and (d) of figure 2.11. At $Re = 25.3$, the lift is oscillatory but always acts along the same direction, while at $Re = 26.7$, the lift periodically reverses direction. The torque generated on the squirmer, plotted in figure 2.12, clearly follows the same pattern as the lift, although it is offset by 90°. The lift and torque are perpendicular due to the planar flow symmetry; the lift is in the symmetry plane, while the torque is normal to it (the symmetry can be seen visually in figure 2.10a figure 2.10b).

Hydrodynamic forces acting parallel to the direction of swimming also

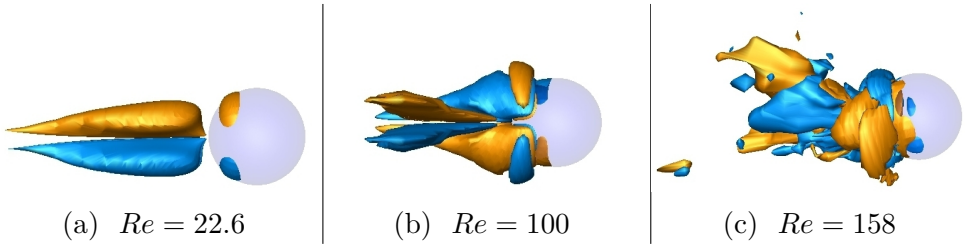

(a) $Re = 22.6$ (b) $Re = 100$ (c) $Re = 158$

Figure 2.10: The streamwise component of the vorticity for a $\beta = 5$ puller at an isocontour of $\omega_z = \pm 1.05$. In (a), the flow is planar symmetric and steady ($Re^{(c1)} < Re < Re^{(c2)}$). Two counter rotating vorticies are present in the wake. In (b), the flow is also planar symmetric but unsteady ($Re > Re^{(c2)}$), and the wake structure is more complicated; a pair of vorticies is being shed downstream from the wake. Finally in (c), the planar symmetry is broken and the flow appears to be almost chaotic in nature.

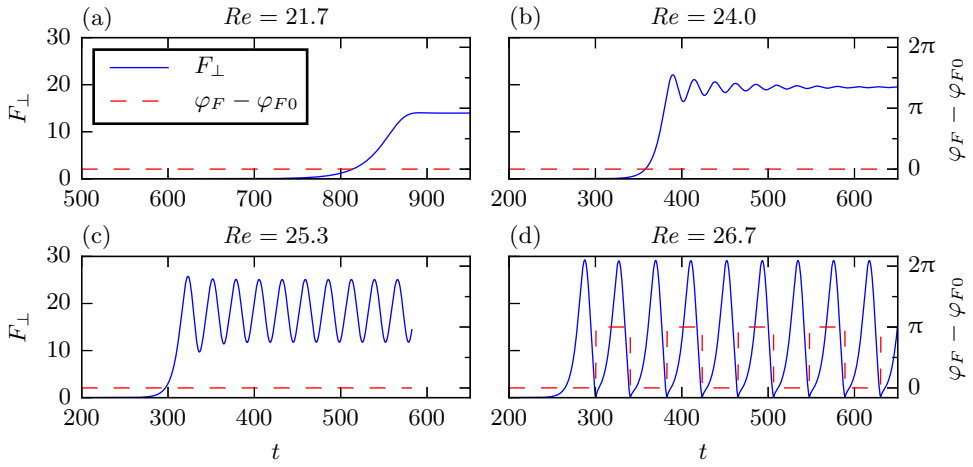

Figure 2.11: Magnitude of the lift force $F_\perp$ normalized by $2B_1 a\mu/3$ (solid) and the azimuthal angle $\varphi_F - \varphi_{F0}$ at which it acts (dashed) for a $\beta = 5$ squirmer accelerating from rest at time $t = 0$. Time is normalized by $3a/(2B_1)$. Here, φ_{F0} represents the (arbitrary) initial angle of the lift when it first becomes nonzero. In (a) and (b), $Re^{(c1)} < Re < Re^{(c2)}$, and a constant steady-state lift force is observed. In (c) and (d), $Re > Re^{(c2)}$, and the lift force is oscillatory. In (c), the direction of the lift remains constant, while in (d) it periodically reverses direction.

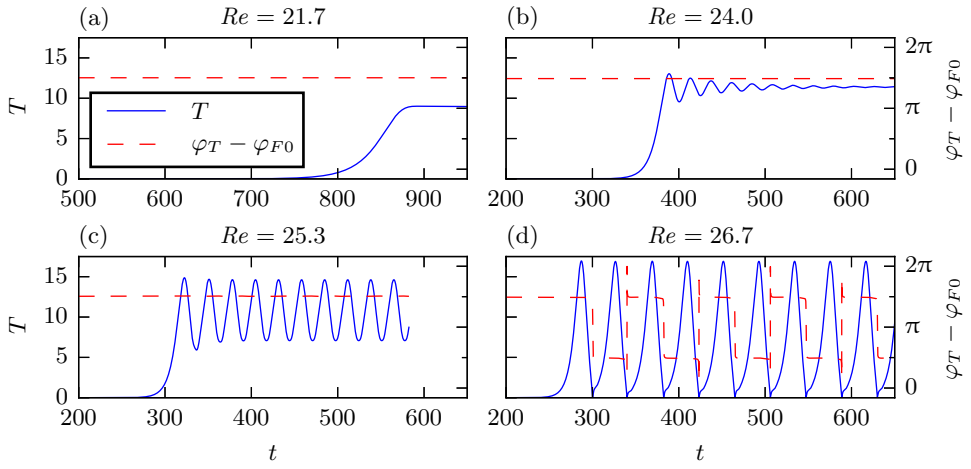

Figure 2.12: Analogous to figure 2.11 above, but now the magnitude of the hydrodynamic torque T (normalized by $2B_1a^2\mu/3$) is plotted along with the angle $\varphi_T - \varphi_{F0}$ that the torque forms with the initial lift force. For all Re shown, the torque is perpendicular to both the direction of translation and the lift.

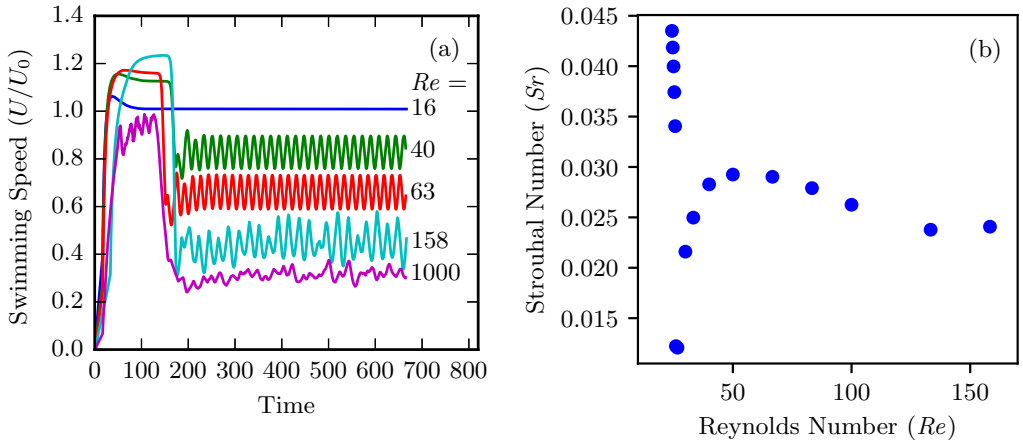

Figure 2.13: (a) Swimming speed vs. time for a $\beta = 5$ puller accelerating from rest (3D simulation). Time is normalized by $3a/(2B_1)$. (b) The Strouhal number Sr vs. Re for a $\beta = 5$ puller.

cause oscillations in the swimming speed when $Re > Re^{(c2)}$. The time-dependent speed of a $\beta = 5$ puller accelerating from rest is shown in figure 2.13a. Note that these oscillations have double the frequency of that in the lift and torque. It is also apparent that the average normalized swimming speed decreases significantly with increasing Re. This can be ascribed to vortex shedding; the drag-reducing effect of the vorticity-trapping wake bubble observed in (unstable) axisymmetric flows is lost as the vorticity is instead shed downstream. This explains the deviation of the unsteady, 3D simulations from the axisymmetric ones seen in figure 2.3 at approximately the same point at which the flow becomes unsteady.

From the dominant dimensional frequency f of the oscillations in the lift force, we define the Strouhal number as $Sr = 3fa/(2B_1)$, which is plotted for a $\beta = 5$ puller in figure 2.13b. A rapid initial decrease of Sr occurs just as Re exceeds $Re^{(c2)}$ and unsteady flow is established. At slightly higher Re, Sr rebounds and maintains a value between 0.024 and 0.029 between $Re = 60$ and $Re = 160$. This can be roughly compared to flow past a no-slip sphere where $Sr_U = fa/U = 0.067$ at $Re_U = 150$ [65, 67].

It is also apparent from figure 2.13a that the flow at $\beta = 5$ transitions from having just a single frequency at $Re = 63$ to appearing nearly chaotic at $Re = 158$. Also, the planar symmetry observed at $Re = 100$ (figure 2.10b) is clearly broken at $Re = 158$ (figure 2.10c). Similar transitions occur for flow past a no-slip sphere in the range $300 < Re_U < 500$, and the fluctuations in the flow become increasingly irregular as Re is further increased, signifying the beginnings of turbulence [67]. This is also observed for a $\beta = 5$ puller at $Re = 1000$, as the increasingly chaotic nature of the flow causes increasingly broadband fluctuations in the swimming speed.

2.4.4 Power expenditure and hydrodynamic efficiency

The dimensionless power $\mathcal{P}$ expended by a squirmer versus Re for $\beta = 0, \pm 0.5$, and ± 5 is shown in figure 2.14a. This is calculated as the rate of work done on the fluid by the tangential motion of the squirmer surface,

$$\mathcal{P} = -\int_S \boldsymbol{n} \cdot \boldsymbol{\sigma} \cdot (v_s \boldsymbol{e}_\theta)\, \mathrm{d}S, \tag{2.10}$$

where $\mathcal{P}$ is normalized by $4B_1^2 a\mu/9$. In axisymmetric flow, (2.10) simplifies to

$$\mathcal{P} = 2\pi \int_0^\pi (2v_s - \omega|_{r=1}) v_s \sin\theta \, \mathrm{d}\theta. \tag{2.11}$$

Additionally, power expended by the squirmer is dissipated viscously by the fluid. The dimensionless rate of viscous dissipation Φ in the flow around a tangentially deforming spherical body can be given in terms of the vorticity and surface velocity [76, 77],

$$\Phi = \int_V \boldsymbol{\sigma} : \nabla \boldsymbol{v} \, \mathrm{d}V = \int_V \boldsymbol{\omega} \cdot \boldsymbol{\omega} \, \mathrm{d}V + 2\int_S v_s^2 \, \mathrm{d}S, \tag{2.12}$$

and at steady-state, $\Phi = \mathcal{P}$. This implies that a squirmer that minimizes the amount of vorticity that it generates in the fluid will also minimize its power expenditure.

In fact, a neutral ($\beta = 0$) squirmer expends the least amount of energy at all Re since it generates no vorticity. In this case, integrating (2.11) gives $\mathcal{P}|_{\beta=0} = 12\pi$ for all Re. We may also integrate (2.11) to give the power expenditure in Stokes flow, $\mathcal{P}|_{Re=0} = 12\pi(2 + \beta^2)/2$ [46], which gives the limits approached by the data in figure 2.14a as $Re \to 0$. As Re is increased, $\mathcal{P}$ increases (if $\beta \neq 0$) due to increased vorticity generation. As shown in figure 2.8, $|\omega|_{\max}$ increases monotonically, scaling with $\sqrt{Re}$ within the boundary layer at large Re. From (2.11) and (2.12), we expect the same scaling for $\mathcal{P}$, which is indeed observed in figure 2.14a. We also observe that $\mathcal{P}(\beta, Re) > \mathcal{P}(\beta, 0)$

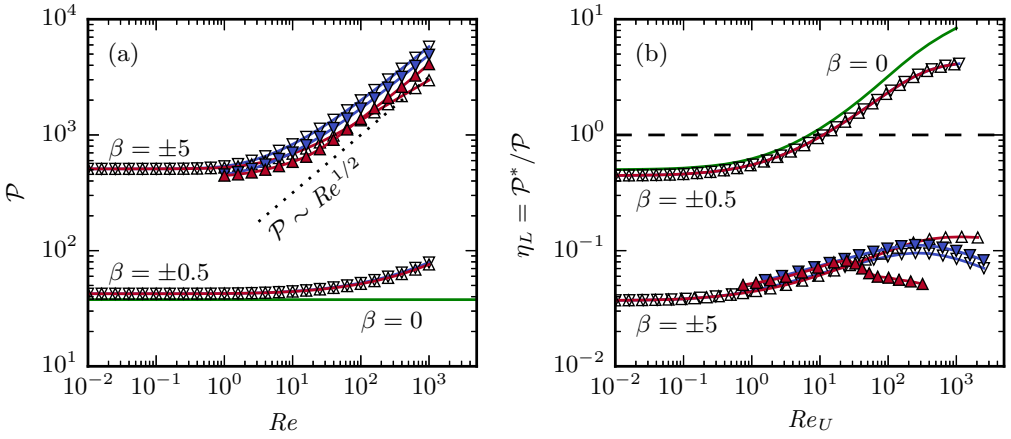

Figure 2.14: Power $\mathcal{P}$ expended by a squirmer versus Re (a), and the Lighthill efficiency η_L versus the translational Reynolds number $Re_U = \varrho U a/\mu$ (b). Here, $\mathcal{P}^*$ is the power necessary to tow a sphere in steady, axisymmetric flow. A neutral ($\beta = 0$) squirmer is indicated by the solid green line (with no markers) and has $\mathcal{P} = 12\pi$ at all Re.

for all $Re > 0$. One might conjecture that this behavior is predicted by the Helmholtz minimum dissipation theorem [78], which guarantees that a Stokes flow field dissipates less energy than any other incompressible flow field with the same boundary velocities. However, the far-field boundary velocity for a squirmer is given by its swimming speed U, which generally depends on Re, so the theorem does not apply. Nonetheless, the observation that $\mathcal{P}$ is minimized at $Re = 0$ for a given value of β is intriguing. Moreover, we observe that $\mathcal{P}$ increases monotonically with Re. This finding may be compared to the monotonic increase of the extensional viscosity of a dilute suspension of rigid spheres with Re in uniaxial extensional flow. Specifically, the extensional viscosity also increases monotonically and scales with $\sqrt{Re}$ at large Re due to intense $O(\sqrt{Re})$ boundary layer vorticity [79]. The extensional viscosity is proportional to the viscous dissipation rate in the flow. Thus, it is an interesting observation that the power expended by a squirmer, which is viscously dissipated, behaves similarly to the extensional viscosity of a dilute suspension of spheres.

The Lighthill [33] efficiency η_L of a squirmer is defined as the ratio of the power $\mathcal{P}^*$ required to tow a no-slip sphere at a speed U to the power $\mathcal{P}$ expended by a squirmer to swim at that same speed. This quantity is plotted in figure 2.14b. Here, the horizontal axis is the Reynolds number based on the translational swimming speed, $Re_U = Re\,U = \varrho U a/\mu$. Note that we take $\mathcal{P}^*$ as the power required to tow a sphere in steady, axisymmetric flow at the same Re_U. At $Re = 0$, $\eta_L = 1/(2+\beta^2)$: pushers and pullers have the same efficiency. At small Re, asymptotic theory shows that pushers are slightly more efficient than pullers [46]. Thus, it would be reasonable to expect that larger differences in efficiency might be observed at larger Re. Interestingly, our results reveal that the difference in efficiency between a $\beta = \pm 0.5$ pusher and puller is very slight, even up to $Re = 1000$. This is somewhat surprising considering that a $\beta = -0.5$ pusher moves nearly 10% faster than a $\beta = 0.5$ puller at $Re = 1000$. Thus, in this case, a puller and pusher exert about the same amount of power once differences in speed are taken into account. Similarly, a $\beta = \pm 5$ puller and pusher have nearly the same efficiency up to the point where the steady, axisymmetric flow destabilizes at $Re_U \approx 20$, with that of a pusher being only slightly greater. If one considers the unstable axisymmetric flow that arises beyond $Re_U \approx 20$, pullers interestingly become *more* efficient than pushers. The drag reducing effect of the Hill's vortex-like wake is responsible. However, if the flow is allowed to be unsteady and 3D, pushers continue to be more efficient by a margin that increases with Re_U. The vortex shedding that takes place in the wake of a high Re puller reduces the amount of swimming work that goes into forward propulsion and causes a subsequent loss of efficiency. This suggests that "pushing" may be more efficient than "pulling" at larger Reynolds numbers due to the increased flow stability.

One may notice that η_L increases above unity in some cases, indicating

that the power required to tow a sphere exceeds that expended by a squirmer swimming at the same speed. In Stokes flow, $\eta_L \leq 3/4$ for any spherical swimmer moving only by tangential surface deformations [77]. For a neutral squirmer at $Re = 0$, $\eta_L = 1/2$. However, this bound does not apply when $Re > 0$. Indeed, $\eta_L|_{\beta=0}$ increases above unity at $Re_U \approx 7$, and the same is true for $\beta = \pm 0.5$ squirmers at $Re_U \approx 10$. This highlights the difficulty of swimming against wholly resistive viscous forces [2]. For a squirmer, swimming is always less efficient than being towed by an external force in the absence of fluid inertia, but may be more efficient when inertia is present.

Finally, we note that the propulsion of a squirmer via tangential surface motion is drag based. This is in contrast to the flapping and undulatory mechanisms of propulsion employed by some (usually large Re) swimmers such as fishes, which are lift based. The efficiency of lift based propulsion can very high in inertial flows where Re is large. However, this efficiency decreases drastically with Re, and drag based propulsion has superior efficiency when fluid viscosity is a strong factor [80]. Thus, without rigorous calculation, we surmise that the efficiency of a squirmer improves compared to lift based propulsion as Re is decreased, likely being comparable at moderate Re. This clearly makes sense from a biological perspective; the ciliated organisms most closely described by the squirmer model are often microorganisms that swim at small Re, although ctenophores provide an interesting example of moderate to large Re squirmers.

2.5 Conclusion

We have demonstrated fundamental differences between the locomotions of pusher and puller squirmers with a fixed swimming stroke when inertia is important to the flow. Specifically, it is shown that a pusher, as well as

a $\beta < 1$ puller, does not generate a standing wake eddy, and also that it produces steady, axisymmetric flow that remains stable to at least $Re = 1000$. The vorticity is confined to a laminar boundary layer of thickness $O(\sqrt{Re})$, and the flow becomes largely irrotational as Re increases. This is due to the strong downstream advection of vorticity by the propulsive surface velocity profile. Before, such behavior has only been demonstrated for bubbles, which produce $O(1)$ vorticity. That this also holds for a $\beta < 1$ squirmer is a key result, as squirmers produce a much larger $O(\sqrt{Re})$ vorticity (similar to a no-slip body).

In contrast, a $\beta > 1$ puller is ineffective at transporting vorticity from its wake, similar to a towed, rigid sphere. Thus, it exhibits a recirculating wake region that triggers a transition to unsteady, 3D flow at a critical Re. A progression of flow patterns is observed as Re is further increased, which strongly resemble those which occur for a rigid sphere, until weakly turbulent flow develops when $Re \sim O(1000)$.

Finally, we show that squirmers that minimize vorticity generation generally maximize their efficiency. In the range of Re where steady, axisymmetric flow is stable, the swimming efficiency of pushers and pullers is surprisingly similar. However, the vortex shedding that occurs for $\beta > 1$ pullers in unsteady, 3D flow at larger Re reduces their overall efficiency below that of a pusher where the axisymmetric flow remains stable.

Future work will entail further quantification of squirmers in unsteady, 3D flows; at sufficiently large Re, the flow around $\beta > 1$ pullers is expected to become fully turbulent, similar to flow around a no-slip body. Furthermore, it would be worthwhile to consider the motion of squirmers that are not bound to move along a single axis of translation. In this case, the motion of the squirmer would be fully coupled to the flow, and different swimming paths would be observed depending upon the values of Re and β. The present results

will be useful in quantifying fluid mixing, production of feeding currents, and hydrodynamic signaling by the abundance of aquatic swimmers living at Re up to 1000.

Chapter 3

Drift volume due to towed bodies

3.1 Introduction

'Drift' refers to the permanent displacement of fluid elements disturbed by the passage of a body through a bulk fluid. Drift is an important heat and mass transport mechanism in natural and industrial processes. For example, heat transfer in pool-boiling is greatly enhanced by the drift induced by rising bubbles that nucleate at the source of heat [81]. In gas-fluidized beds, drift induced by bubbles (or voids) moving through a particulate medium is an important source of mixing [82]. Drift is also relevant to froth floatation, a process used in the mining industry in which rising air bubbles separate minerals from an aqueous slurry. Water carried upward with the bubbles induces recirculation within froth floatation columns, negatively impacting performance [83].

Classic investigations of the trajectories traced out by fluid elements as a result of a passing body date back to Rankine [84] and Maxwell [85], who considered the case of a circular cylinder steadily translating through an inviscid fluid. Fluid elements follow along streamlines in the reference frame that

The content in this chapter has been submitted for publication as a journal article in Physical Review Fluids and is currently under review.

moves with the cylinder. However, a simple Galilean change of reference frame into that in which the fluid far from the cylinder is at rest reveals that, in this frame, fluid elements follow complex, looping paths. Moreover, they are permanently displaced some distance forward after the body is made to travel a long distance. This phenomenon was further investigated by Darwin [22], who referred to it as 'drift.' Darwin introduced the concept of the 'drift volume' to conveniently quantify the net displacement of the entire fluid without the need to explicitly assess the path of each individual fluid element. This concept will be discussed further in what follows below.

Recent interest in drift (and the drift volume) was sparked by the suggestion of Katija and Dabiri [17] that drift is an important mechanism in biogenic ocean mixing. They show drift to be 'viscosity enhanced,' meaning that the total fluid displacement due to a translating body increases with the viscosity of the fluid. This lends support to the possibility that small, millimeter-scale, swimming organisms (such as krill or copepods, which make up the dominant fraction of the oceanic animal biomass) may induce large scale mixing processes [86]. Their work prompted a number of theoretical and experimental investigations into the drift induced by swimmers at small and intermediate Reynolds numbers and its possible impact on ocean stirring [18, 19, 28, 21]. Drift has also been investigated in the context of vortex motion [87, 26], recirculatory wakes behind bluff bodies [88, 89], multi-body problems [90, 91], and protein transport in cellular membranes [92].

The drift volume D is defined as the volume enclosed between the initial and final profiles of a marked (as in with dye) material surface, as the body translates from an infinite distance behind to an infinite distance in front of the plane on which the fluid was initially marked. The initial material plane is infinite in extent and perpendicular to the body's path of motion. Thus, D may be interpreted as the volume of fluid eventually entrained by the passing body.

Darwin's analysis of the drift volume in inviscid flow revealed the remarkable result that $D = m_a/\varrho$, where m_a is the added mass of the body and ϱ is the fluid density. This relation is often referred to as 'Darwin's theorem' or 'Darwin's proposition.' Further proofs of Darwin's theorem were put forth by Yih [93]. The result of the theorem is unexpected in at least two respects. First, the sphere must displace a volume of fluid equal to its own volume as it translates, suggesting there should be a net reflux of fluid opposite to the direction of travel. However, the positive sign of D indicates a net *forward* flux instead. Second, it is not immediately obvious why D should be so closely tied to m_a, although Yih [93] provides a clever geometrical explanation. The added mass describes the apparent additional mass of an accelerating body due to the increasing kinetic energy of the surrounding fluid. The drift volume, in contrast, has no inherent association with such acceleration.

However, caution must be exercised in the application of Darwin's 'theorem,' causing some debate about whether it is more appropriately referred to as a 'proposition' [94, 23, 95]. As pointed out by Darwin himself, the procurement of the relation $D = m_a/\varrho$ is dependent upon the ordering of nested improper integrals involved in computing D, which are taken over all space. Evaluating D amounts to evaluating the total momentum of the fluid (divided by ϱ), which is itself indeterminate [94]. The physical origins of this indeterminacy were elucidated by Eames, Belcher, and Hunt [23], who extended Darwin's concept by introducing the *partial* drift volume $D_p(x_0, h)$, where the body is placed at a finite initial distance x_0 from the marked plane, which is a disc of finite height h. Assuming that h far exceeds the dimensions of the body ($h \to \infty$), one expects to recover $D_p(x_0, h) \to m_a/\varrho$ as the distance of the body behind the marked plane is made infinite ($x_0 \to -\infty$). However, this is only true if $x_0/h \to -\infty$. In fact, D_p depends critically on the ratio x_0/h, although it is always finite and comparable in magnitude to the volume

of the body V_b. For instance, if $x_0/h \to 0^-$, then $D_p(x_0, h) \to -V_b$. In this case, one finds that the drift volume represents a net backward reflux of fluid, itself equal in magnitude to the volume of the body.

A limitation of Darwin's theorem is that it formally applies only to inviscid fluids. Let $Re \equiv 2\varrho U l_c/\mu$ be the Reynolds number, where U is the speed of the body and μ is the fluid viscosity, and l_c is the characteristic length of the body. Darwin's theorem is of practical value only in cases where Re is sufficiently large for the effects of viscosity to be negligible. In such scenarios, where the majority flow is approximately irrotational, experimental results for D indeed exhibit reasonable agreement with the prediction $D = m_a/\varrho$ [96, 97, 87, 26]. However, any body moving through an unbounded fluid by the action of an external force at a finite Re carries with it a viscous wake of nonzero vorticity. The velocity disturbance in the wake decays as $v \sim 1/r$, where v is the magnitude of the velocity disturbance and r is the radial distance from the body [78]. This slow decay suggests that the displacement of any fluid element entrained by the wake diverges logarithmically as the body translates an infinite distance, and thus D is unbounded [18]. Disagreement between Darwin's theorem and experiments on rising bubbles at $Re \approx 100$ can be attributed to this fact [98].

The nature of the drift volume in viscous flows has not been studied to the same extent as in the inviscid case, although there are some theoretical predictions for Stokes flow ($Re = 0$). Eames, Gobby, and Dalziel [27] computed a leading order approximation to D_p induced by a translating spherical droplet of radius a in Stokes flow as $a/h \to \infty$, which is found to diverge with time t (i.e., as the distance traveled by the droplet, Ut, becomes large). This is due to the slow velocity decay of the Stokeslet (force monopole) contribution to the flow, which has $v \sim 1/r$ everywhere. However, it is also found that, if the fluid is bounded by a wall, D_p is instead convergent because v decays faster

than $1/r$ in the far-field, and hence marked fluid elements translate only a finite distance as $t \to \infty$. For a wall parallel to the travel direction, $v \sim 1/r^2$, and for a perpendicular wall, $v \sim 1/r^3$. The drift volume induced by a disc translating through a two-dimensional porous medium has also been considered [92]. Here, D and D_p are also bounded because $v \sim 1/r^2$ at distances greater than the Brinkman screening length, upon which D is shown to be quadratically dependent.

The drift volume induced by a spherical microswimmer (a 'squirmer') of radius a at $Re = 0$ has been investigated by Leshansky and Pismen [19] and Pushkin, Shum, and Yeomans [28]. The flow generated by such a swimmer can be described by a combination of a stresslet (symmetric force dipole) contribution and a potential dipole contribution. Whether the swimmer generates thrust from the front or rear (i.e., is a 'pusher' or 'puller', respectively) is dictated by the sign of the stresslet, while the potential dipole can be interpreted as an irrotational 'treading' of the fluid past the swimmer. There is no Stokeslet contribution to the flow because the swimmer is assumed to be free of external forces and translating steadily. Thus, the stresslet, which has $v \sim 1/r^2$, makes the dominant contribution to the far-field flow. However, its fore-aft symmetric velocity distribution mean that its net contribution to D cancels as the swimmer translates from far behind to far ahead of the initially marked fluid plane. The potential dipole component of the flow ($v \sim 1/r^3$) is left to determine D, and it is found that $D = V_b/2 = 2\pi a^3/3$. The same result is coincidentally recovered for a sphere moving through an inviscid fluid.

The drift volume induced by a body moving through a viscous fluid at finite Re has yet to be quantified in detail. The central goal of the present chapter is to address this knowledge gap. A reasonable suggestion is that D_p should be tied to the volumetric flux Q through the viscous wake downstream of the body. This flux is constant at distances far downstream and is related

to the drag F on the body as $Q = F/\varrho U$ [78]. Therefore, one may surmise that D_p diverges linearly with time as $t \to \infty$, at a rate that is proportional to F [23, 19]. However, this argument assumes that h is always large compared to the traverse size of the wake, which also diverges with the downstream distance. It also neglects the source-like flow emanating from the sphere that compensates the flux through the wake. As we will show, the behavior of D_p at finite Re is more complex than has been previously suggested. Moreover, although D_p always diverges as $t \to \infty$, the nature of this divergence depends critically on assumptions regarding the ratio of the total distance traversed by the sphere to the extent of the marked plane as these quantities are made unboundedly large. This behavior is analogous to the conditional nature of Darwin's theorem, $D = m_a/\varrho$, in inviscid flow.

In the sections to follow, we address the problem of the partial drift volume of a rigid sphere of radius a translating at a steady speed U as a function of $Re = 2\varrho U a/\mu$. We restrict ourselves to the case where $h \gg a$, since this is typically of greatest interest, and because it allows us to make asymptotic approximations to D_p. In section 3.2, we generalize the partial drift volume concept to finite travel times by introducing a definition that we show to have two distinct geometrical interpretations. Another way of doing so is given by Camassa et al. [99], but their argument requires v to decay faster than $1/r$ in the far-field. The flux argument that we develop has no such limitation, and thus we may readily apply it to unbounded Stokes flows and flows at finite Re (where the velocity in the wake decays as $1/r$). We first review the classic inviscid flow problem in section 3.3, where we validate our method of computing $D_p(t)$ against previous analytical results. From there, we consider Stokes flow in section 3.4, where a two-term asymptotic expansion for $D_p(t)$ is derived for $h/a \gg 1$. In section 3.5, we obtain an approximation to D_p at small Re using Oseen's approximation of the flow. Finally, we consider

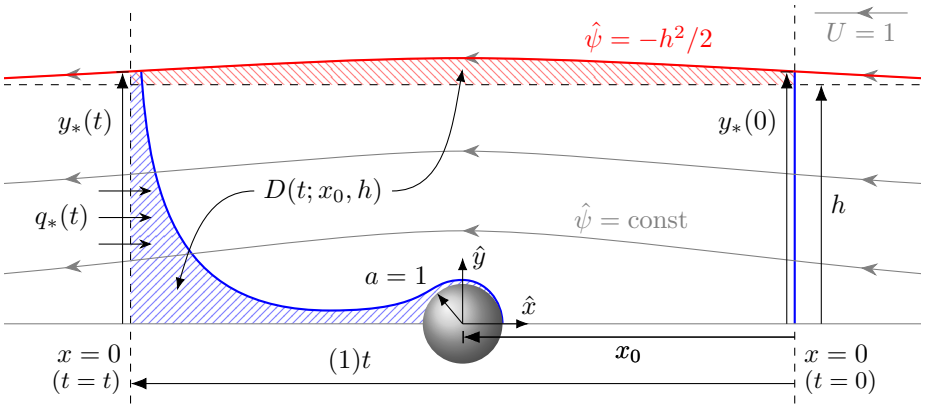

Figure 3.1: An illustration of the drift volume in the co-moving frame, in which a uniform flow approaches a sphere of unit radius from the right at unit velocity. At $t = 0$, the fluid is marked at $x = 0$ for $y < y_*(0)$, as indicated by the solid line to the right of the sphere. The sphere is at an initial distance x_0 from the $x = 0$ plane. At time $t > 0$, the sphere translates a distance of $(1)t$ toward and eventually past $x = 0$, causing the marked fluid to deform. The volume swept out by the marked fluid at time t is indicated by the shaded area to the left of the sphere and is defined to be the drift volume, $D(t; x_0, h)$. The fluid volume between $y = h$ and the streamline $\hat{\psi} = -h^2/2$, represented by the shaded area above the sphere, is also equal to D. The rate at which D increases with t is equal to the volumetric flux, $q_*(t)$, through $x = 0$ for $y < y_*(t)$.

the drift volume associated with the point force solution to Oseen's equations, which gives a general estimate of D_p for a body translating in steady, laminar flow. A brief discussion of the overall results is presented in section 3.7, which are finally summarized in section 3.8. For brevity, we will henceforth use the term 'drift volume' to refer to the partial drift volume D_p as a general function of t, x_0, and h, and we will omit the subscripted 'p'.

3.2 Definition of the drift volume

Consider an impermeable sphere of radius a translating steadily through an unbounded fluid at speed U in the positive direction along the x-axis (figure 3.1). We will normalize distance by a and time t by a/U, and all quantities defined henceforth will be dimensionless unless stated otherwise. Let the y-coordinate

measure the distance from the x-axis, such that (x, y) specifies a position in a cylindrical coordinate system in which the fluid far from the sphere is at rest (the fixed frame). The flow is assumed to be axisymmetric about the x-axis so that there is no dependence on the azimuthal angle. At $t = 0$, let the initial position of the sphere be $(x_0, 0)$. Also, in the frame that is co-moving with the sphere, let $\hat{x}$ and $\hat{y}$ be the coordinates centered on the sphere such that $\hat{x} = x-(x_0+t)$ and $\hat{y} = y$. The flow is assumed to be steady in this frame, and thus it may be described by a stream function $\hat{\psi}(\hat{x}, \hat{y})$, which is normalized by Ua^2 and tends toward $-\hat{y}^2/2$ in the far-field. At $t = 0$, the fluid on the $x = 0$ plane is marked (as in with dye) for $y < y_*(0)$, where the point $(0, y_*(t))$ is the intersection of the $x = 0$ plane with the streamline, $\hat{\psi} = -h^2/2$, that approaches $y = h$ as $x \to \pm\infty$. Driven by the motion of the sphere, the marked fluid deforms as time progresses from $t = 0$. Now, consider the fluid enclosed by the $x = 0$ plane, the marked material surface of fluid, and the fluid lying on $\hat{\psi} = -h^2/2$, which also constitutes a material surface. Let the (dimensionless) drift volume $D = D(t; x_0, h)$ be defined as the volume of fluid, normalized by a^3, contained within this region at a particular time $t > 0$, which is depicted as the shaded area trailing the sphere in figure 3.1. The partial drift volume, as defined by Eames, Belcher, and Hunt [23], is reproduced in the limit $t \to \infty$, as the streamlines become flat at an infinite downstream distance from the sphere. Darwin's drift volume is also reproduced upon letting $x_0 \to -\infty$, $t \to \infty$, and $h \to \infty$ (although the ordering of these limits requires care, as we will discuss later).

This definition of the drift volume is particularly useful because it reveals that D may be interpreted as the time-integrated flux through a kinematic surface within the fluid domain. Let $A = A(t)$ represent such a surface lying on $x = 0$ for $y < y_*(t)$ (with area πy_*^2), and let $q_* = q_*(t)$ represent the volumetric flux through A. All boundaries of the region defining the drift

volume are material surfaces except A, including the surface of the sphere itself. Therefore, a material balance dictates that $D = \int_0^t q_*(t)\,dt$. Our flux interpretation of D is similar to that of Benjamin [94]; it only differs in that we bound A by a streamline (or, more accurately, a stream tube), rather than by an arbitrary time-independent circle of constant radius ($> a$). Our modification ensures that $D(t \to \infty; x_0, h)$ is consistent with the partial drift volume considered by Eames, Belcher, and Hunt [23].

Let $\psi(x, y, t) = \hat{\psi}(\hat{x}, \hat{y}) + \hat{y}^2/2$ represent the instantaneous stream function of the flow in the fixed frame. The difference in ψ between any two points is equivalent to (2π times) the flux through any instantaneous axisymmetric surface connecting those points. Thus, we may evaluate the flux through $A(t)$ as $q_*(t) = 2\pi[\psi_*(t) - \psi_b(t)]$, where $\psi_*(t) = \psi(0, y_*(t), t)$, and $\psi_b(t)$ is ψ evaluated at the intersection of the $x = 0$ plane with the sphere's surface. When there is no intersection, $\psi_b = 0$. Integrating $q_*(t)$ over time yields

$$D = 2\pi \int_0^t [\psi_*(t') - \psi_b(t')]\,\mathrm{d}t' = 2\pi \int_0^t \psi_*(t')\,\mathrm{d}t' - \left[\bar{V}_b(t) - \bar{V}_b(0)\right], \tag{3.1}$$

where $\bar{V}_b(t)$ is the volume of the sphere (normalized by a^3) that has passed through $x = 0$ at time t. The second equality in (3.1) holds as long as the sphere is impermeable.

There is a second possible interpretation of the drift volume. An implicit relation between ψ_* and y_* is given by

$$\psi_* = \frac{1}{2} y_*^2 - \frac{1}{2} h^2. \tag{3.2}$$

Inserting (3.2) into (3.1) gives

$$D = \pi \int_0^t y_*^2(t')\,\mathrm{d}t' - \pi h^2 t - \left[\bar{V}_b(t) - \bar{V}_b(0)\right]. \tag{3.3}$$

The first two terms on the right hand side of (3.3) evidently describe a volume of revolution about the x-axis that is bounded above by $\hat{\psi} = -h^2/2$ and

below by $y = h$, as highlighted in figure 3.1. The equivalence of D to the volume between this streamline and its unperturbed (free-stream) position can be realized by a direct geometrical argument [93] that has been utilized by others [27, 19, 28]. However, the flux interpretation that we outlined here has not been previously emphasized, and thus it is worth pointing out the mathematical equivalence between these two interpretations of D.

Solving (3.2) for ψ_* as an explicit function of time in the interest of evaluating (3.1) is complicated by the fact that $\psi(x, y, t)$ is generally a nonlinear function of space and time. To ameliorate this issue, and because we are primarily concerned with the motion of the entirety of the bulk fluid as the sphere translates, we will restrict our attention to the case where $h \gg 1$, i.e., where the radius of the marked disc of fluid is large compared to that of the sphere. Then, $y_*/h \sim 1$ for all t since the departure from the uniform stream is small far from the sphere. In this case, it is convenient to define $\tau = (x_0 + t)/h$ and $\rho = y_*/h$. We may rearrange and express (3.2) in terms of these variables as

$$\rho^2 = 1 + \frac{2\psi_*}{h^2}. \tag{3.4}$$

The integral for the drift volume from (3.1) then becomes

$$D = 2\pi h \int_{\tau_0}^{\tau} \psi_*(\tau')\,\mathrm{d}\tau' - \left[\bar{V}_b(\tau) - \bar{V}_b(\tau_0)\right], \tag{3.5}$$

where $\tau_0 = \tau|_{t=0} = x_0/h$. For brevity, we will make use of the function $\Delta(\tau; h) = D(\tau, \tau_0 = 0, h)$, from which $D(\tau) = \Delta(\tau) - \Delta(\tau_0)$. We may interpret $\Delta(\tau)$ as the 'downstream' drift volume, occurring after the center of the sphere has crossed $x = 0$. Conversely, $-\Delta(\tau_0)$ is the 'upstream' drift volume occurring before the center of the sphere crosses $x = 0$.

3.3 Inviscid flow

The flow due to a sphere passing through an inviscid fluid is described by a potential dipole at the center of the sphere. Thus, the instantaneous stream function in the fixed frame evaluated at $(0, y_*(t))$ is given by

$$\psi_* = \frac{\rho^2}{2h(\tau^2+\rho^2)^{3/2}}. \tag{3.6}$$

Inserting (3.6) into (3.4) yields a nonlinear equation for $\rho(\tau)$,

$$\rho^2 = 1 + \frac{\rho^2}{h^3(\tau^2+\rho^2)^{3/2}}. \tag{3.7}$$

For $h \gg 1$, (3.7) makes apparent that there is only a very small, $O(1/h^3)$, deflection from the free-stream flow. This suggests that we may make a leading order approximation to D by setting $\rho = 1$ in (3.6). Hence, from (3.5), an approximation to the drift volume is

$$D \sim D_0 = 2\pi \int_{\tau_0}^{\tau} \frac{\mathrm{d}s}{s^2+1} - \left[\bar{V}_b(\tau) - \bar{V}_b(\tau_0)\right]. \tag{3.8}$$

Evaluating (3.8) gives

$$\Delta \sim \Delta_0 = \frac{\pi\tau}{\sqrt{\tau^2+1}} - \bar{V}_b(\tau). \tag{3.9}$$

This approximation to the drift volume is essentially the same as that considered by Benjamin [94]. We may physically interpret D_0 as the volume of fluid through a disc of radius h at $x = 0$, since we have effectively neglected the deflection of streamlines far from the sphere. Interestingly, the drift volume only depends on x_0, h, and t through τ (and τ_0) at this level of approximation. The fact that h does not appear in (3.9) indicates that D converges to an $O(1)$ value as the height of the marked plane is made large. Also, we observe that $\Delta_0(\tau) = -\Delta_0(\tau_0)$ due to the fore-aft symmetry of the flow.

If an unbounded marked plane ($h \to \infty$) is considered, corresponding to Darwin's original calculation, then the error incurred by setting $\rho = 1$ in (3.6)

approaches zero, and $D \to D_0$. However, this places no restriction on the values of x_0 or t, which may be unboundedly large. The ratios τ and τ_0 are in this case indeterminate and must be specified for $D(\tau)$ to be well defined [94, 23]. In order to recover the equivalence of the drift volume (multiplied by the fluid density) to the added mass, as originally done by Darwin, the distance traveled by the sphere must be assumed to be infinitely large compared to the marked plane. This corresponds to letting $\tau_0 \to -\infty$ and $\tau \to \infty$ in (3.9). From this, we obtain the expected result that $D = 2\pi - V_b = 2\pi/3$, where V_b is the total (nondimensional) volume of the sphere, $4\pi/3$. If instead the path traversed by the sphere is infinitesimal compared to h (although large compared to a), then $\tau \to 0$ for all t. The first term in (3.9) consequently vanishes, and $D = -V_b = -4\pi/3$ (a result that was also obtained by Darwin). Finally, τ or τ_0 may be taken as finite, in which case intermediate values of D are obtained. However, despite its conditional nature, D is always comparable in magnitude to V_b.

We may obtain corrections to $D(\tau; \tau_0, h)$ for large (but finite) h by an asymptotic expansion in terms of the small parameter $\varepsilon = 1/h$. In this manner, the effect of the small deflection of the streamline $\hat{\psi} = -h^2/2$ may be accounted for. (3.6) suggests an expansion for $\rho(\tau; \varepsilon)$ of the form $\rho^2 = 1 + \varepsilon^3 \rho_3^2(\tau) + \varepsilon^6 \rho_6^2(\tau) + O(\varepsilon^9)$. After substituting this series into (3.7) and expanding each term as a Taylor series about $\varepsilon = 0$, matching like powers of ε gives

$$\rho^2 = 1 + \frac{\varepsilon^3}{u^3} + \varepsilon^6 \left(\frac{1}{u^6} - \frac{3}{2u^8} \right) + O\big(\varepsilon^9\big), \tag{3.10}$$

where $u = \sqrt{\tau^2 + 1}$. We may directly obtain a corresponding expansion for ψ_* using (3.4); namely,

$$\psi_* = \frac{\varepsilon}{2u^3} + \varepsilon^4 \left(\frac{1}{2u^6} - \frac{3}{4u^8} \right) + O\big(\varepsilon^7\big). \tag{3.11}$$

This may be substituted into (3.5) and integrated by making the hyperbolic substitution $\tau = \sinh\theta$ and applying the reduction formula $(n-1) \int \operatorname{sech}^n \theta \, \mathrm{d}\theta =$

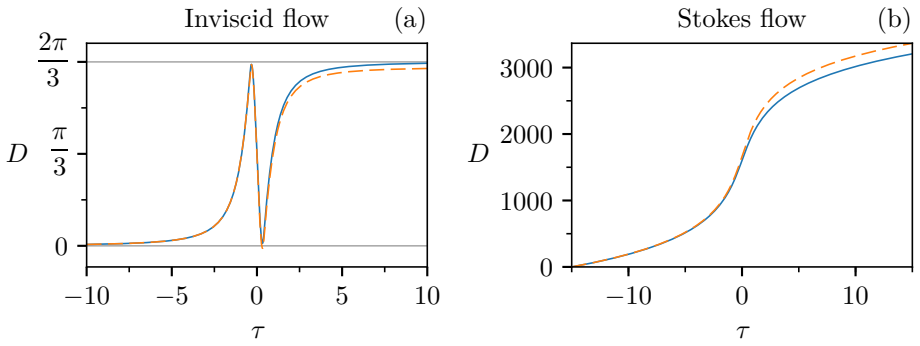

Figure 3.2: The drift volume D (normalized by a^3) for a rigid sphere in inviscid flow (a) and in Stokes flow (b). The solid lines represent the leading order approximations to D from Equation (3.9) and (3.15), respectively, and the dashed lines represent the asymptotic corrections given by Equation (3.12) and (3.16), respectively. In (a), $h = 2.5$ and $\tau_0 \to -\infty$. The sharp drop in D at $\tau = 0$ is the result of the sphere displacing fluid as it passes through the $x = 0$ plane. Darwin's result that $D = 2\pi/3$ is approached as τ becomes large. In (b), we have taken $h = 10$ and $\tau_0 = 15$. Note that the magnitude of D in Stokes flow is orders of magnitude greater than that in inviscid flow.

$\operatorname{sech}^{n-2}\theta \tanh\theta + (n-2)\int \operatorname{sech}^{n-2}\theta \, \mathrm{d}\theta$. The expansion $\Delta(\tau;\varepsilon) = \Delta_0(\tau) + \varepsilon^3\Delta_3(\tau) + O(\varepsilon^6)$ is thereby obtained, where

$$\Delta_3(\tau) = -\frac{\pi}{32}\left[3\tan^{-1}\tau + \frac{3\tau}{(\tau^2+1)} + \frac{2\tau}{(\tau^2+1)^2} + \frac{8\tau}{(\tau^2+1)^3}\right]. \tag{3.12}$$

From (3.12), we observe that Δ_3 decreases (very nearly) monotonically with τ (the last bracketed term produces weak non-monotonicity). Therefore, Δ_3 represents a reflux of fluid opposite to the direction of travel. Taking the limit of D as $\tau \to \infty$ and $\tau_0 \to -\infty$, all of the bracketed terms in (3.12) vanish except for the monotonic $\tan^{-1}\tau$ term. Thus, $D = 2\pi/3 - 3\pi^2\varepsilon^3/32 + O(\varepsilon^6)$. The results for $D(\tau;\tau_0,h)$ given by (3.9) and (3.12) are plotted in figure 3.2(a). They are consistent with other asymptotic analyses of the drift volume in inviscid flow [23, 99] and serve to validate our method for computing D.

3.4 Stokes flow

Repeating the analysis for Stokes flow ($Re = 0$) past a rigid spherical particle with a no-slip surface is straightforward; the procedure requires little modification from the inviscid flow case considered in section 3.3. Here, the stream function at $(0, y_*(t))$ is

$$\psi_* = \frac{3h}{4}\frac{\rho^2}{(\tau^2+\rho^2)^{1/2}} - \frac{1}{4h}\frac{\rho^2}{(\tau^2+\rho^2)^{3/2}}. \tag{3.13}$$

The large, $O(h)$ term in (3.13) is contributed by the Stokeslet, which dominates the flow far from the sphere. The much weaker $O(1/h)$ term is due to a potential dipole contribution to the flow, required to satisfy the no-slip condition at the sphere surface (it is of the same form that appears in (3.6)).

Inserting (3.13) into (3.4) gives

$$\rho^2 = 1 + \frac{3}{2h}\frac{\rho^2}{(\tau^2+\rho^2)^{1/2}} - \frac{1}{2h^3}\frac{\rho^2}{(\tau^2+\rho^2)^{3/2}}. \tag{3.14}$$

Compared to the inviscid case, where the deflection from the uniform stream is only $O(h^{-3})$ (see (3.7)), (3.14) shows a more significant $O(h^{-1})$ deflection. Nonetheless, the flow is approximately uniform far from the sphere, and a leading order approximation to $D(\tau; \tau_0, h)$ may again be obtained by neglecting the vertical deflection of streamlines for $h \gg 1$. Setting $\rho = 1$ in (3.13) and evaluating the resulting integral in (3.5) yields

$$\Delta \sim \Delta_0 = \frac{3\pi}{2}h^2 \sinh^{-1}\tau, \tag{3.15}$$

which we plot with $h = 10$ in figure 3.2(b). Note that Eames, Gobby, and Dalziel [27] obtain a similar result, which can be verified to be in agreement with (3.15) after rewriting τ in terms of the angle θ, with reference to the center of the sphere, subtended by the x-axis and the point $(0, y_*)$ at time t. Namely, it can be shown that $\sinh^{-1}\tau = \sinh^{-1}(-\cot\theta) = \ln\left(\tan\frac{1}{2}\theta\right)$.

The sole term in (3.15) is contributed by the Stokeslet and is $O(h^2)$. Other contributions to $\Delta(\tau; h)$ coming from the second term in (3.13) and $\bar{V}_b(\tau)$ are only $O(1)$. Hence, they are omitted from (3.15), which, as we will formally show below, has $O(h)$ error. From this leading order result, we find that $\Delta(\tau) = -\Delta(\tau_0)$, which is due to the fore-aft flow symmetry and is a property that is shared with the inviscid flow case. However, we also observe that D diverges linearly with the area, projected onto a plane perpendicular to the x-axis, of the marked fluid as $\tau \to \infty$, πh^2, and hence quadratically with h. It also diverges logarithmically with τ as $\tau \to \infty$ (since $\sinh^{-1}\tau \sim \ln\tau$ for $\tau \gg 1$), and there is a similar divergence as $\tau_0 \to -\infty$ (as the initial distance of the sphere from the marked fluid is made large). This behavior contrasts drastically with that found for inviscid flow, where D converges to an $O(1)$ value as $h \to \infty$ and $t \to \infty$. The divergent nature of D in Stokes flow can be attributed to the slow $1/r$ decay of the velocity disturbance. The total horizontal displacement of marked fluid elements $X(t)$ (in the fixed frame) scales as $X \sim \int^t \mathrm{d}t/t = \ln t$ as $t \to \infty$. This can be compared with the far weaker $v \sim 1/r^3$ decay in inviscid flow, which leads to a bounded fluid displacement; $X \sim 1/t^2$ as $t \to \infty$.

Recall the indeterminant nature of $D(t; x_0, h)$ in inviscid flow, which is in turn due to assumptions made regarding τ as $x_0 \to \infty$, $t \to \infty$ and $h \to \infty$. The same issue must be addressed for Stokes flow. If we allow that $\tau = (x_0 + t)/h \gg 1$, so that the path of travel far exceeds h, then D diverges logarithmically with t according to (3.15). However, if the path of travel is not large compared to h, such that $\tau = (x_0 + t)/h \ll 1$ for all t, then (3.13) gives $\psi_* \sim 3h/4$, which is interestingly independent of τ. This implies a constant volumetric flux through all planes perpendicular to the x-axis, and hence that $D \sim 3\pi h t/2$. Thus, D diverges linearly, rather than logarithmically, with t at long times in this case. This behavior is also contained within (3.15), which

can be verified by evaluating the Taylor expansion of $\Delta_0(\tau; h)$ about $\tau = 0$ to leading order in τ.

Corrections to Δ_0 for small but finite $\varepsilon = 1/h$ may be obtained in the same manner as for the inviscid flow case, with the exception that ρ^2 must be expanded in powers of ε instead of ε^3, as indicated by the presence of an $O(\varepsilon)$ term in (3.14). Performing the expansion yields

$$\Delta = \frac{3\pi}{2} h^2 \sinh^{-1}\tau + h\left(\frac{27\pi}{16}\tan^{-1} s - \frac{9\pi s}{16(s^2+1)}\right) + O(1). \tag{3.16}$$

The second term in (3.16) represents an $O(h)$ correction to the leading order result, Δ_0, from (3.15). It increases monotonically, therefore representing a net drift of fluid in the same direction as the sphere, rather than a reflux, as was found for the analogous correction in inviscid flow (3.12). This may be attributed to the fact that, in Stokes flow, the velocity in the fixed frame is everywhere in the direction of travel, and the corresponding streamlines are therefore open. In inviscid flow, the streamlines are closed in loops, and the flow moves opposite to the direction of travel for $\hat{y}^2 > 2\hat{x}^2$. Note that the correction to $\Delta(\tau; h)$ in (3.16) is more significant compared to that for inviscid flow in the sense that its magnitude differs from the leading order term by a factor of $1/h$, as compared to $1/h^3$.

3.5 Small Reynolds numbers

To quantify the effect of inertia on the drift volume, we first consider Oseen's approximation to the flow for $Re \ll 1$ [100]. In this approximation, the stream function for the flow produced by a steadily translating rigid sphere with a no-slip surface evaluated at $(0, y_*(t))$ is

$$\psi_* = \frac{3}{Re}\left(1 + \frac{\tau}{\sqrt{\tau^2+\rho^2}}\right)\left\{1 - \exp\left[-\frac{Re\, h}{4}\left(\sqrt{\tau^2+\rho^2} - \tau\right)\right]\right\} - \frac{1}{4h}\frac{\tau^2}{(\tau^2+\rho^2)^{3/2}}. \tag{3.17}$$

We anticipate that the 'Oseenlet' (i.e., the solution to Oseen's equations for a point force), represented by the first term in (3.17), will make the dominant contribution to D. Hence, the $O(1)$ contribution of the remaining potential dipole term is neglected, and the $\bar{V}_b(\tau)$ contribution from (3.5) is omitted for the same reason. Finally, the deflection of the $\hat{\psi} = -h^2/2$ streamline, which we expect to have a relatively small effect on D, is neglected by setting $\rho = 1$. With these approximations, (3.17) in (3.5) gives

$$D_0 = \frac{6\pi h}{Re} \int_{\tau_0}^{\tau} \left(\frac{s}{\sqrt{s^2+1}} + 1 \right) \left\{ 1 - \exp\left[-\frac{Re\, h}{4} \left(\sqrt{s^2+1} - s \right) \right] \right\} \mathrm{d}s, \quad (3.18)$$

which represents a first approximation to D for $h \gg 1$ and $Re \ll 1$. By making the substitution $u(\tau) = \sqrt{\tau^2+1} - \tau$, (3.18) may be simplified to

$$D_0 = \frac{6\pi h^2}{Re_h} \int_{u(\tau_0)}^{u(\tau)} \left[1 - \exp\left(-\tfrac{1}{4}\, Re_h\, u \right) \right] \mathrm{d}\left(\frac{1}{u} \right), \quad (3.19)$$

where $Re_h = Re\, h$ is the Reynolds number based on h. Evaluating (3.19) in terms of the exponential integral, $E_1(z) \equiv \int_z^\infty \exp(-x)/x \, \mathrm{d}x$, gives

$$\Delta_0(u) = \frac{3\pi h^2}{2} \left[\frac{1 - \exp\left(-\frac{1}{4}\, Re_h\, u \right)}{\frac{1}{4}\, Re_h\, u} + E_1\left(\tfrac{1}{4}\, Re_h\, u \right) \right] - C, \quad (3.20)$$

where

$$C = \frac{3\pi h^2}{2} \left[\frac{1 - \exp\left(-\frac{1}{4}\, Re_h \right)}{\frac{1}{4}\, Re_h} + E_1\left(\tfrac{1}{4}\, Re_h \right) \right].$$

The magnitude of Re_h, which (3.20) suggests is centrally important to the behavior of $D_0(\tau)$, quantifies how much the motion of the marked fluid is influenced by inertial versus viscous forces. It may be interpreted as the ratio of the height of the marked fluid h to the distance from the sphere, $r \sim 1/Re \gg 1$, at which inertial and viscous forces balance. The general pattern of flow around the sphere is illustrated in figure 3.3. Viscous forces dominate where $r \ll 1/Re$, in the 'Stokes' region, but are balanced by inertial forces at $r = O(1/Re)$, in the 'Oseen' region. At distances far into the Oseen region, where $r \gg 1/Re$, inertia dominates, and the majority of the flow is

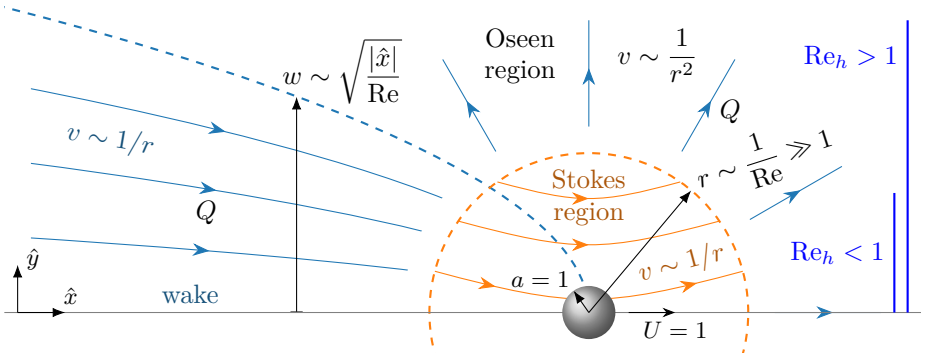

Figure 3.3: A sketch of the flow pattern produced by a rigid sphere translating steadily at $Re \ll 1$. Here, r is the radial distance from the sphere, v is the magnitude of the velocity disturbance, and w is the transverse dimension of the parabolic wake. There is a constant volumetric flux Q through the wake that is compensated by the source-like flow in remainder of the Oseen region. The solid vertical lines to the right of the sphere represent the vertical extent of the initially marked fluid.

irrotational with a source-like character. However, the Oseen region features a parabolic wake downstream of the sphere where viscous forces remain relevant, even far outside of the Stokes region. The width of the wake as a function of the distance downstream of the sphere is described by $w \sim \sqrt{-\hat{x}/\,Re}$, and hence $w|_{x=0} \sim h\sqrt{\tau/\,Re_h}$. It follows that the size of the wake is comparable to the height of the marked fluid ($w \sim h$) when $\tau \sim Re_h$. Therefore, Re_h has the second interpretation of being the dimensionless distance downstream of the sphere beyond which the majority of the marked fluid becomes entrained by the viscous wake.

The result from (3.20) is shown in figure 3.4, where we have normalized D_0 by h^2 in order to collapse (3.20) to a single curve for each value of Re_h. Here, $Re_h = 0$ corresponds to the leading order result for Stokes flow. Indeed, (3.15) is recovered asymptotically from (3.20) as $Re_h \to 0$ because the Stokes region grows unboundedly large in this limit. To show this formally, we see that if $Re_h\, u \ll 1$, then the first bracketed term in (3.20) approaches unity while the second term yields $E_1(Re_h\, u/4) \sim -\ln u(\tau) = \sinh^{-1}\tau$. Thus, $D_0(\tau) \to -\ln u(\tau) = \sinh^{-1}\tau$ as $Re_h \to 0$. When Re_h is nonzero but much

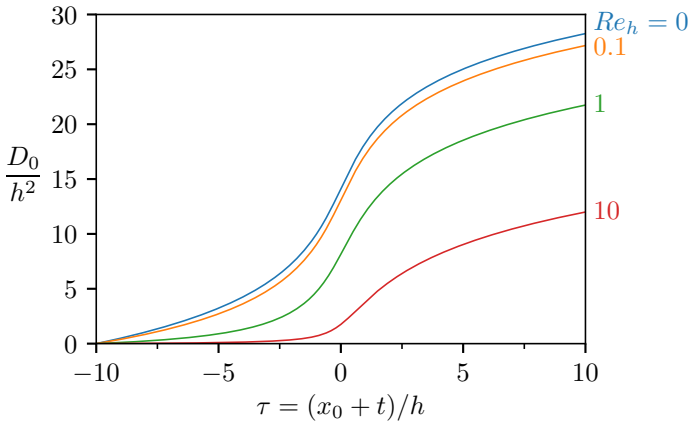

Figure 3.4: The leading order drift volume $D_0(\tau; \tau_0, Re_h)$ normalized by h^2 for $Re \ll 1$, as given by (3.20), where we have set $\tau_0 = -10$. The value of Re_h is indicated to the right of each curve.

less than unity, the Stokes region is finite in size but still large compared to h, and the majority of the marked fluid is completely contained by the Stokes region as long as $|\tau| < 1/\,Re_h$. Hence, D_0 is only marginally different than the Stokes flow prediction in this case, as is observed in figure 3.4 for $Re_h = 0.1$.

As Re_h increases, the Stokes region becomes smaller compared to the height of the marked fluid, and inertia has an increasing effect on D_0. From figure 3.4, it is apparent that there is an overall decrease in D_0/h^2 with increasing Re_h, or, equivalently, a decrease in D_0 with increasing Re given a fixed value of h. The reason is that the regions of flow that are dominated by viscous forces shrink in extent as Re is increased; the radius of the Stokes region decreases as $1/\,Re$, and the wake narrows as $1/\sqrt{Re}$. These regions are of utmost importance to generating drift because they are characterized by a velocity disturbance that exhibits a slow $1/r$ decay and moves fluid in the same general direction as the sphere, even at large distances (figure 3.3). In the part of the Oseen region outside of the wake, inertia causes the velocity to drop off more rapidly as $1/r^2$, and this much weaker flow contributes comparatively little to the drift volume.

Important differences between the nature of the drift volume at finite Re

and that at $Re = 0$ arise from the breaking of the fore-aft flow symmetry by fluid inertia. The asymmetry is greatest in the Oseen region due to the presence of the wake, and thus the influence of inertia is felt most when the majority of the marked fluid resides here, i.e, when $Re_h \geq O(1)$. In contrast, the Stokes region makes a symmetric contribution to the drift volume that fades away as Re_h is made large. (3.20) reveals that $\Delta(\tau) \neq -\Delta(\tau_0)$, whereas this inequality is an equality for inviscid and Stokes flows due to their fore-aft symmetry. Because the flow disturbance inside the wake is significantly stronger than that in the remainder of the Oseen region, the drift volume accumulated for $\tau > 0$ (i.e., after the sphere has passed through $x = 0$) is significantly greater than that for $\tau < 0$, and it becomes increasingly so as Re_h is increased (figure 3.4).

Furthermore, the slowly decaying velocity disturbance in the wake ($v \sim 1/r$) causes the marked fluid to be displaced an infinite distance, $X \sim \ln(\tau)$, as $\tau \to \infty$. The height of the wake diverges with the distance downstream, albeit slowly, as $w \sim \sqrt{|\hat{x}|/\,Re}$. As a result, all of the marked fluid is eventually entrained by the wake as $\tau \to \infty$, regardless of the value of Re_h. Therefore, the logarithmic divergence of D as $\tau \to \infty$, found also for Stokes flow, persists at finite Re as the sphere passes far ahead of the $x = 0$ plane. Assuming that $Re_h \geq O(1)$, the majority of the marked fluid is outside of the Stokes region and entrained by wake once $\tau \geq O(Re_h)$. Thus, we find from (3.20) that $D_0 \sim \ln \tau$ for $\tau \gg Re_h$, since $u(\tau) \sim 1/2\tau$ for $\tau \gg 1$.

However, D converges as $\tau_0 \to -\infty$ at finite Re, unlike at $Re = 0$, where it is divergent. In Stokes flow, the 'symmetric' logarithmic divergence of D as $\tau \to \infty$ and as $\tau_0 \to -\infty$ is due to the fore-aft flow symmetry. Viscous forces dominate everywhere if $Re = 0$, and hence $v \sim 1/r$ everywhere far downstream and upstream of the sphere. Such symmetry is not present if Re is finite. Although viscous forces remain important far downstream in

the wake, they become negligible everywhere else in the Oseen region, where v drops more rapidly as $1/r^2$. Consequently, fluid elements upstream of the wake are not displaced nearly as far, and D_0 converges as $\tau_0 \to \infty$. For $\tau_0 \ll -1$, $u(\tau) \sim -2\tau$, and thus (3.20) shows that $\Delta_0(\tau_0) \sim -2/(Re_h\,\tau_0) - C \to -C$ as $\tau_0 \to -\infty$. Interestingly, this reveals that the constant C represents $D(\tau = 0; \tau_0 \to -\infty, h)$, which is finite.

3.6 Point sources of momentum and wakes

At distances much greater than its radius, the sphere appears as a steady, translating point source of momentum (or vorticity) in an otherwise quiescent fluid, even if $Re \geq O(1)$, granted that Re is not so large as to render the steady, axisymmetric flow unstable. In this case, the far-field flow is described by a steady Oseenlet of strength proportional to the external force $F = F(Re)$ required to tow the sphere [29], where F is normalized by $\varrho U^2 a^2$. This ignores the details of the flow in the immediate neighborhood of the sphere, but they are evidently unimportant for making a leading order approximation to $D(\tau; \tau_0, h)$ when $h \gg 1$, since doing so only requires knowledge of ψ at $r \geq O(h)$. At these far distances, the streamlines are nearly straight and parallel ($\rho \approx 1$). Therefore, for $h \gg 1$,

$$\psi_* \sim \frac{F}{4\pi}\left(1 + \frac{\tau}{\sqrt{\tau^2+1}}\right)\left\{1 - \exp\left[-\frac{Re_h}{4}\left(\sqrt{\tau^2+1} - \tau\right)\right]\right\}. \tag{3.21}$$

Inserting (3.21) into (3.5), making the substitution $u = \sqrt{\tau^2+1} - \tau$, and integrating (omitting the $O(1)$ contribution by $\bar{V}_b(\tau)$) gives

$$\Delta_0 = \frac{F\,Re\,h^2}{8}\left[\frac{1 - \exp\left(-\frac{1}{4}\,Re_h\,u\right)}{\frac{1}{4}\,Re_h\,u} + E_1\left(\tfrac{1}{4}\,Re_h\,u\right)\right] - C, \tag{3.22}$$

where $C = D(\tau = 0; \tau_0 \to -\infty, h)$ and is given by

$$C = \frac{F\,Re\,h^2}{8}\left[\frac{1 - \exp\left(-\frac{1}{4}\,Re_h\right)}{\frac{1}{4}\,Re_h} + E_1\left(\tfrac{1}{4}\,Re_h\right)\right].$$

The $Re \ll 1$ result (3.20) is readily recovered from (3.22) upon setting F to the Stokes drag, $12\pi/\,Re$. However, we also expect (3.22) to be valid for $Re \geq O(1)$. Moreover, (3.22) apparently describes the leading order drift volume induced by an arbitrarily shaped body as long as the far-field flow can be described by a steady Oseenlet. This will be the case as long as the body is towed by a steady external force acting along the direction of translation (i.e., there is a drag force but no lift force acting on the body). In describing the body as a point force, its dimensions are assumed to be small enough compared to the extent of the marked fluid that its exact geometry does not matter.

It follows that many of the details concerning the behavior of D for $Re \ll 1$ discussed in section 3.5 remain pertinent for $Re \geq O(1)$, except that now we must have $Re_h \gg 1$, since (3.22) only applies if $h \gg 1$. The Stokes region existing at $Re \ll 1$ is thus irrelevant; it disappears into the region near the sphere where the Oseenlet does not offer a valid description of the flow. In reality, viscous forces and the vorticity they generate are confined to a thin boundary layer adjacent to the sphere surface, of thickness $1/\sqrt{Re}$, as Re becomes large. The only exception is the viscous wake, into which the vorticity is eventually shed and convected downstream by the bulk flow. Far from the sphere, the velocity disturbance in the wake decays as $1/r$, which we have already found to cause D to diverge logarithmically with τ as $\tau \to \infty$.

It is possible to employ a boundary layer analysis to provide an additional description of the flow in the wake alone [78]. The sphere is again treated as a momentum point source, but streamwise vorticity diffusion is neglected in favor of the much stronger streamwise convection. Again assuming that h is sufficiently large such that $\rho \approx 1$, this approximation to the flow yields

$$\psi_* \sim \frac{F}{2\pi}\left[1 - \exp\left(-\frac{Re_h}{8\tau}\right)\right]. \tag{3.23}$$

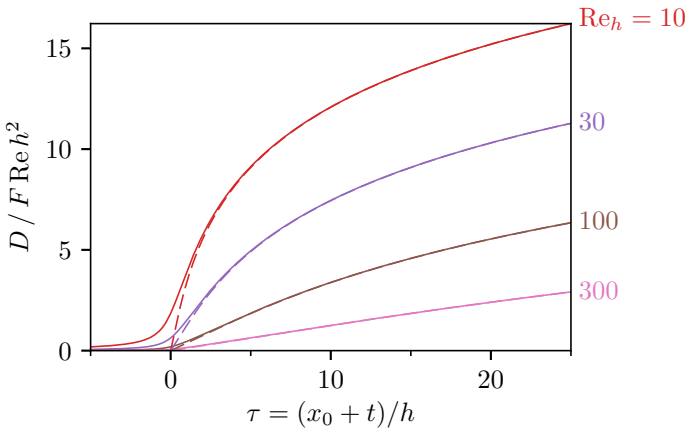

Figure 3.5: The drift volume D, normalized by $F\,Re\,h^2$, for $Re_h \gg 1$ as a function of τ, where we have taken $\tau_0 \to -\infty$. The solid lines indicate the result from (3.22) for the full Oseenlet and the dashed lines correspond to the drift due only to the wake D_w from (3.24).

Putting (3.23) in (3.5), the contribution of the wake to the drift volume is

$$D_w(\tau) = \frac{F\,Re\,h^2}{8}\left[\frac{1-\exp\left(-\,Re_h\,/8\tau\right)}{Re_h\,/8\tau} + E_1\!\left(\frac{Re_h}{8\tau}\right)\right], \tag{3.24}$$

where we have taken $\tau_0 \to 0$ since (3.23) applies only to the downstream far-field flow. Normalizing the results from (3.22) and (3.24) by $F\,Re\,h^2$ collapses them onto single curves for a given a value of Re_h, and such curves are plotted in figure 3.5.

Comparing (3.24) to (3.22), it is readily verified that $D \sim D_w$ for $\tau \gg 1$ (recall that $u \sim 1/2\tau$), reaffirming our earlier statement that the wake dominates the drift whenever $Re_h \gg 1$. Figure 3.5 accordingly reveals good agreement between the full Oseen approximation to D and D_w, even though (3.24) makes no prediction of the drift due to the flow outside of the wake. This is due to the fact that the flow outside the wake is relatively weak, and becomes increasingly so as Re_h increases. Indeed, the agreement between D and D_w improves as Re_h is made larger. Additionally, it is apparent from figure 3.5 that there exists a regime in which D increases linearly with τ given that Re_h is sufficiently large. Specifically, this regime occurs when $1 \ll \tau \ll Re_h\,/8$. Here, the exponential term in (3.23) may be neglected, giving

$\psi_* \sim F/2\pi$. It follows that $D_w \sim Ft$; the drift volume due to the wake increases approximately linearly with time at a rate equal to F. The reason is that the momentum imparted on the fluid by the sphere must equal the total momentum deficit in the wake, independently of the distance downstream. Thus, $F = Q$, where Q is the total flux through any plane traversing the wake normalized by Ua^2 [78]. When $0 < \tau \ll Re_h/8$, the marked fluid fully spans the wake; $w|_{x=0} \ll h$. Therefore, $D(t) \sim D_w(t) \sim \int^t Q\,\mathrm{d}t = Ft$. When $\tau = O(Re_h/8)$, $w|_{x=0} = O(h)$, and the rate at which D increases with t is no longer constant. Once $\tau \gg Re_h/8$, the logarithmic divergence of D with τ is recovered.

However, the reason why $D \not\sim D_w$ when $0 < \tau \leq O(1)$ is not immediately obvious, since the velocity profiles in the wake provided by the Oseenlet and the boundary layer approximation closely coincide [29]. Importantly, the Oseenlet describes the entire far-field flow, rather than just that in the wake. Considering more carefully the flow due to the full Oseenlet, we gather from (3.21) that $\psi_* \sim F/4\pi$ when $|\tau| \ll 1$, and hence $D \sim Ft/2 = D_w/2$. This astonishingly suggests that D increases at the *same* constant rate before *and* after the sphere crosses $x = 0$, despite the asymmetric nature of the flow field at finite Re due to the strong inward flux through the wake. Evidently, the wake does not make the only important contribution to D when $|\tau| \ll 1$. The wake alone increases D at a rate of approximately F when $\tau \leq O(Re_h/8)$. However, conservation of mass dictates that the flux through the wake Q must be compensated by a source flow of equal strength emanating from the sphere [78] (figure 3.3). Since $w|_{x=0} \ll h$ when $\tau \ll 1 \ll Re_h$, only a very small amount of fluid actually resides in the wake in this case. The rest is well outside the wake, where the flow is indeed source-like [100]. After the sphere crosses $x = 0$ ($\tau > 0$), half of the source flow is directed backward toward $x = 0$. Since any fluid crossing backward though the $x = 0$ plane (for

$0 < y < y_* \approx h$) contributes negatively to D, the source flow decreases D at a rate of about $F/2$. It follows that $D \sim D_w - Ft/2 = Ft/2$. Before the sphere crosses $x = 0$ ($\tau < 0$), the half of the source flow that is directed ahead of the sphere (toward $x = 0$) similarly increases D at a rate of about $F/2$. Here, the wake obviously does not contribute to D, and thus it is again found that $D \sim Ft/2$. Thus, despite its faster $1/r^2$ velocity decay, the source-like flow outside of the wake still makes an appreciable contribution to D when $|\tau| \ll 1$. As τ becomes larger, the effect of the source flow fades away, and only the drift induced by the wake remains important.

Yet again, the behavior of $D(\tau; \tau_0, h)$ critically depends on what values that τ and τ_0 are assumed to have. If the length traveled by the sphere is large compared to h such that the sphere passes far beyond the $x = 0$ plane and $\tau \gg 1$, then D is almost entirely accounted for by the forward flux of fluid through the wake. However, if one takes h to be comparable to or smaller than the travel length, such that $\tau \leq O(1)$, both the flux through the wake and the compensating source flow must be considered. Of course, the non-convergent properties of D are nothing new, and are analogous to the similar happenings in inviscid flow and Stokes flow that have already been discussed. However, the (far-field) flow pattern at finite Re is more intricate than the simple fore-aft symmetric flow in these other cases, and the more complicated behavior of D reflects this.

3.7 Discussion

The preceding results for the drift volume are derived assuming that the flow in the co-moving frame is steady everywhere. However, if the sphere is initially started from rest at $t = 0$, consideration must be given to the time it takes for the steady flow to fully develop. If $Re \ll 1$ and we are only concerned

with the flow up to the Oseen distance $r = O(1/\,Re)$, then the transient flow is governed by the unsteady Stokes equations. The dimensionless time scale t_d for the momentum (or vorticity) to diffuse a distance r from the sphere is $t_d \sim Re\, r^2$. Thus, we expect the flow to be quasi-steady for $r \ll \sqrt{t_d/\,Re}$, and steady flow is approached as $t^{-1/2}$ [101]. For the prediction of the drift volume in steady Stokes flow given by (3.16) to apply, the time required for momentum to diffuse far past the marked fluid must be much shorter than the total travel time t of the sphere. At $t = 0$, the distance to the furthest marked fluid element is approximately $\sqrt{x_0^2 + h^2}$. Thus, we have the condition that $t \gg Re(x_0^2 + h^2)$.

As vorticity surpasses the Oseen length, it is transported via convection into the viscous wake (the remainder of the Oseen region remains irrotational). The wake grows diffusively in the transverse direction, but grows convectively (linearly) in the streamwise direction [102]. Therefore, the wake is bounded by an 'edge' at an $O(t)$ distance downstream of the sphere. Similar dynamics apply to laminar wakes at larger Re. Thus, we expect that Equation (3.22) and (3.24) accurately represent $D(t; x_0, h)$ only when the marked fluid is sufficiently far in front of the edge of the wake such that the flow there is approximately steady, i.e., the wake must be well developed.

A second source of unsteadiness occurs due to flow destabilization when Re is increased beyond a critical value. For a rigid sphere, unsteadiness first develops at $Re \approx 210$ [65], inducing a time-dependent drag and lift force on the sphere. Further increases in Re lead to more complex temporal behavior, eventually triggering the transition to turbulent flow [67]. This clearly limits the applicability of the drift volume estimate given by Equation (3.22) and (3.24), which strictly applies only if Re is sufficiently small for the flow to be steady and axisymmetric. However, if the time-averaged drag on the body is nonzero, it follows that there must also be a time-averaged momentum (and

thus mass) deficit in the wake. Moreover, for three-dimensional flows, turbulent wakes eventually transition back to a laminar state at very far distances downstream [78]. This implies that the drift volume will still diverge with time (eventually logarithmically), even in the unsteady case, as long as there is a finite drag on the body.

It is interesting to consider the idealized case of a non-deformable spherical bubble with a perfect-slip surface translating steadily at $Re \gg 1$. Due to the fact that only an $O(1)$ amount of vorticity is generated in the boundary layer adjacent to the bubble, the flow remains steady and laminar, becoming irrotational as $Re \to \infty$ [69]. The leading order drag on the bubble is found to be $F \sim 48\pi/\,Re$ [68]. As $Re \to \infty$, it is reasonable to expect that the inviscid flow result for D given by (3.9) should be recovered. However, as $Re_h \to \infty$ in (3.22), the coefficient in front of the bracketed terms approaches a constant equal to 6π while the bracketed terms themselves vanish. Thus, we find instead that $D \to 0$ as $Re \to \infty$. This (lack of) prediction of D by (3.22) is simply due to its leading order nature. Treating the sphere as a point source of momentum neglects the fact that the body occupies a nonzero volume (V_b). As is shown in section 3.3, D is $O(V_b)$ in inviscid flow.

The divergence of D with t in viscous flows is tied to the existence of regions where the velocity decays slowly, as $1/r$, far from the translating body. Thus, any scenario where this velocity disturbance is weakened can be expected to have an important impact on the drift and drift volume. For example, we have not considered the potentially important effect of external boundaries or neighboring bodies, which generally cause v to decay faster than $1/r$ and hence lead to a bounded drift volume [24, 90, 27]. At finite Re, the presence of boundaries or other bodies in the fluid triggers the process of vorticity annihilation, which cuts off the flux through the wake. This produces irrotational flow far downstream of the translating body [103, 90], and it is thus reason-

able to expect a greatly decreased and bounded drift volume in this case, in contrast to the case of a fully unbounded fluid. There are, of course, other possible situations which cause the velocity to decay more quickly than $1/r$ in the far-field, such as density stratification of the fluid.

Finally, it is important to mention that we have only examined the drift volume in the case that the body is towed steadily through the surrounding fluid by an external force (e.g., sedimenting particles or rising bubbles). If the body is self-propelled and free of acceleration and external forces, i.e., a neutrally buoyant swimmer, there are important differences in the far-field flow pattern that will greatly affect the induced drift volume. Within the Stokes region of a swimmer at $Re \ll 1$, the flow is described by a stresslet ($v \sim 1/r^2$) rather than a Stokeslet ($v \sim 1/r$), and thus the far-field flow disturbance is much weaker compared to a towed body. At distances larger than the Oseen length, the flow disturbance in the wake behind a swimmer is also weaker than that of a towed body, having $v \sim 1/r^2$ and $v \sim 1/r^3$ inside and outside of the parabolic wake, respectively [47]. Moreover, it carries no net momentum (or mass) deficit because the swimmer is force-free ($F = 0$) [18]. Clearly, the drift volume induced by a steady swimmer is essentially different compared to that due to an object translating under an external force.

3.8 Summary

We have conducted a detailed analysis of the drift volume $D(t; x_0, h)$ induced by a spherical body being steadily towed through a viscous fluid, where the flow around the sphere assumed to be steady and axisymmetric in the co-moving frame. For simplicity, we only examined the case where the radius of the sphere is small compared to the extent of the marked fluid ($h \gg 1$). Our analysis was carried out by interpreting D as the time-integrated flux

through a kinematic plane that is stationary in the fixed frame and bounded by a stream tube in the co-moving frame. A two-term asymptotic expansion of D for $h \gg 1$ computed for Stokes flow ($Re = 0$) revealed a positive $O(h)$ correction to D. This contrasts with the analogous result for inviscid flow, where this correction is $O(1/h^3)$ and negative. In addition, a leading order result for D at finite Re is computed, and its behavior as a function of travel time t is shown to parametrically depend on $Re_h = Re\, h$.

A bounded drift volume for $t \to \infty$ and $h \to \infty$ is obtained only for the inviscid case, although the exact value of D depends on the ordering of these limits. Otherwise, the drift volume generally diverges with both t and h as these quantities become large. However, the exact nature of this divergence critically depends upon the assumed ratio of the total distance travelled by the sphere to h, which is encapsulated by τ and τ_0. The fact that evaluating $D(\tau; \tau_0, h \to \infty)$ amounts to evaluating the total momentum of the fluid (divided by ϱ) is responsible for this conditional behavior. Thus, if one wishes to experimentally measure D for a body traveling in an effectively unbounded bulk fluid, the observed behavior may be expected to depend heavily on the values of τ and τ_0.

The drift volume induced by a body translating through a semi-infinite or fully bounded fluid domain at finite Re remains to be considered. The presence of boundaries is expected to have a profound impact on the induced drift volume, as is true for Stokes flow and inviscid flow. Furthermore, the drift volume induced by self-propelled bodies, especially at finite Re, remains an area that is largely unexplored. The lack of a net external force on such swimmers will drastically alter the behavior of $D(t; x_0, h)$ compared to the result for a towed body. Finally, the drift volume due to unsteadily translating bodies appears to be another important area for future investigation. With regard to swimmers, most propel themselves in an unsteady manner. Examining this

case therefore seems critical to understanding the physics of fluid transport by swimmers.

Chapter 4

Drift volume due to swimming bodies

4.1 Introduction

A convenient way of quantifying the net fluid displacement caused by a translating body is via the so-called 'drift volume,' which measures of the amount of fluid entrained by the body as it moves a given distance. Specifically, D is the volume enclosed between the initial and final profiles of a marked (as in with dye) material sheet of fluid that is initially flat and perpendicular to the body's direction of travel. This concept was first introduced by Darwin [22], who considered the drift volume of a body translating an infinite distance through an inviscid fluid. Along with the travel time of the body, the extent of marked fluid is also taken to be infinite. As noted by Darwin and discussed further by Benjamin [94], a subtlety arises concerning the well-posedness of the drift volume having to do with the ordering these infinities. To resolve this issue, it is useful to generalize the drift volume to a finite travel time and a marked plane of a finite size [23, 99, 104]. This is referred to the 'partial drift volume' D_p, which is a well-defined quantity. For brevity, we will refer to the partial drift volume simply as the 'drift volume' in this chapter.

The drift volume depends on the ratio of inertial to viscous forces in

the fluid, which is quantified by the Reynolds number, defined here as $Re = 2\varrho U a/\mu$, where a is the characteristic size of the body, U is its speed, and the fluid density and viscosity are given by ϱ and μ, respectively. In the limit of inviscid flow ($Re \to \infty$), the magnitude of the fluid velocity v at large distances decays rapidly as $1/r^3$, where r is the distance from the body. As a result, the drift volume of the body is of the same order of magnitude as the body's volume [22, 23]. This may be contrasted with Stokes flow ($Re = 0$), where inertial forces are irrelevant, and the dominance of longer-ranged viscous forces lead to a much slower $v \sim 1/r$ velocity decay for a body that is passively towed by an external force. In this case, D diverges linearly with the area of the marked plane ($\sim \pi h^2$) and logarithmically with the travel time t after the body has passed sufficiently far from the initially marked plane [27]. Therefore, D may be orders of magnitude larger than the body volume, becoming infinite as $t \to \infty$. The reason is that the marked fluid elements are displaced a logarithmically divergent distance, as can be shown by integrating the $v \sim 1/r$ far-field velocity disturbance. If Re is finite, the presence of fluid inertia causes the majority of the flow at sufficiently large distances from the body to appear source-like and decay more quickly as $v \sim 1/r^2$. As a result, D is decreased compared to the $Re = 0$ case. However, this source-like flow is supplied by a viscous wake through which there is a net fluid flux. The wake flux remains constant at all distances into the wake, being proportional to the rate at which the body imparts momentum onto the fluid (via the drag force). As a result, D is still potentially much larger than the body volume, especially in the case that Re is small to intermediate [104].

Quantifying the amount of fluid volume that is transported by a self-propelled body is relevant to estimating the extent to which biogenic mixing is achieved by swimming organisms, especially small ones. The idea that swimmers might contribute to large-scale mixing processes, especially in the world's

oceans, originates with Munk [86]. Support to this idea, on an energetic basis, is given by Dewar et al. [16]. A critical issue with this hypothesis concerns the mixing efficiency of these organisms. The majority of the biomass of oceanic swimmers comprises millimeter-scale zooplankton, such as copepods and krill. If it is assumed that these organisms transport no more fluid than they physically displace, then the mixing efficiency achieved is very low, suggesting little contribution to ocean stirring [105]. Large organisms have a higher mixing efficiency, but their low abundance suggests that they make little contribution to mixing. However, as argued by Katija and Dabiri [17], the drift volume (relative to the body volume) increases drastically as Re is decreased, providing a potentially important, 'viscosity-enhanced', mechanism for swimmers to induce large-scale flows that can lead to large-scale fluid mixing.

An issue with this viscosity-enhanced drift volume argument is that the velocity field produced by a swimmer is fundamentally different than that produced by a towed body (e.g., a sedimenting particle). For a steadily translating neutrally buoyant swimmer (that is otherwise free of external forces) at $Re = 0$, there is no 'Stokeslet' contribution to the flow, which is responsible for the slow $1/r$ velocity decay. Instead, the far-field velocity of the swimmer is dominated by the 'stresslet' (or symmetric force dipole) component of the flow that is associated with the equal and opposite thrust and drag forces acting on the swimmer. The flow disturbance due to a force dipole has a more rapid $v \sim 1/r^2$ decay, and thus fluid elements are displaced a finite distance, placing a limitation on the drift volume induced by a swimmer [18]. Moreover, if one considers a swimmer that passes from far behind to far ahead of a passive tracer particle in the fluid, the tracer moves in a nearly closed loop due to the fore-aft mirror-image symmetry of the Stresslet velocity field (unless the tracer is very near to the direct path of the swimmer) [20, 28]. In this case, the swimmer induces $D \sim O(V_b)$, where V_b is the swimmer's volume [19, 28],

as is obtained for a body in potential flow.

This seems to directly suggest that the drift volume due to a Stokesian swimmer does not lead to the displacement of fluid volumes greater than $O(V_b)$, and thus small swimmers should be ineffective mixers. However, simulations conducted by Lin, Thiffeault, and Childress [20] have demonstrated that the effective diffusivity of a passive tracer particle is significantly enhanced in a dilute suspension of swimmers that have a far-field stresslet flow over a similar suspension of 'potential flow' swimmers. Experiments show a similar effect [106, 107, 108]. The reason is that swimmers need not follow an infinitely long or straight-line path, leading to symmetry breaking of the tracer path [109].

The drift volume induced by a swimmer in Stokes flow is addressed by Leshansky and Pismen [19] and Pushkin, Shum, and Yeomans [28]. These authors consider the case where the swimmer passes symmetrically from far behind to far ahead of the initially marked plane. However, the largest contribution to the (partial) drift volume arises when the path traveled by the swimmer is asymmetric, which is the case we focus on here. We adopt a simple description of a swimmer as a translating symmetric force dipole. Thus, the near-field flows that depend on the specific geometric details and swimming kinematics of a swimmer are ignored in favor of the more universal far-field flow expected of most typical swimmers. We show that the drift volume of a swimmer at $Re = 0$ is maximized when the swimmer starts or ends its swimming path close to its nearest approach to the marked plane. In fact, D diverges with h in this case, although it is convergent with respect to the travel time t, in contrast to a towed body.

The second scenario that we focus on is the drift volume due to a steady swimmer at finite Re, of which there are currently no detailed analysis. Our motivation is that zooplankton communities throughout the oceans are often dominated by intermediate-Re swimmers such as copepods and krill [11,

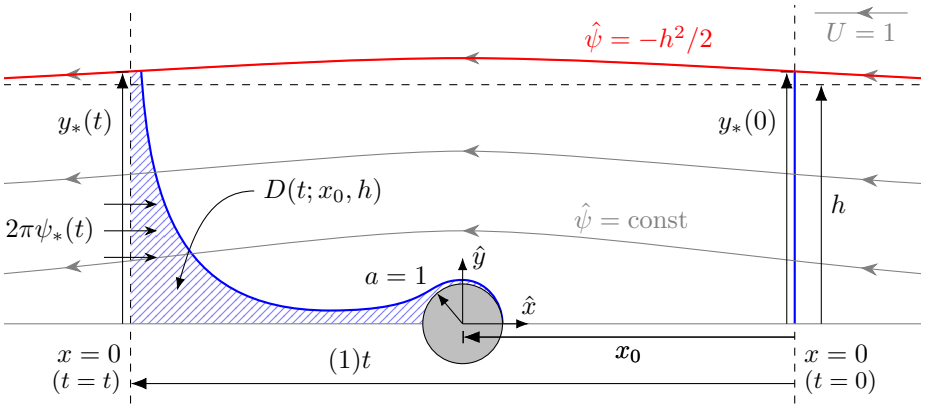

Figure 4.1: An illustration of the drift volume D in the co-moving frame, where a uniform flow approaches the swimmer's body (depicted as a sphere for simplicity) at unit velocity. At $t = 0$, the fluid is marked at $x = 0$ for $y < y_*(0)$, as indicated by the solid line to the right of the swimmer. The swimmer is at an initial distance x_0 from the $x = 0$ plane. At time $t > 0$, the swimmer translates a distance of $(1)t$ toward and eventually past $x = 0$, causing the marked fluid to deform. The volume swept out by the marked fluid at time t is indicated by the shaded area to the left of the swimmer and is defined to be the drift volume, $D(t; x_0, h)$. The rate at which D increases with t is equal to the volumetric flux, $2\pi\psi_*(t)$, through $x = 0$ for $y < y_*(t)$. Note that, in general, the marked fluid need not be to the right of $x = 0$ at time t, and fluid to the left of $x = 0$ is counted as a negative contribution to D.

12], which have $Re = O(0.1)$ to $O(100)$ [110]. Thus, the fluid transport induced by such organisms is of interest. We describe the finite-Re swimmer as a steadily translating Oseen force dipole. The drift volume induced by this model swimmer is predicted to be $O(b/Re)$ for $Re \ll 1$, where b is the force dipole strength. It is shown that the drift volume diminishes rapidly as Re increases, suggesting that the amount of fluid transport (and hence fluid mixing) induced by a steady intermediate-Re swimmer is limited.

4.2 Calculation of the drift volume

Consider a solitary swimmer of characteristic length a translating steadily through an unbounded, incompressible Newtonian fluid of viscosity μ and

density ϱ at speed U. We will normalize length by a, time t by a/U, and force by μaU (a viscous scaling). All quantities hereafter will be dimensionless unless otherwise stated. We will utilize both the frame of reference that is fixed with respect to the bulk fluid far from the swimmer and the reference frame that is co-moving with the swimmer. Thus, let $\boldsymbol{r} = x\boldsymbol{e}_x + y\boldsymbol{e}_y$ and $\hat{\boldsymbol{r}} = \hat{x}\boldsymbol{e}_x + \hat{y}\boldsymbol{e}_y$ define the position vectors in these two frames, respectively. Here, $\boldsymbol{e}_x$ and $\boldsymbol{e}_y$ are the axial and radial unit vectors of a cylindrical coordinate system, respectively, where the swimmer translates in the $\boldsymbol{e}_x$ direction. The co-moving coordinates are related to their fixed-frame analogs as $\hat{x}(x,t) = x - (x_0 + t)$ and $\hat{y}(y,t) = y$, where x_0 is the x position of the swimmer at time $t = 0$.

We assume that the swimmer generates a flow that is axisymmetric about the x axis, free of azimuthal rotation, and steady in the co-moving frame. Therefore, the flow in the co-moving frame may be described in terms of the stream function

$$\hat{\psi}(\hat{x},\hat{y}) = \int \hat{y}\hat{\boldsymbol{u}} \cdot (\boldsymbol{e}_x \,\mathrm{d}\hat{y} - \boldsymbol{e}_y \,\mathrm{d}\hat{x}) \,, \tag{4.1}$$

which has been normalized by Ua^2 and where $\hat{\boldsymbol{u}} = \hat{u}_x\boldsymbol{e}_x + \hat{u}_y\boldsymbol{e}_y$ is the (co-moving) fluid velocity vector. By satisfying (4.1), $\hat{\boldsymbol{u}}$ automatically satisfies continuity ($\nabla\cdot\hat{\boldsymbol{u}} = 0$). In order to uniquely determine $\hat{\psi}$, we set $\hat{\psi}(\hat{x}(x,t),0) = 0$. Similarly, an instantaneous stream function ψ giving the fixed-frame velocity $\boldsymbol{u} = u_x\boldsymbol{e}_x + u_y\boldsymbol{e}_y$ may be defined by subtracting the bulk uniform flow in the co-moving frame, which has unit velocity in the $-\boldsymbol{e}_x$ direction, from $\hat{\psi}$, giving $\psi(x,y,t) = \hat{\psi}(\hat{x}(t),\hat{y}) + \hat{y}^2/2$.

Now, consider a material sheet of fluid that is marked (as in with dye) at $t = 0$ on the $x = 0$ plane and whose outer edge is initially on the intersection of the $x = 0$ plane with the co-moving streamline $\hat{\psi} = -h^2/2$ (figure 4.1). At $t = 0$, the swimmer is at position $\boldsymbol{r} = x_0\boldsymbol{e}_x$ relative to the center of the initially marked fluid, which forms a flat circular disc perpendicular to the swimmer's

path of travel. The radius of this disc approaches h as $x_0 \to -\infty$. The marked material surface deforms as time progresses due to the flow generated by the swimmer. From this, the (partial) drift volume D induced by the swimmer may be defined as the volume of fluid bounded by the $x = 0$ plane, the marked material sheet, and the streamline approaching $y = h$ as $x \to \pm\infty$ [104, 23, 22] (figure 4.1). The stream function ψ (times a factor of 2π) can be interpreted as the instantaneous volumetric flux through a surface of revolution about the x axis formed by an arbitrary path connecting any two points on the xy plane. Let $y_*(t)\boldsymbol{e}_y$ be the point (in the fixed frame) where the streamline bounding the marked fluid intersects the $x = 0$ plane, and let $\psi_*(t) = \psi(0, y_*, t)$. Then, the drift volume, normalized by a^3, is given by [104]

$$D(t; x_0, h) = \int_0^t \psi_*(t'; x_0, h)\,\mathrm{d}t' - [V_b(t) - V_b(0)], \tag{4.2}$$

where $V_b(t)$ is the volume of the swimmer that has passed through the $x = 0$ plane at time t. The V_b contribution to D is the simple result of the swimmer's body physically displacing fluid, as it passes through $x = 0$, into the geometric fluid volume that defines D. Note that this method for obtaining D conveniently circumvents the need to explicitly compute the paths of the marked fluid elements.

We are primarily interested in the possibility of the swimmer transporting a volume of fluid that is large compared to its own volume via drift. Thus, we limit our attention to the $h \gg 1$ scenario, where the extent of the marked fluid is much larger than that of the swimmer, so that we may quantify such large-scale fluid motion. Let $\tau = (x_0 + t)/h$ and $\rho(\tau) = y_*(t)/h$. Far from the swimmer, for $\hat{r} = |\hat{\boldsymbol{r}}| \gg 1$, the deviation of the streamline $\hat{\psi} = -h^2/2$ (that intersects the edge of the marked fluid) from its free-stream position $\hat{y} = h$ becomes asymptotically small. Implicitly relating $\rho(t)$ and $\psi_*(t)$ as

$$\rho^2 = 1 + \frac{2\psi_*}{h^2} \tag{4.3}$$

makes this clear. Thus, $\rho(\tau) \sim 1$ for $h \gg 1$, and we will take advantage of this fact in order to compute asymptotic approximations to D. Rewriting (4.2) in terms of the rescaled variables τ and ρ_* gives

$$D(\tau_f, \tau_i, h) = 2\pi h \int_{\tau_i}^{\tau_f} \psi_*(\tau, \rho(\tau); h)\, \mathrm{d}\tau - [V_b(\tau_f) - V_b(\tau_i)], \tag{4.4}$$

where τ_i and τ_f are the initial and final values of τ.

4.3 A Stokesian swimmer

First, we address the drift volume due to a swimmer in Stokes flow ($Re = 0$). We will consider a steadily translating 'dipolar' swimmer, whose effect is to exert a symmetric force dipole, or 'stresslet,' on the fluid. Due to our assumption that the swimmer moves along a straight path, there is no antisymmetric 'rotlet' component to flow. We assume that the swimmer is neutrally buoyant and otherwise free of external forces so that there is also no Stokeslet (point-force) component to the flow. Note that this is a far-field model only; it does not consider the specifics of the swimmer's exact geometry and swimming kinematics. However, doing so is not necessary for quantifying the large-scale fluid transport due to an individual swimmer. If the detailed flow around the swimmer is expressed in a multipole expansion, the leading-order stresslet term has $\hat{u} = |\hat{\boldsymbol{u}}| \sim 1/\hat{r}^2$ and dominates the far-field flow. The 'quadrupolar' terms at the next order have $\hat{u} \sim 1/\hat{r}^3$, and they are thus mainly important in describing the near-field flow (along with even higher order terms). It has been shown that these quadrupolar terms only make an $O(1)$ contribution to D [28, 19]. Therefore, they are irrelevant to the possibility of an individual swimmer transporting a volume of fluid that is larger than that of the swimmer's body, justifying our neglect of the near-field flow details.

Concerning our assumption of steady swimming kinematics, most mi-

croorganisms propel themselves in an unsteady manner, inducing a time dependent flow that is oscillatory over a stroke cycle. However, because we are concerned with large-scale transport of fluid, it is appropriate to assume that the total distance traveled by the swimmer is large compared to that traveled over a single stroke cycle. In this case, a steady swimming model is sufficient to accurately describe the time-averaged far-field flow [111, 112].

It will prove useful to express the flow due to the swimmer in terms of that generated by a point force, i.e., a 'Stokeslet', in the $\boldsymbol{e}_x$ direction. The Stokeslet velocity field can be expressed as $\hat{\boldsymbol{u}}_S = \boldsymbol{e}_x \cdot \boldsymbol{J}$, where $\boldsymbol{J} = \boldsymbol{I}/\hat{r} + \hat{\boldsymbol{r}}\hat{\boldsymbol{r}}/\hat{r}^3$ is the Oseen tensor and $\boldsymbol{I}$ is the identity tensor. Let $\hat{\psi}_S$ be the stream function obtained by integrating $\hat{\boldsymbol{u}}_S$ according to (4.1), yielding

$$\hat{\psi}_S(\hat{x}, \hat{y}) = \frac{\hat{y}^2}{8\pi\hat{r}}. \tag{4.5}$$

The steady, axisymmetric flow generated by the swimmer may be expressed in terms of $\hat{\psi}_S$ as

$$\hat{\psi}(\hat{x}, \hat{y}) = -\frac{1}{2}\hat{y}^2 - b\frac{\partial \hat{\psi}_S}{\partial \hat{x}}, \tag{4.6}$$

where the first term accounts for the uniform bulk flow and the second term represents the flow due to a symmetric force dipole (stresslet) of strength b.

Swimmers producing the flow field given by (4.6) may be divided into two categories: $b < 0$ gives a 'puller', whose center of thrust is in front of its center of drag, and $b > 0$ gives a 'pusher', whose center of thrust is behind its center of drag (figure 4.2). Microorganisms such as the bacteria *E. coli*, which use flagella to push themselves through their surrounding fluid, exemplify pusher-type swimmers. On the other hand, an example of a puller is given by *Chlamydomonas*, which possesses two flagella that perform a 'breast stroke,' pulling the organism along. Due to the symmetry of the force-dipole, the centers of thrust and drag on the swimmer lie on, and are aligned with, the x axis.

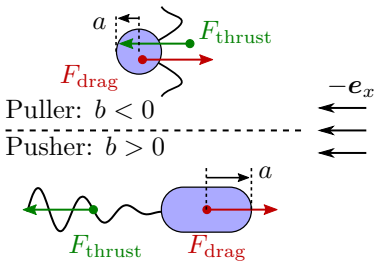

Figure 4.2: An illustration puller and pusher type swimmers translating at unit velocity, such that the oncoming flow (in the co-moving frame) is in the $-\boldsymbol{e}_x$ direction. Pullers ($b < 0$) are propelled from the front, and hence the center of thrust is in front of the center of drag. Pushers ($b > 0$) are propelled from the rear, where the opposite is true. Note that F_{thrust} and F_{drag}, which are equal and opposite, represent the force exerted by the swimmer on the fluid, and hence F_{thrust} is shown to be directed opposite to the swimming direction.

From (4.6), the instantaneous fixed-frame stream function representing the stresslet generated by the swimmer, evaluated at $x = 0$ and $y = y_*(t)$, may be expressed as

$$\psi_*(\tau) = -b\frac{\partial\hat{\psi}_S}{\partial\hat{z}}\bigg|_{\substack{\hat{x}=-h\tau \\ \hat{y}=h\rho(\tau)}} \sim \frac{b}{h}\frac{\mathrm{d}}{\mathrm{d}\tau}\hat{\psi}_S(-h\tau, h) = \frac{b}{h}\frac{\mathrm{d}}{\mathrm{d}\tau}\psi_{hS}(\tau), \tag{4.7}$$

where we invoked the fact that $\rho(\tau) \sim 1$ for $h \gg 1$. Here, $\psi_{hS}(\tau)$ is the instantaneous fixed-frame stream function of a Stokeslet centered at the swimmer's location and evaluated at $\boldsymbol{r} = 0\boldsymbol{e}_x + h\boldsymbol{e}_y$, which, from (4.5), is

$$\psi_{hS}(\tau) = \frac{h}{8\pi\sqrt{\tau^2+1}}. \tag{4.8}$$

Thus, from (4.7) in (4.4), we see that we may obtain a leading-order asymptotic approximation to $D(\tau; h)$ for $h \gg 1$ for a dipolar swimmer using the particularly simple formula

$$D \sim 2\pi h\int_{\tau_i}^{\tau_f}\frac{b}{h}\frac{\mathrm{d}}{\mathrm{d}\tau}\psi_{hS}(\tau)\,\mathrm{d}\tau = 2\pi b\Big(\psi_{hS}(\tau_f) - \psi_{hS}(\tau_i)\Big). \tag{4.9}$$

By inserting (4.8) into (4.9), we obtain

$$D = \frac{bh}{4}\left(\frac{1}{\sqrt{\tau_f^2+1}} - \frac{1}{\sqrt{\tau_i^2+1}}\right) + O(1) \tag{4.10}$$

as the leading-order drift volume induced by a dipolar swimmer at $Re = 0$. The $O(1)$ term represents error from two sources. The first is the $[V_b(\tau_f) - V_b(\tau_i)]$ term from (4.4), which comes from the physical displacement of fluid to the right of the $x = 0$ plane by the swimmer's body. The second comes from the quadrupolar (and higher order) flows generated by the swimmer that we have neglected. Neither of these factors are important to large scale fluid transport. There is some additional error due to setting $\rho = 1$, but it can be shown that this is only $O(1/h)$.

Turning our attention to the first term in (4.10), which represents the contribution of the stresslet to D, we see that $D \sim O(bh)$, and thus the drift volume is potentially large. However, there is an important limitation on the drift volume induced by a dipolar swimmer; the path traveled must not be symmetric with respect to the position of the initially marked plane at $x = 0$. If it is, i.e., if $\tau_f = -\tau_i$, (4.10) makes apparent that the stresslet makes no net contribution to D, and hence $D = O(1)$. Furthermore, D is also $O(1)$ if the swimmer moves from sufficiently far behind to sufficiently far in front of the $x = 0$ plane, corresponding to the limits $\tau_f \to \infty$ and $\tau_i \to -\infty$. In these cases, the swimmer only transports a net volume of fluid that is comparable to its own body volume. This may be attributed to the fore-aft mirror-image symmetry of the stresslet flow. A given fluid element undergoes significant displacement as the swimmer makes its closest approach to it, but it is then returned to its original position as the swimmer continues onward [28]; the fluid element essentially traverses a closed-loop path.

From this, it is reasonable to conclude that large scale transport of fluid by a Stokesian swimmer is not possible because the stresslet flow, which produces the strongest far-field fluid motion, produces little *net* displacement of fluid elements. Interestingly, and in contradiction to this notion, computations performed by Lin, Thiffeault, and Childress [20] have demonstrated that

a dilute suspension of stresslet swimmers significantly enhance the effective diffusivity of passive tracer particles in comparison to an analogous suspension of quadrupolar (potential dipole) swimmers (which lack a stresslet). Clearly, stresslet-producing swimmers must generate greater fluid displacement than their quadrupolar counterparts for this to be possible. The key reason is that swimmers generally travel a finite distance before stopping or changing direction (e.g., the run-and-tumble motion of *E. coli*), and hence need not travel in a symmetric path relative to all fluid elements. In this case, the stresslet flow may induce a large, $O(hb)$, drift volume.

Indeed, we see from (4.10) that D is maximized when the path traveled by the swimmer is maximally asymmetric with respect to the marked plane. This refers to the scenario where the swimmer starts much nearer to the $x = 0$ plane where the fluid is initially marked ($\tau_i \ll 1$) than where it eventually stops or changes direction ($\tau_f \gg 1$). Letting $\tau_i \to 0$ and $\tau_f \gg 1$ in (4.10) yields $D_{\max} \sim bh/4 \gg 1$. The same result is obtained if $-\tau_i \gg 1$ and $\tau_f \ll 1$, corresponding to the opposite case where the swimmer starts far away but stops (or turns) near $x = 0$.

Experimental measurements [112] and numerical predictions [113] of the flow produced by *E. coli* allow us to estimate $D_{\max}$ for this swimmer. In particular, $F_d \approx 1\,\mathrm{pN}$, $l_d \approx a \approx 2\,\mu\mathrm{m}$, and $U \approx 20\,\mu\mathrm{m/s}$, where F_d and l_d are the magnitude and separation distance of the centers of thrust and drag, respectively. Assuming the viscosity of water ($\mu \approx 10^{-3}\,\mathrm{Pa\,s}$) gives a (dimensionless) dipole strength of $b = F_d l_d/\mu U a \approx 25$. Hence, we obtain $D_{\max} \approx 6.25h$, which is clearly many times the physical volume of an *E. Coli* bacterium for $h \gg 1$.

At this point, it is possible to raise the objection that D and $D_{\max}$ are ill-defined; they do not converge to a specific value (for a given swimmer) as h is made large. Letting $h \to \infty$ seems to suggest that the swimmer transports

an infinite volume of fluid from wherever it starts it's motion. In fact, this is similar to the case of a towed body for which D also diverges as $h \to \infty$ [104]. This behavior is due to our assumption of an unbounded fluid housing a single swimmer. In reality, the swimmers will be surrounded by physical boundaries and other passive or actively moving objects in the flow, which will eventually cut off the drift due to the individual swimmer [90]. As we will see in section 4.4, the presence of any amount of fluid inertia will also cause D to be bounded as $h \to \infty$. The key point is that the drift volume due to a Stokesian swimmer may be large compared to the volume of the swimmer itself, enabling large scale fluid transport by a microswimmer.

4.4 Finite Reynolds number swimmers

The drift volume due to a swimmer moving at a finite Re may be computed by utilizing Oseen's approximation to the flow [see, e.g., 78, p. 241]. The Oseen equations yield a uniformly valid solution to the flow for $Re \ll 1$, and we first focus on this case. We again make the assumption that the swimmer exerts a symmetric force dipole of strength b along the $\boldsymbol{e}_x$ direction. Proceeding similarly to the Stokes flow case, we may write the flow due to the dipolar swimmer in terms of the point-force solution to the Oseen equations, $\hat{\psi}_O(\hat{x}, \hat{y}; Re)$. This is possible because, akin to the Stokes equations, the Oseen equations are linear in $\hat{\psi}$. The flow induced by the dipolar swimmer is given by

$$\hat{\psi}(\hat{x}, \hat{y}) = -\frac{1}{2}\hat{y}^2 - b\frac{\partial \hat{\psi}_O}{\partial \hat{x}}, \tag{4.11}$$

where b is the effective force dipole strength and

$$\hat{\psi}_O(\hat{x}, \hat{y}) = \frac{1}{2\pi\, Re}\left(1 - \frac{\hat{x}}{\hat{r}}\right)\left\{1 - \exp\left[-\frac{Re}{4}(\hat{r} + \hat{x})\right]\right\} \tag{4.12}$$

is the flow due to a translating 'Oseenlet' (point force). Note that we use the term 'effective' here because b will not, in general, be equal to the *actual* force dipole exerted by the swimmer on the fluid [18]; the force dipole is not conserved across arbitrary fluid surfaces enclosing the swimmer. However, for $Re \ll 1$, the two quantities are of the same order of magnitude [47]. (4.11) is analogous to (4.6), with $\hat{\psi}_S$ replaced with $\hat{\psi}_O$. To obtain the drift volume, we may simply replace ψ_{hS} with ψ_{hO} in (4.9) to give the leading-order approximation

$$D \sim 2\pi b\Big(\psi_{hO}(\tau_f) - \psi_{hO}(\tau_i)\Big), \tag{4.13}$$

for $h \gg 1$, where $\psi_{hO} = \hat{\psi}_O(-h\tau, h)$. This yields, from (4.12) in (4.13),

$$D \sim \frac{b}{Re}\left[\left(\frac{\tau}{\sqrt{\tau^2+1}}+1\right)\left\{1-\exp\left[-\frac{Re_h}{4}\left(-\tau+\sqrt{\tau^2+1}\right)\right]\right\}\right]_{\tau_i}^{\tau_f}, \tag{4.14}$$

where $Re_h = Re\, h$ is the Reynolds number based on the radius of the initially marked fluid disc.

The value of Re_h quantifies how strongly fluid inertia affects the motion of the marked fluid elements. Thus, it also quantifies the strength of the effect of inertia on D. Indeed, Re_h may be interpreted as the ratio of the height of the marked plane h to the 'Oseen length', $1/Re$, at which inertia becomes appreciable [104]. The flow pattern generated by the swimmer at $Re \ll 1$ is illustrated in figure 4.3. The impact of inertia on the flow is significant at distances of $\hat{r} \geq O(1/Re)$ from the swimmer, in the 'Oseen region,' whereas this effect is small for $\hat{r} \ll 1/Re$, in the 'Stokes region,' where the flow approaches that of a stresslet.

Figure 4.4 plots the drift volume for a dipolar swimmer as a function of Re_h. In order to obtain a universal curve for each value of Re_h, we plot D/bh, letting $\tau_i \to -\infty$ and $\tau = \tau_f$ on the horizontal axis. As detailed in the caption of figure 4.4, it is straightforward to obtain values of D/bh for arbitrary τ_f and τ_i by taking the difference of the corresponding values of D/bh on any given

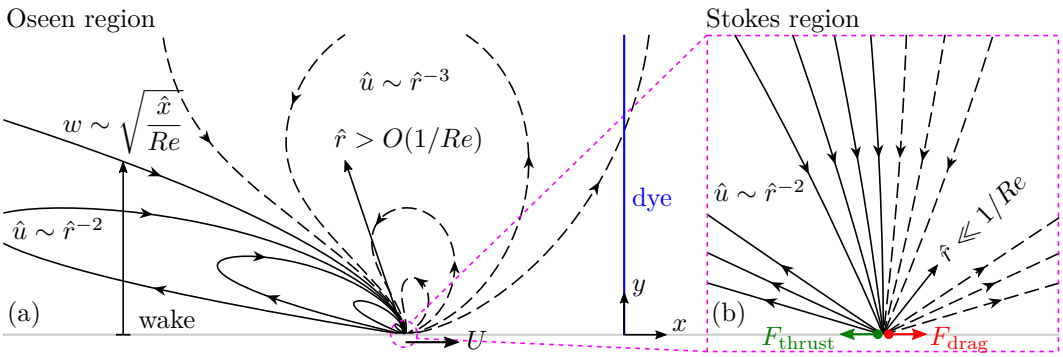

Figure 4.3: The streamlines, in the fixed frame, generated by a pusher-type ($b > 0$), dipolar swimmer translating at constant speed ($U = 1$) at $Re \ll 1$. Here, $\hat{r}$ is the radial distance from the swimmer and $\hat{u}$ is the magnitude of the velocity disturbance. Dashed lines indicate positive isocontours of $\hat{\psi}$, while solid lines indicate negative isocontours, and the arrows indicate the flow direction. The flow pattern at distances $\hat{r} > O(1/Re)$ from the swimmer, in the Oseen region, is affected appreciably by inertia (a). For illustrative purposes, the initial position of the dyed sheet of fluid is shown to the right of the swimmer. A viscous wake of height w grows parabolically with distance downstream of the swimmer. At distances $\hat{r} \ll 1/Re$, in the Stokes region, inertial effects are relatively weak and the flow pattern approaches the $Re = 0$ stresslet (b). Equivalent plots for a puller ($b < 0$) may be visualized from the above illustration by simply negating the flow directions and the sign of ψ (but not the swimming direction). In this case, the 'positions' of F_{thrust} and F_{drag} are swapped as illustrated by figure 4.2.

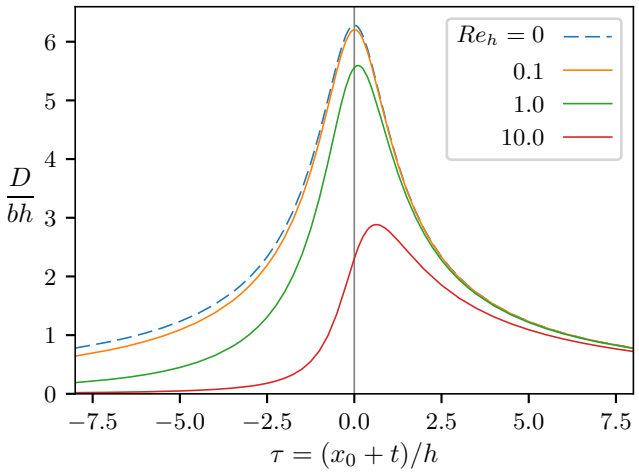

Figure 4.4: The (partial) drift volume D, normalized bh, versus dimensionless time τ, as given by (4.14), where we have taken $\tau_i \to -\infty$ and let $\tau = \tau_f$. The dashed line represents $Re_h = 0$, while the solid lines represent $Re_h = \{0.1, 1, 10\}$ as the curves descend, respectively. For arbitrary values of τ_f and τ_i, one may obtain D/bh by picking τ_f and τ_i off of the τ axis and subtracting the respective corresponding values of D/bh.

curve. At $Re_h = 0$, corresponding to a Stokesian swimmer, D/bh is completely symmetric about τ. Thus, there is no net drift volume for a symmetric path where $\tau_f = -\tau_i$, which is an affect of the fore-aft flow symmetry.

As Re_h increases, two major effects are observed. First, the overall value of D/bh decreases, meaning that fluid inertia causes an overall decrease in the drift volume. This is also apparent from (4.14), where the outermost bracketed term is at most $O(1)$, and hence $D \sim O(b/Re)$. This is readily explained by the fact that inertial forces act to cause the magnitude of the fluid velocity $\hat{u} = |\hat{\boldsymbol{u}}|$ to decay more rapidly with $\hat{r}$. The stresslet-like flow in the Stokes region decays as $\hat{u} \sim \hat{r}^{-2}$, whereas the majority of the flow in the Oseen region decays as $\hat{u} \sim 1/\hat{r}^{-3}$ (figure 4.3). As Re increases, the distance from the swimmer at which the Stokes region ends and the Oseen regions begins shrinks (as $1/Re$), and the slower fluid velocities in the Oseen region cause less overall fluid displacement. However, D is still potentially large *as long as* Re *is small*. The second major effect of inertia is that it causes D/bh to become asymmetric about $\tau = 0$ due to breaking of the fore-aft flow symmetry. Thus, in contrast to Stokes flow, the drift volume induced by a dipolar swimmer moving along a symmetric path ($\tau_f = -\tau_i$) no longer vanishes, especially if Re_h is large. The drift occurring for $\tau < 0$, before the swimmer has crossed the $x = 0$ plane, is markedly less than that occurring for $\tau > 0$, after $x = 0$ has been crossed.

In contrast to Stokes flow, (4.14) interestingly reveals that D does not diverge with h when Re is finite. If we assume that τ_f and τ_i remain finite, taking the limit $h \to \infty$ in (4.14) amounts to letting $Re_h \to \infty$, such that the marked plane is large compared to the Oseen length. The result is

$$\lim_{Re_h \to \infty} D = \frac{b}{Re} \left[\frac{\tau}{\sqrt{\tau^2 + 1}} \right]_{\tau_i}^{\tau_f}. \tag{4.15}$$

The drift volume given by (4.15) is maximized when $\tau_f \to \infty$ and $\tau_i \to -\infty$,

giving $D = 2b/Re$. (4.15) is of the same form (up to a constant) as the drift volume due to a body in inviscid flow [104], which reflects the fact that we have taken the Reynolds number on the scale of the marked fluid (Re_h) to be infinite. The far-field flow due to the swimmer approaches that of a potential dipole for $\hat{r} \gg 1/Re$, which is the same flow pattern that is generated by a sphere translating through an inviscid fluid. The only region where the flow does not eventually approach the potential dipole form as $\hat{r}$ becomes large is in a parabolic wake behind the swimmer (figure 4.3). For a towed body, this wake is important to the generating drift due to the mass deficit that it caries [104], which is due to the presence of a net force on the towed body. Due to the force-free nature of the swimmer, however, there the wake carries no net mass deficit. Thus, if the marked fluid spans the entire wake, the wake makes no net contribution to D. However, fluid is exchanged in the wake itself, and this topic is discussed in section 4.5.

If an intermediate-Re swimmer ($Re \geq O(1)$) is considered, the flow sufficiently far from the swimmer is still described by the Oseen flow (4.11) because the perturbation to the uniform stream remains small [29]. In fact, the perturbation from the free stream far from the swimmer generally becomes smaller as Re increases. We assume that Re is not so large as to induce turbulence, so that a laminar description of the flow is adequate. Of course, the Oseen description does not capture the near-field flows that are significantly perturbed by the swimmer's geometry, but these flows are generally unimportant to the generation of a large scale drift due to their short-ranged nature. Therefore, Equation (4.14) and (4.15) suggest that, at most, $D \sim O(b/Re)$ for a finite Re swimmer. This implies that a potentially large drift volume can be induced by a swimmer at $Re \ll 1$, but not by a swimmer having $Re \geq O(1)$, suggesting that the capability of such a swimmer to individually transport large fluid volumes is severely limited.

4.5 Fluid transport in the wake

There is one potential caveat to our conclusion that an individual intermediate-Re swimmer is generally incapable of generating large scale fluid transport. This concerns the extent to which fluid is exchanged in the wake. Inertia has the effect of breaking the far-field flow into two distinct regions (figure 4.3). The majority of the flow assumes a potential dipole character, having $\hat{u} \sim 1/\hat{r}^3$; viscous forces are mostly irrelevant here, and the drift volume induced by this flow is accounted for by (4.15). However, viscous forces do remain relevant within the wake region, as evidenced by the slower $1/\hat{r}^2$ velocity decay. This is the same rate of velocity decay that is found for Stokesian swimmers that, as shown in section 4.3, can transport fluid volumes on a large scale. For a towed body, the wake makes a substantial contribution to the drift volume because it contains a net mass deficit that is constant with the longitudinal distance into the wake. Hence, the wake causes a linear divergence of D with time if the entire flux through the wake is counted [18, 104]. However, due to the force-free nature of a neutrally buoyant swimmer, there is zero net mass deficit in the wake, and hence the total drift volume due to the wake is also zero. However, the bidirectional flow pattern in the wake, shown in figure 4.3, seems to suggest that the wake still causes fluid exchange, which may be significant. It is thus of interest to quantify the total exchange of fluid volume in the wake.

The asymptotic form of the flow in the wake of due to a translating Oseenlet (point force) for $\hat{y} \ll \hat{x}$ is

$$\hat{\psi}_{Ow}(\hat{x}, \hat{y}) = \frac{1}{\pi\, Re}\left(1 - \exp\left[\frac{Re\,\hat{y}^2}{8\hat{x}}\right]\right), \tag{4.16}$$

which can be obtained from (4.12). This is also the flow obtained upon conducting a boundary layer analysis of the wake behind a towed body [78, p. 349]. Inserting $\hat{\psi}_{Ow}$ in place of $\hat{\psi}_O$ in (4.11) then yields for the stream function of

the wake behind a dipolar swimmer

$$\hat{\psi}_w(\hat{x},\hat{y}) = -\frac{b\hat{y}^2}{8\pi\hat{x}^2}\exp\left(\frac{Re\,\hat{y}^2}{8\hat{x}}\right). \tag{4.17}$$

The descriptions of the flow given by Equation (4.16) and (4.17) apply at distances sufficiently far downstream of the swimmer such that the streamlines are approximately straight and parallel.

From (4.17), the x-direction velocity in the wake is

$$\hat{u}_x = \frac{1}{\hat{y}}\frac{\partial\hat{\psi}_w}{\partial\hat{y}} = -\frac{b(Re\,\hat{y}^2+8\hat{x})}{\hat{x}^3}\exp\left(\frac{Re\,\hat{y}^2}{8\hat{x}}\right). \tag{4.18}$$

Assuming a pusher ($b>0$), it is apparent from (4.18) that $\hat{u}_x<0$ when $\hat{y}^2<-8\hat{x}/Re$ and $\hat{u}_x>0$ when $\hat{y}^2>-8\hat{x}/Re$. Therefore, the wake contributes a time-integrated flux of fluid in the direction opposite to the swimming direction that is given by

$$D_- = 2\pi bh\int_{\tau_i}^{\tau_f}\psi_{w0}\,\mathrm{d}\tau = -2\pi bh\int_{\tau_i}^{\tau_f}\frac{\mathrm{d}\tau}{\mathrm{e}\pi\,Re\,h\tau} = -b\frac{2}{\mathrm{e}\,Re}\ln\left(\frac{\tau_f}{\tau_i}\right). \tag{4.19}$$

Here, $\psi_{w0}=\hat{\psi}_w\left(-h\tau,\sqrt{8h\tau/Re}\right)$ is the fixed-frame stream function evaluated at the point where the $\hat{u}_x=0$ surface intersects the initially marked plane ($x=0$). We may interpret D_- as the backward (thrust) contribution from the wake to the drift volume. Because the wake is mass-deficit-free, the compensating forward (drag) contribution to drift volume D_+ is equal and opposite to D_-, i.e., $D_+=-D_-$. Note that because the description of the flow (4.17) only applies to the wake, τ_f and τ_i should be chosen to be positive values (with $\tau_f>\tau_i$).

It is perhaps tempting to conclude from (4.19) that the fluid transport through the wake is large. The amount of fluid exchanged in the wake diverges as $\tau_f\to\infty$, or equivalently, as $t\to\infty$, and this eventually leads to an infinite volume of transported fluid. However, the logarithmic nature of this divergence makes it quite slow. Moreover, it is multiplied by a factor of $1/Re$, suggesting

that the amount of fluid exchanged in the wake diminishes quickly as Re is increased. Therefore, the bidirectional wake flow is likely not a mechanism whereby intermediate Re swimmers may induce significant large-scale fluid transport or mixing.

4.6 Summary

We have estimated the drift volume induced by a self-propelled swimmer by using a translating symmetric force-dipole description of the induced (far-field) flow. We have shown that the drift volume due to a Stokesian swimmer ($Re = 0$), while less than that of a towed body, is still potentially large compared to the volume of the swimmer's body if the swimmer traverses an asymmetric path. The ability of Stokesian swimmers to transport large fluid volumes via the drift volume mechanism explains their ability to effectively mix their surroundings [20]. We have also shown that the drift volume quickly decreases as Re is increased, suggesting that intermediate-Re swimmers are much less effective at mixing at scales large than their own body size.

Throughout the chapter, we have assumed that strength of the force dipole b is $O(1)$ and dominates the far-field flow. However, some swimmers lack a strong force-dipole and are instead 'quadrupolar' swimmers; Volvox are an example of this [111]. A neutrally buoyant quadrupolar swimmer is expected to produce a small, $O(1)$, drift volume because the far-field flow disturbance it produces decays more rapidly, as $1/\hat{r}^3$, than for a dipolar swimmer. Furthermore, swimmers that are not neutrally buoyant may have a significant Stokeslet flow component, which can contribute significantly to the drift volume. Finally, we have only considered the case of a steady swimmer. Interestingly, unsteady finite-Re swimmers, unlike their Stokesian counterparts, may impart a non-zero net amount of momentum onto the fluid over a stroke

cycle. This is due to the non-linear nature of finite-Re flows; the momentum imparted on the fluid during the propulsive phase of the stroke cycle does not necessarily equal the amount reabsorbed during the recovery phase [19, 31]. This topic deserves further investigation, since a total net momentum deficit caused by the swimmer may lead to much larger drift volumes than would be predicted for an equivalent steady swimmer. Furthermore, we have not accounted for the collective effects of dense aggregations of swimmers, which may induce a large collective drift volume when migrating as a group. This topic is another interesting direction of future study, as abundant marine species such as Antarctic krill are known for their swarming behavior [114].

Chapter 5

Summary and Conclusions

5.1 Summary of research accomplishments

We have paired simple mathematical models of swimmers with analytical and numerical tools in order to make important general predictions about the fluid mechanics of self-propelled bodies. In particular, we have considered the effect of fluid inertia on a 'squirmer' and we were able to quantify the flows produced by this model swimmer as a function of the Reynolds number, Re. This work is motivated by a critical and long-standing knowledge gap in the physics of finite Re self-propulsion. Moreover, we have quantified the amount of fluid fluid transported by towed bodies and self-propelled swimmers as a function of Re. We have utilized the concept of the drift volume in order to do so, which has the advantage of being easily computed for model swimmers that capture the relevant physics. We focus on swimmers that move at small to moderate Re, since such organisms have been implicated in large-scale mixing of the oceans [21, 115, 17]. It is hoped that our work may aid in the intense and ongoing debate concerning the extent to which swimmers transport fluid mass [18, 19, 105, 16].

In chapter 2, we considered the spherical 'squirmer' model of self-propulsion.

The 'swimming stroke' of this model swimmer is described by a steady, fixed velocity profile. A combination of spectral-element and finite-volume methods is used to numerically compute the steady, axisymmetric and unsteady, three-dimensional flows, respectively, around a force-free squirmer for $0.01 \leq Re \leq 1000$. Despite its great simplicity (or perhaps owing to it), the squirmer model reveals a great deal about finite Re swimming, with fundamental differences arising between 'pusher' and 'puller' type squirmers. Pushers, which generate thrust from the rear, efficiently shed vorticity away from their body and into to their wake, leading to the preservation of steady, laminar flow at large Re. This is a remarkable observation, considering the bluff, spherical shape of the squirmer and the large $O(1/\sqrt{Re})$ amount of vorticity generated within the boundary layer at the squirmer's surface. Similar characteristics are shared by the near-field flow around a shear-free, spherical bubble, where the mobile surface achieves a similar effect, although the boundary layer vorticity is only $O(1)$ in this case.

In contrast, the steady, axisymmetric flow around pullers destabilizes at a critical value of Re, yielding to unsteady, three-dimensional flow. This critical Re drops rapidly as the magnitude of the parameter β, which roughly describes the 'strength' of the pusher ($\beta < 0$) or puller ($\beta > 0$), increases beyond unity. The behavior of the near-field flow around a puller is quite analogous to a towed sphere; in both cases the recirculatory eddies attached to the rear of the body are shed into the wake in an unsteady manner that is regular at first but becomes increasingly chaotic as Re is increased [67].

Finally, we show that the swimming efficiency of pushers and pullers is nearly equal up until the point where the axisymmetric flow around the puller destabilizes. This is also remarkable considering that pushers swim considerably faster than pullers for a given value of $|\beta|$ for moderate to large Re. Essentially, pullers expend less energy per unit swimming speed. However,

pullers suffer from reduced efficiency compared to a pusher due to the vortex shedding that occurs above the critical Re.

In chapters 3 and 4, our focus shifts from studying the detailed near-field flows produced by a model swimmer to analyzing the net fluid transport induced by towed and self-propelled bodies in an unbounded fluid domain. Specifically, we consider the drift volume, which quantifies the net volume of fluid entrained by the body as it translates. The drift volume D is defined as the fluid volume swept out by a marked material surface that is initially flat and perpendicular to the direction of the body's translation. Specifically, we compute the drift volume D induced by towed and swimming bodies as a function of Re to investigate the effect of inertia on fluid transport.

In chapter 3, we construct a geometric definition of the drift volume that can be applied to finite travel times t and a marked plane of a finite radius h. This generalizes Darwin's original definition, which requires h and t to both be infinite, and the partial drift volume concept introduced by Eames, Belcher, and Hunt [23], which applies to finite h but infinite t. This generalized definition is necessary because D potentially diverges as $h \to \infty$ and/or $t \to \infty$ if the surrounding fluid has a finite viscosity [104, 27]. An interesting dual-interpretation of of the drift volume is revealed; D is equal to both the time-integrated flux under a streamline and the volume or revolution between that same streamline and its free-stream position. The latter interpretation was discussed by Yih [93], but its mathematical equivalence to the former interpretation has not been previously demonstrated in the literature.

Armed with this generalized definition of D, asymptotic analysis for large h/a, where a is the characteristic size of the translating body, is employed to compute a leading order approximation to D as a function of Re. In our analysis, the critical parameter $Re_h = Re\, h/a$ arises, which quantifies the relative effect of inertial versus viscous forces on the motion of the marked fluid

(and hence D). We demonstrate that fluid inertia generally acts to decrease D, relative to the body volume ($\sim a^3$), due to the weakening of the far-field flow beyond the Oseen distance, a/Re. However, there exists a viscous wake behind the towed body, through which there is a constant fluid flux $Q = F/\varrho U$, where F is the force on the body, U is the speed of the body, and ϱ is the fluid density [78]. This ultimately results in a logarithmic divergence of the drift volume with time as $D/a^3 \sim Q(h/a)^2 \ln(tU/ah\, Re_h)$. This can be contrasted with the case of an inviscid fluid, where the complete lack of viscous forces lead to D/a^3 being no larger than $O(1)$. Clearly, the presence of viscous forces is key to the generation of a large drift volume.

In chapter 4, we perform a similar analysis to compute the drift volume induced by a steadily translating self-propelled swimmer that is assumed to be free of external forces (e.g, it is neutrally buoyant). The swimmer is modeled as a simple force dipole, which captures the universal large-scale flow characteristics that are common to most force-free swimmers [111, 29]. Although the drift volume of a Stokesian $Re = 0$ swimmer traversing a symmetric path with respect to the marked fluid is only $D/a^3 = O(1)$ [19, 28], a much more significant, $O(h/a)$ 'partial' drift volume is found if the path is asymmetric. Such non-symmetric paths occur when the swimmer starts and then stops or changes direction after some amount of time. This indicates that Stokesian swimmers are indeed capable of transporting large volumes of fluid. This is reflected by experimental [106, 107, 108] and theoretical [20, 109] observations of markedly enhanced fluid tracer diffusion due to a suspension of dipolar Stokesian swimmers over 'potential flow' swimmers.

We also estimate the drift volume due to a finite Re swimmer by using the expected form of the far-field velocity, which is given by the Oseen doublet [29]. We discover that D dies off as $1/Re$, placing a severe limitation on the potential fluid transport by steady, force-free swimmers at $Re \geq O(1)$. One

may surmise from our results that such a swimmer has at most $D/a^3 \sim O(1)$, which is of the same order of magnitude as a swimmer in an inviscid fluid. This is of potential consequence to the amount of fluid transport induced by the diel-vertical migrations of moderate Re swimmers in the oceans, which have been suggested to be of possible importance in ocean mixing [17, 115, 21]. Our results suggest that such swimmers may be quite limited in their ability to mix their surrounding fluid via the mechanism of Darwinian drift. However, it is important to note that this is based on estimates for steady individual swimmers, and it is possible for collective or unsteady effects at finite Re to induce a net drift that is possibly larger than predicted for a steady swimmer [19]. This is a topic for future investigation that is discussed further in section 5.2.

5.2 Future work

In our discussion of fluid transport by swimmers via the drift volume mechanism in chapter 4, we assumed that locomotion was steady, with the thrust exactly balancing the drag at all times. However, real swimmers often utilize unsteady mechanisms of propulsion. For example, a jellyfish swims by rapidly contracting its bell-shaped body from an initially extended position during the propulsive stage of its swimming stroke, where the jellyfish accelerates rapidly. This is followed by a recovery phase where the jellyfish coasts some distance while slowly decelerating. This mechanism of swimming is often referred to as 'jet propulsion' [116, 31]. Copepods utilize a similar mechanism during escape swimming, in which long swimming legs are rapidly contracted from an extended position to a position folded along the copepod's body during propulsion [117, 110].

At small Re, the flow is unaffected by unsteadiness in a time-averaged

sense over many stroke cycles. An unsteady Stokesian swimmer undergoes accelerations due to alternating periods of the thrust exceeding the drag and vice versa over a single stroke period. Due to these unbalanced forces, there exists an unsteady Stokeslet component to the flow. However, owing to the linearity of the Stokes equations, there will be no time-averaged Stokeslet flow as long as the swimmer does not have an average acceleration over many stroke cycles. This explains why steady models are adequate to describe the time-average flow of unsteady swimmers [111, 112].

The situation at finite Re is fundamentally different due to the nonlinear nature of the flow. Mathematically, this is a consequence of the nonlinear (convective) inertia term in the Navier-Stokes equations. Here, the momentum imparted on the fluid during the fast propulsive phase of a swimming stroke does not necessarily equal the momentum that is reabsorbed by the swimmer during the recovery phase. This implies that an *unsteady* inertial swimmer may impart some net amount of momentum on the fluid, which may have important consequences for the induced drift volume [19].

Far from the swimmer, the net momentum imparted on the fluid (per unit time) will appear as an effective point force exerted on the fluid at the swimmer's location. This force will be unsteady in general but may be averaged over a swimming cycle to give the average net momentum deficit in the wake. Remarkably, this suggests that an *unsteady* swimmer may be treated as a *steadily towed* body moving under a effective force F_{eff} for the purposes of estimating the drift volume. The theory presented in chapter 3 for towed bodies at finite Re may therefore be applied to estimate the drift volume of an unsteady swimmer based on F_{eff}. Unfortunately, we are not aware of any estimates, experimental or theoretical, of the rate at which an unsteady swimmer imparts momentum on its surrounding fluid. Thus, the proposed work would involve obtaining such estimates of F_{eff} as a function of Re.

This could conceivably be accomplished by performing numerical simulations of an unsteady swimmer and then analyzing the strength of the average net momentum deficit that is generated in the swimmer's wake. From this, it could be determined whether or not an unsteady swimmer is capable of transporting significantly more fluid than steady swimmer at finite Re, which ultimately depends on whether F_{eff} may be sufficiently large for a realistic swimmer. It would be interesting to examine different unsteady swimming mechanisms in this context. For example, organisms that use a jet propulsion mechanism, e.g., jellyfish or scallops, often propel themselves forward several body lengths over a single powerful stroke cycle, and the inherent unsteadiness of this mechanism could be expected to produce more drift in comparison to that due to steadier swimmers.

Appendix A

Validation of numerical solutions

Convergence of the flow computations with respect to the grid parameters was tested empirically. First, it was ensured that the distance R_∞ from the squirmer at which uniform flow was imposed was large enough as to not affect the computed swimming speed U. Computations were relatively insensitive to this parameter due to the fast velocity decay from the squirmer surface ($\sim 1/r^2$) at $Re = 0$ and $\sim 1/r^3$ at large Re, outside the wake) [18], provided that the domain was not so small as to restrict flow near the squirmer body. For

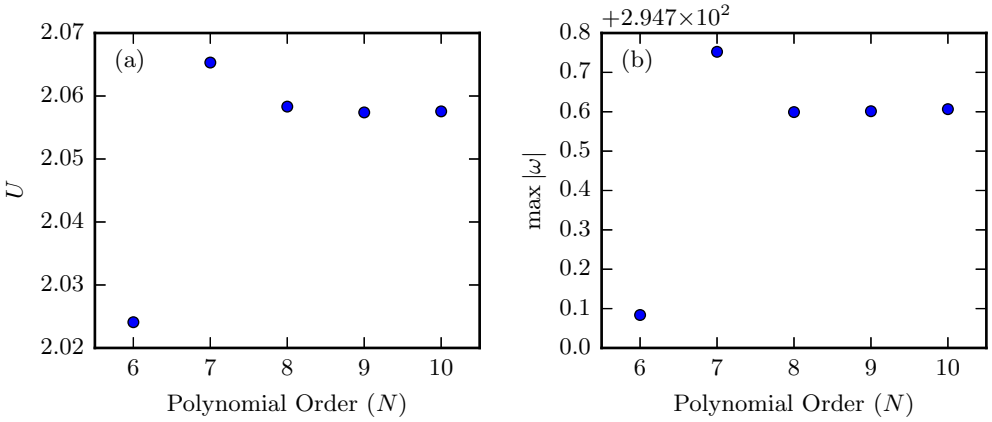

Figure A.1: Convergence of the swimming speed U (a) and $\max|\omega|$ (b) for a $\beta = 5$ puller at $Re = 1000$ computed via a spectral element method for steady, axisymmetric flow. The horizontal axis represents the degree of the shape functions within each element. The element thickness in the boundary layer was $\Delta_{r0} = 0.01$.

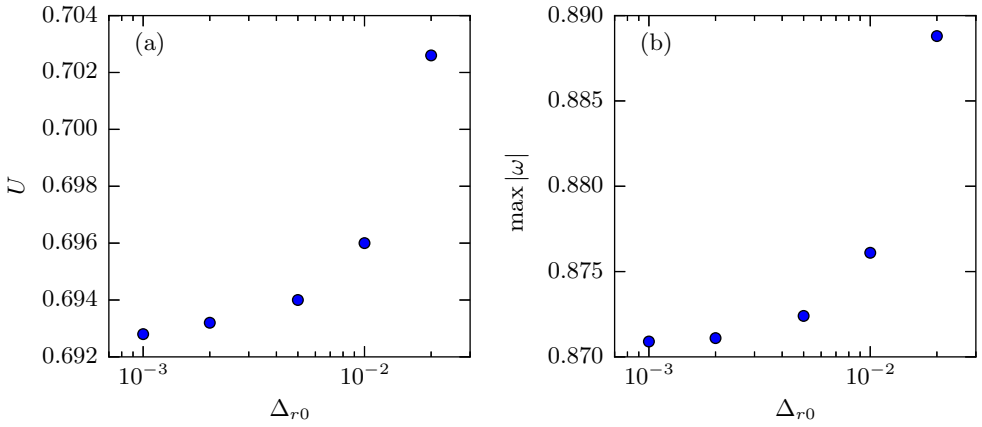

Figure A.2: Convergence of the swimming speed U (a) and $\max|\omega|$ (b) with respect to the grid resolution at the squirmer surface for 3D, unsteady flow computed via a second-order accurate finite-volume method. Here, $\beta = -0.5$ and $Re = 1$.

the axisymmetric computations, the polynomial order N of the shape functions within each element was incrementally increased to convergence (figure A.1). In order to fully resolve the boundary layer, it was ensured that the condition $\Delta_{r0}/\delta \lesssim N^2/9$ [118] was satisfied, where Δ_{r0} is the element size (perpendicular to the boundary layer) and δ is the boundary layer thickness. The thickness of the boundary layer was estimated as $\delta = O(1/\sqrt{Re})$ since the boundary layer is expected to be laminar. For the second-order accurate finite-volume method used for 3D computations, a higher mesh resolution is required due to the lower order approximation, and a satisfactorily converged solutions were reached with $\Delta_{r0} = 0.001$ (figure A.2).

Additional validation of our computational methods was carried out by computing the drag coefficient of a no-slip sphere in uniform flow and comparing to previously known results (figure A.3). The drag coefficient is defined as $C_D = 2F_D/(\pi\varrho a^2 U^2)$, where F_D is the drag force and U is the far-field velocity of the oncoming flow. Known values are provided by the correlation $C_D = (\sqrt{12/\,Re_U} + 0.5407)^2$ [119]. Additionally, values in (potentially unstable) steady, axisymmetric flow up to $Re_U = 2500$ are provided by Fornberg

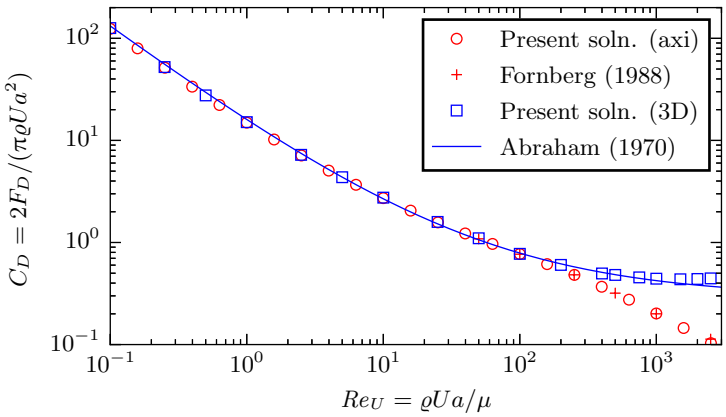

Figure A.3: The drag coefficient C_D of a no-slip sphere in uniform flow computed using the numerical methods described in section 2.3. Comparison is made to the results of Fornberg [71] (for steady, axisymmetric flow) and the correlation given by Abraham [119].

[71]. The computational meshes used for our computations were the same as those used for the squirmer computations at $Re = 1000$. The results of the comparison show good agreement. Note that when $Re_U \gtrsim 500$, C_D becomes nearly constant, and the reported computations reproduce this feature.

References

[1] J. Gray. *Animal locomotion*. Weidenfeld & Nicolson, 1968.

[2] E. M. Purcell. "Life at low Reynolds number". In: *Am. J. Phys.* 45 (1977), pp. 3–11.

[3] C. Brennen and H. Winnet. "Fluid mechanics of propulsion by cilia and flagella". In: *Ann. Rev. Fluid Mech.* 9 (1977), pp. 339–398.

[4] E. Lauga and T. R. Powers. "The hydrodynamics of swimming microorganisms". In: *Rep. Prog. Phys.* 72 (2009), p. 096601.

[5] O. S. Pak and E. Lauga. "Theoretical Models of Low-Reynolds-Number Locomotion". In: *Fluid-Structure Interactions in Low-Reynolds-Number Flows*. The Royal Society of Chemistry, 2016. Chap. 4, pp. 100–167. ISBN: 978-1-84973-813-2. DOI: 10.1039/9781782628491-00100.

[6] T. Miloh and A. Galper. "Self-Propulsion of General Deformable Shapes in a Perfect Fluid". In: *Proc. Roy. Soc. A* 442.1915 (Aug. 1993), pp. 273–299. ISSN: 1364-5021. DOI: 10.1098/rspa.1993.0104.

[7] S. Childress. *Mechanics of Swimming and Flying*. Cambridge Univ. Press, 1981.

[8] M. J. Lighthill. "Note on the swimming of slender fish". In: *J. Fluid Mech.* 9.02 (Mar. 1960), p. 305. ISSN: 0022-1120. DOI: 10.1017/S0022112060001110.

[9] P. G. Saffman. "The self-propulsion of a deformable body in a perfect fluid". In: *J. Fluid Mech.* 28.02 (1967), pp. 385–389.

[10] M. J. McHenry, E. Azizi, and J. A. Strother. "The hydrodynamics of locomotion at intermediate Reynolds numbers: undulatory swimming in ascidian larvae (*Botrylloides sp.*)" In: *J. Exp. Biol.* 206.2 (2003), pp. 327–343.

[11] S. B. Schnack-Schiel, Elke M., and Astrid C. "Copepod abundance and species composition in the Eastern subtropical/tropical Atlantic". In: *Deep Sea Research Part II: Topical Studies in Oceanography* 57.24-26 (2010). Species Diversity of Marine Zooplankton, pp. 2064–2075. ISSN: 0967-0645. DOI: http://doi.org/10.1016/j.dsr2.2010.09.010.

[12] A. Atkinson et al. "A re-appraisal of the total biomass and annual production of Antarctic krill". In: *Deep Sea Research Part I: Oceanographic Research Papers* 56.5 (2009), pp. 727–740. ISSN: 0967-0637. DOI: http://doi.org/10.1016/j.dsr.2008.12.007.

[13] C. E. Jordan. "A model of rapid-start swimming at intermediate Reynolds number: undulatory locomotion in the chaetognath *Sagitta elegans*". In: *J. Exp. Biol.* 163.1 (1992), pp. 119–137.

[14] S. Kern and P. Koumoutsakos. "Simulations of optimized anguilliform swimming". In: *J. Exp. Biol.* 209 (2006), pp. 4841–4857.

[15] M. Gazzola, W. M. Van Rees, and P. Koumoutsakos. "C-start: optimal start of larval fish". In: *J. Fluid Mech.* 698 (May 2012), pp. 5–18. ISSN: 1469-7645. DOI: 10.1017/jfm.2011.558.

[16] W. K. Dewar et al. "Does the marine biosphere mix the ocean?" In: *J. Mar. Res.* 64.4 (July 2006), pp. 541–561. ISSN: 00222402. DOI: 10.1357/002224006778715720.

[17] K. Katija and J. O. Dabiri. "A viscosity-enhanced mechanism for biogenic ocean mixing". In: *Nature* 460.7255 (July 2009), pp. 624–6. ISSN: 1476-4687. DOI: 10.1038/nature08207.

[18] G. Subramanian. "Viscosity-enhanced bio-mixing of the oceans". In: *Curr. Sci* 98.8 (2010), pp. 1103–1108.

[19] A. M. Leshansky and L. M. Pismen. "Do small swimmers mix the ocean?" In: *Phys. Rev. E* 82.2 (Aug. 2010), p. 025301. ISSN: 1539-3755. DOI: 10.1103/PhysRevE.82.025301.

[20] Z. Lin, J.-L. Thiffeault, and S. Childress. "Stirring by squirmers". In: *J. Fluid Mech.* 669 (Feb. 2011), pp. 167–177.

[21] J. C. Nawroth and J. O. Dabiri. "Induced drift by a self-propelled swimmer at intermediate Reynolds numbers". In: *Phys. Fluids* 26.9 (2014). DOI: 10.1063/1.4893537.

[22] C. Darwin. "Note on hydrodynamics". In: *Math. Proc. Cambridge Philos. Soc.* 49.02 (Oct. 1953), pp. 342–354. ISSN: 0305-0041. DOI: 10.1017/S0305004100028449.

[23] I. Eames, S. E. Belcher, and J. C. R. Hunt. "Drift, partial drift and Darwin's proposition". In: *J. Fluid Mech.* 275 (Apr. 1994), p. 201. ISSN: 0022-1120. DOI: 10.1017/S0022112094002338.

[24] I. Eames, J. C. R. Hunt, and S. E. Belcher. "Displacement of inviscid fluid by a sphere moving away from a wall". In: *J. Fluid Mech.* 324 (Apr. 1996), pp. 333–353. DOI: 10.1017/S002211209600794X.

[25] I. Eames and G. Duursma. "Displacement of horizontal layers by bubbles injected into fluidised beds". In: *Chem. Eng. Sci.* 52.16 (Aug. 1997), pp. 2697–2705. DOI: 10.1016/S0009-2509(96)00474-5.

[26] J. O. Dabiri. "Note on the induced Lagrangian drift and added-mass of a vortex". In: *J. Fluid Mech.* 547 (Jan. 2006), p. 105. ISSN: 0022-1120. DOI: 10.1017/S0022112005007585.

[27] I. Eames, D. Gobby, and S. B. Dalziel. "Fluid displacement by Stokes flow past a spherical droplet". In: *J. Fluid Mech.* 485 (2003), pp. 67–85. ISSN: 00221120. DOI: 10.1017/S0022112003004361.

[28] D. O. Pushkin, H. Shum, and J. M. Yeomans. "Fluid transport by individual microswimmers". In: *J. Fluid Mech.* 726 (May 2013), pp. 5–25. ISSN: 0022-1120. DOI: 10.1017/jfm.2013.208.

[29] Y. D. Afanasyev. "Wakes behind towed and self-propelled bodies: Asymptotic theory". In: *Phys. Fluids* 16.8 (2004), pp. 3235–3238. DOI: 10.1063/1.1768071.

[30] N. G. Chisholm et al. "A squirmer across Reynolds numbers". In: *J. Fluid Mech.* 796 (June 2016), pp. 233–256. ISSN: 0022-1120. DOI: 10.1017/jfm.2016.239.

[31] S. Vogel. *Life in Moving Fluids: The Physical Biology of Flow*. Princeton, NJ: Princeton University Press, 1994. ISBN: 0-691-03485-0.

[32] M. J. Lighthill. *Mathematical Biofluiddynamics*. Philadelphia: SIAM, 1975.

[33] M. J. Lighthill. "On the squirming motion of nearly spherical deformable bodies through liquids at very small Reynolds numbers". In: *Commun. Pure Appl. Math.* 5 (1952), pp. 109–118.

[34] J. R. Blake. "A spherical envelope approach to ciliary propulsion". In: *J. Fluid Mech.* 46 (1971), pp. 199–208.

[35] G. K. Batchelor. "The stress system in a suspension of force-free particles". In: *J. Fluid Mech.* 41 (03 Apr. 1970), pp. 545–570. ISSN: 1469-7645. DOI: 10.1017/S0022112070000745.

[36] T. Ishikawa, M. P. Simmonds, and T. J. Pedley. "Hydrodynamic interaction of two swimming model micro-organisms". In: *J. Fluid Mech.* 568 (2006), pp. 119–160.

[37] T. Ishikawa, M. P. Simmonds, and T. J. Pedley. "The rheology of a semi-dilute suspension of swimming model micro-organisms". In: *J. Fluid Mech.* 588 (2007), pp. 399–435.

[38] V. Magar, T. Goto, and T. J. Pedley. "Nutrient uptake by a self-propelled steady squirmer". In: *Q. J. Mechanics Appl. Math.* 56 (2003), pp. 65–91.

[39] L. Zhu et al. "Locomotion by tangential deformation in a polymeric fluid". In: *Phys. Rev. E* 83.1 (Jan. 2011), p. 011901.

[40] L. Zhu, E. Lauga, and L. Brandt. "Self-propulsion in viscoelastic fluids: Pushers vs. pullers". In: *Phys. Fluids* 24.5 (2012), p. 051902.

[41] J.-L. Thiffeault and S. Childress. "Stirring by swimming bodies". In: *Phys. Lett. A* 374.34 (July 2010), pp. 3487–3490.

[42] V. Magar and T. J. Pedley. "Average nutrient uptake by a self-propelled unsteady squirmer". In: *J. Fluid Mech.* 539 (2005), pp. 93–112.

[43] S. Michelin and E. Lauga. "Optimal feeding is optimal swimming for all Péclet numbers". In: *Phys. Fluids* 23.10 (2011), p. 101901.

[44] K. Drescher et al. "Dancing Volvox: Hydrodynamic bound states of swimming algae". In: *Phys. Rev. Lett.* 102.168101 (2009), pp. 1–4.

[45] I. Llopis and I. Pagonabarraga. "Hydrodynamic interactions in squirmer motion: Swimming with a neighbour and close to a wall". In: *Journal of Non-Newtonian Fluid Mechanics* 165.17-18 (2010), pp. 946–952.

[46] S. Wang and A. Ardekani. "Inertial squirmer". In: *Phys. Fluids* 24 (2012), p. 101902.

[47] A. S. Khair and N. G. Chisholm. "Expansions at small Reynolds numbers for the locomotion of a spherical squirmer". In: *Phys. Fluids* 26.1 (Jan. 2014), p. 011902. ISSN: 1089-7666. DOI: 10.1063/1.4859375.

[48] G.-J. Li and A. M. Ardekani. "Hydrodynamic interaction of microswimmers near a wall". In: *Phys. Rev. E* 90 (1 July 2014), p. 013010. DOI: 10.1103/PhysRevE.90.013010.

[49] E. D. Tytell et al. "Interactions between internal forces, body stiffness, and fluid environment in a neuromechanical model of lamprey swimming". In: *Proc. Natl. Acad. Sci. U.S.A.* 107.46 (2010), pp. 19832–19837.

[50] A. Hamel et al. "Transitions between three swimming gaits in Paramecium escape". In: *Proc. Natl. Acad. Sci. USA* 108.18 (2011), pp. 7290–7295.

[51] G. I. Matsumoto. "Swimming movements of ctenophores, and the mechanics of propulsion by ctene rows". English. In: *Hydrobiologia* 216-217.1 (1991), pp. 319–325. ISSN: 0018-8158. DOI: 10.1007/BF00026481.

[52] S. L. Tamm. "Cilia and the life of ctenophores". In: *Invertebrate Biol.* 133.1 (2014), pp. 1–46.

[53] M. Horowitz and C. H. K. Williamson. "The effect of Reynolds number on the dynamics and wakes of freely rising and falling spheres". In: *J. Fluid Mech.* 651 (2010), pp. 251–294.

[54] P. Ern et al. "Wake-induced oscillatory paths of bodies freely rising or falling in fluids". In: *Ann. Rev. Fluid Mech.* 44 (2012), pp. 97–121.

[55] G. E. Karniadakis and S. Sherwin. *Spectral/hp Element Methods for Computational Fluid Dynamics*. 2nd ed. Oxford Univ. Press, 2005.

[56] C. Geuzaine and J.-F. Remacle. "Gmsh: A 3-D finite element mesh generator with built-in pre-and post-processing facilities". In: *Intl J. Numer. Methods Eng.* 79.11 (2009), pp. 1309–1331.

[57] D. Legendre and J. Magnaudet. "The lift force on a spherical body in a viscous linear shear flow". In: *J. Fluid Mech.* 368 (1998), pp. 81–126.

[58] J. Magnaudet, M. Rivero, and J. Fabre. "Accelerated flows past a rigid sphere or a spherical bubble. Part 1. Steady strainning flow". In: *J. Fluid Mech.* 284 (1995), pp. 97–135.

[59] A. Merle, D. Legendre, and J. Magnaudet. "Forces on a high-Re spherical bubble in a turbulent flow". In: *J. Fluid Mech.* 532 (2005), pp. 53–62.

[60] D. Legendre, A. Merle, and J. Magnaudet. "Wake of a spherical bubble or a solid sphere set fixed in a turbulent environment". In: *Phys. Fluids* 18.4 (2006), p. 048102.

[61] Y. Hallez and D. Legendre. "Interaction between two spherical bubbles rising in a viscous liquid". In: *J. Fluid Mech.* 673 (2011), pp. 406–431.

[62] G. Mougin and J. Magnaudet. "Path instability of a rising bubble". In: *Phys. Rev. Lett.* 88.1 (2001), p. 014502.

[63] J. Magnaudet and G. Mougin. "Wake instability of a fixed spheroidal bubble". In: *Journal of Fluid Mechanics* 572 (Feb. 2007), pp. 311–337. ISSN: 1469-7645. DOI: 10.1017/S0022112006003442.

[64] D. Fabre, F. Auguste, and J. Magnaudet. "Bifurcations and symmetry breaking in the wake of axisymmetric bodies". In: *Phys. Fluids* 20.5 (2008), p. 051702.

[65] R. Natarajan and A. Acrivos. "The instability of the steady flow past spheres and disks". In: *J. Fluid Mech.* 254 (1993), pp. 323–344.

[66] T. A. Johnson and V. C. Patel. "Flow past a sphere up to a Reynolds number of 300". In: *J. Fluid Mech.* 378 (Jan. 1999), pp. 19–70. ISSN: 00221120. DOI: 10.1017/S0022112098003206.

[67] A. G. Tomboulides and S. A. Orszag. "Numerical investigation of transitional and weak turbulent flow past a sphere". In: *J. Fluid Mech.* 416 (2000), pp. 45–73.

[68] D. W. Moore. "The boundary layer on a spherical gas bubble". In: *J. Fluid Mech.* 16.02 (1963), pp. 161–176. DOI: 10.1017/S0022112063000665.

[69] L. G. Leal. "Vorticity transport and wake structure for bluff bodies at finite Reynolds number". In: *Phys. Fluids A: Fluid Dyn.* 1.1 (1989), pp. 124–131. ISSN: 08998213. DOI: 10.1063/1.857540.

[70] S. C. R. Dennis and J. D. A. Walker. "Calculation of the steady flow past a sphere at low and moderate Reynolds numbers". In: *J. Fluid Mech.* 48.04 (Mar. 1971), pp. 771–789. ISSN: 0022-1120. DOI: 10.1017/S0022112071001848.

[71] B. Fornberg. "Steady viscous flow past a sphere at high Reynolds numbers". In: *J. Fluid Mech.* 190 (1988), pp. 471–489.

[72] G. K. Batchelor. "A proposal concerning laminar wakes behind bluff bodies at large Reynolds number". In: *J. Fluid Mech.* 1.04 (1956), pp. 388–398.

[73] D. S. Dandy and L. G. Leal. "Boundary-layer separation from a smooth slip surface". In: *Phys. Fluids* 29.5 (1986), pp. 1360–1366.

[74] A. Blanco and J. Magnaudet. "The structure of the axisymmetric high-Reynolds number flow around an ellipsoidal bubble of fixed shape". In: *Phys. Fluids* 7.6 (1995), pp. 1265–1274.

[75] W. M. Deen. *Analysis of Transport Phenomena*. Oxford Univ. Press, 1998.

[76] H. A. Stone. "An interpretation of the translation of drops and bubbles at high Reynolds numbers in terms of the vorticity field". In: *Phys. Fluids A Fluid Dyn.* 5.10 (1993), pp. 2567–2569. ISSN: 08998213. DOI: 10.1063/1.858771.

[77] H. A. Stone and A. D. T. Samuel. "Propulsion of microorganisms by surface distorsions". In: *Phys. Rev. Lett.* 77 (1996), pp. 4102–4104.

[78] G. K. Batchelor. *An Introduction to Fluid Mechanics*. Cambridge Univ. Press, 1967.

[79] G. Ryskin. "The extensional viscosity of a dilute suspension of spherical particles at intermediate microscale Reynolds numbers". In: *J. Fluid Mech.* 99.03 (1980), pp. 513–529.

[80] Jeffrey A Walker. "Functional Morphology and Virtual Models: Physical Constraints on the Design of Oscillating Wings, Fins, Legs, and Feet at Intermediate Reynolds Numbers". In: *Integrative and Comparative Biology* 42.2 (Apr. 2002), pp. 232–242. DOI: 10.1093/icb/42.2.232.

[81] P. J. Berenson. "Experiments on pool-boiling heat transfer". In: *International Journal of Heat and Mass Transfer* 5.10 (1962), pp. 985–999. ISSN: 0017-9310. DOI: 10.1016/0017-9310(62)90079-0.

[82] I. Eames and M. A. Gilbertson. "Mixing and drift in gas-fluidised beds". In: *Powder Technol.* 154.2 (2005), pp. 185–193. ISSN: 00325910. DOI: 10.1016/j.powtec.2005.04.036.

[83] S. K. Kawatra and T. C. Eisele. *Flotation column with adjustable supported baffles*. US Patent 5,335,785. 1994.

[84] W. J. M. Rankine. "On Plane Water-Lines in Two Dimensions". In: *Phil. Trans. R. Soc. London* 154 (1864), pp. 369–391. ISSN: 02610523.

[85] J. C. Maxwell. In: *Proc. London Math. Soc.* 1-3 (1 1869), p. 82.

[86] W. H. Munk. "Abyssal recipes". In: *Deep Sea Research and Oceanographic Abstracts* 13.4 (1966), pp. 707–730. ISSN: 0011-7471. DOI: 10.1016/0011-7471(66)90602-4.

[87] I. Eames and J.-B. Flór. "Fluid transport by dipolar vortices". In: *Dyn. Atmos. Ocean.* 28.2 (1998), pp. 93–105. ISSN: 03770265. DOI: 10.1016/S0377-0265(98)00046-3.

[88] S. Melkoumian and B. Protas. "Wake effects on drift in two-dimensional inviscid incompressible flows". In: *Phys. Fluids* 26.12 (2014). DOI: 10.1063/1.4903066.

[89] I. R. Peters et al. "Volume entrained in the wake of a disk intruding into an oil-water interface". In: *Phys. Rev. Fluids* 1 (3 July 2016), p. 033901. DOI: 10.1103/PhysRevFluids.1.033901.

[90] I. Eames. "The concept of drift and its application to multiphase and multibody problems". In: *Phil. Trans. A. Math. Phys. Eng. Sci.* 361.1813 (2003), pp. 2951–65. ISSN: 1364-503X. DOI: 10.1098/rsta.2003.1277.

[91] S. Melkoumian and B. Protas. "Drift due to two obstacles in different arrangements". In: *Theor. Comput. Fluid Dyn.* 297 (May 2016), pp. 29–36. ISSN: 0935-4964. DOI: 10.1007/s00162-016-0394-9.

[92] A. Prasad, J. Kondev, and H. A. Stone. "Drift in supported membranes". In: *Phys. Fluids* 19.11 (2007), p. 113103. ISSN: 10706631. DOI: 10.1063/1.2805843.

[93] C.-S. Yih. "New derivations of Darwin's theorem". In: *J. Fluid Mech.* 152 (1985), pp. 163–172. ISSN: 1469-7645. DOI: 10.1017/S0022112085000623.

[94] T. B. Benjamin. "Note on added mass and drift". In: *J. Fluid Mech.* 169 (1986), pp. 251–256.

[95] C.-S. Yih. "Evolution of Darwinian drift". In: *J. Fluid Mech.* 347 (Sept. 1997), pp. 1–11. ISSN: 00221120. DOI: 10.1017/S002211209700654X.

[96] J. Bataille, M. Lance, and J. L. Marie. "Some aspects of the modelling of bubbly flows". In: *Phase-interface phenomena in multiphase flow* (1991), pp. 179–193.

[97] J. W. M. Bush and I. Eames. "Fluid displacement by high Reynolds number bubble motion in a thin gap". In: *Int. J. Multiph. Flow* 24.3 (1998), pp. 411–430. ISSN: 03019322. DOI: 10.1016/S0301-9322(97)00068-2.

[98] M. E. Weber and D. Bhaga. "Fluid drift caused by a rising bubble". In: *Chem. Eng. Sci.* 37.1 (1982), pp. 113–116. ISSN: 00092509. DOI: 10.1016/0009-2509(82)80073-0.

[99] R. Camassa et al. "Brachistochrones in potential flow and the connection to Darwin's theorem". In: *Phys. Lett. A* 372.45 (Nov. 2008), pp. 6742–6749. ISSN: 03759601. DOI: 10.1016/j.physleta.2008.06.093.

[100] H. Lamb. *Hydrodynamics*. Cambridge University Press, 1932.

[101] A. B. Basset. *A Treatise on Hydrodynamics*. Vol. 2. Deighton, Bell and Co., 1888.

[102] P. M. Lovalenti and J. F. Brady. "The hydrodynamic force on a rigid particle undergoing arbitrary time-dependent motion at small Reynolds number". In: *J. Fluid Mech.* 256 (Nov. 1993), p. 561. ISSN: 0022-1120. DOI: 10.1017/S0022112093002885.

[103] J. C. R. Hunt and I. Eames. "The disappearance of laminar and turbulent wakes in complex flows". In: *J. Fluid Mech.* 457 (Apr. 2002), pp. 111–132. DOI: 10.1017/S0022112001007236.

[104] N. G. Chisholm and A. S. Khair. "Drift volume in viscous flows". In: *Phys. Rev. Fluids* (in review).

[105] André W. Visser. "OCEAN SCIENCE: Biomixing of the Oceans?" In: *Science* 316.5826 (May 2007), pp. 838–839. ISSN: 0036-8075. DOI: 10.1126/science.1141272.

[106] Kyriacos C. Leptos et al. "Dynamics of Enhanced Tracer Diffusion in Suspensions of Swimming Eukaryotic Microorganisms". In: *Phys. Rev. Lett.* 103.19 (Nov. 2009), p. 198103. ISSN: 0031-9007. DOI: 10.1103/PhysRevLett.103.198103.

[107] G. L. Miño et al. "Induced diffusion of tracers in a bacterial suspension: theory and experiments". In: *J. Fluid Mech.* 729.2013 (Aug. 2013), pp. 423–444. ISSN: 0022-1120. DOI: 10.1017/jfm.2013.304. eprint: 1210.7704.

[108] H. Kurtuldu et al. "Enhancement of biomixing by swimming algal cells in two-dimensional films". In: *Proc. Natl. Acad. Sci.* 108.26 (June 2011), pp. 10391–10395. ISSN: 0027-8424. DOI: 10.1073/pnas.1107046108.

[109] D. O. Pushkin and J. M. Yeomans. "Fluid Mixing by Curved Trajectories of Microswimmers". In: *Phys. Rev. Lett.* 111.18 (Oct. 2013), p. 188101. ISSN: 0031-9007. DOI: 10.1103/PhysRevLett.111.188101. arXiv: arXiv:1307.6025v1.

[110] J. Yen. "Life in transition: balancing inertial and viscous forces by planktonic copepods." In: *Biol. Bull.* 198.2 (Apr. 2000), pp. 213–24. ISSN: 0006-3185.

[111] Knut Drescher et al. "Direct Measurement of the Flow Field around Swimming Microorganisms". In: *Phys. Rev. Lett.* 105.16 (Oct. 2010), p. 168101. ISSN: 0031-9007. DOI: 10.1103/PhysRevLett.105.168101.

[112] Knut Drescher et al. "Fluid dynamics and noise in bacterial cell-cell and cell-surface scattering". In: *Proc. Natl. Acad. Sci.* 108.27 (July 2011), pp. 10940–10945. ISSN: 0027-8424. DOI: 10.1073/pnas.1019079108.

[113] J. Dunstan et al. "A two-sphere model for bacteria swimming near solid surfaces". In: *Phys. Fluids* 24.1 (Jan. 2012), p. 011901. ISSN: 1070-6631. DOI: 10.1063/1.3676245.

[114] J. W. S. Marr. "The natural history of geography of the Antarctic krill (Euphausia superba Dana)". In: *Discovery report* 32 (1962), pp. 33–464.

[115] K. Katija. "Biogenic inputs to ocean mixing". In: *J. Exp. Biol.* 215.6 (Mar. 2012), pp. 1040–1049. ISSN: 0022-0949. DOI: 10.1242/jeb.059279.

[116] Thomas L. Daniel. "Mechanics and energetics of medusan jet propulsion". In: *Can. J. Zool.* 61.6 (June 1983), pp. 1406–1420. ISSN: 0008-4301. DOI: 10.1139/z83-190.

[117] Luca A. van Duren. "Escape from viscosity: the kinematics and hydrodynamics of copepod foraging and escape swimming". In: *J. Exp. Biol.* 206.2 (Jan. 2003), pp. 269–279. ISSN: 00220949. DOI: 10.1242/jeb.00079.

[118] D. Gottlieb and S. A. Orszag. *Numerical Analysis of Spectral Methods: Theory and Applications*. Vol. 26. SIAM, 1977.

[119] F. F. Abraham. "Functional dependence of drag coefficient of a sphere on Reynolds number". In: *Phys. Fluids* 13.8 (1970), pp. 2194–2195. DOI: 10.1063/1.1693218.